Investigation of Laser Plasma Interactions

by

Joshua Ludwig

A thesis submitted in partial fulfillment of the requirements for the degree of

Doctor of Philosophy

Department of Physics

UNIVERSITY OF ALBERTA

© Joshua Ludwig 2021

Abstract

Both short and long pulse laser plasma interactions are investigated by theoretical analysis and modern computational techniques. An extensive set of simulations of short pulse laser plasma based particle accelerators are performed with the aim of improving performance and diagnostics of the accelerators. Simulations are also compared with experimental results for the production of Mid-Infrared light using relativistically intense short pulse optical lasers.

A new type of long pulse laser based plasma probe is proposed for measuring plasma conditions with a single shot high bandwidth pump-probe configuration. Simulations and theory are presented for the study of shock formation in supersonic plasma flows relevant to the conditions of the inertial confinement fusion targets at the National Ignition Facility.

Acknowledgements

I would first like to thank my supervisor Wojciech Rozmus at the University of Alberta. Wojciech challenged and motivated me to work hard and excel, taking time to discuss projects on a daily basis and ensuring I had opportunity to go to conferences, summer schools, and internships. I would also like to thank Wojciech for introducing me to many experts in the field and for sharing some of his wealth of knowledge about plasma physics and LPI.

I would like to thank my supervisors Scott Wilks and Pierre Michel at LLNL, the LLNL Summer Student Program for funding, use of computers, and travel opportunities such as allowing me to tour GA, LBNL, and SLAC. I would like to thank Scott Wilks and Paul-Edouard Masson-Laborde for teaching me how to use PIC codes and for their collaboration on LWFA and BRA projects. I would like to thank Thomas Chapman and Pierre Michel for teaching me about Fourier optics, the paraxial approximation, and kinetic theory of plasmas, Mikhail Belyaev for teaching me about fluid equations and heat transport, and Stefan Huller for collaboration on our BRA project, for providing CLAW, and for collaboration on our shock formation project.

Contents

List of Figures

List of Tables

List of Abbreviations

BRA	**B**ackward **R**aman **A**mplifier
CBET	**C**ross **B**eam **E**nergy **T**ransfer
CPP	**C**ontinuous **P**hase **P**late
EOM	**E**lectro **O**ptic **M**modulator
GPU	**G**raphics **P**rocessing **U**nit
ICF	**I**nertial **C**onfinement **F**usion
IR	**I**nfra**r**ed
LEH	**L**aser **E**ntrance **H**ole
LPI	**L**aser **P**lasma **I**nteraction
LWFA	**L**aser **W**ake**F**ield **A**ccelerationn
NIF	**N**ational **I**gnition **F**acility
PIC	**P**article **I**n **C**ell
RPP	**R**andom **P**hase **P**late
SBS	**S**timulated **B**rillouin **S**cattering
SSD	**S**moothing (by) **S**pectral **D**ispersion
SRS	**S**timulated **R**aman **S**cattering

Physical Constants

Speed of Light	$c = 2.99792458 \times 10^{8}\ ms^{-1}$ (exact)
Permittivity of Free Space	$\epsilon_0 = 8.8541878128(13) \times 10^{-}12\ Fm^{-1}$
Permeability of Free Space	$\mu_0 = 1.25663706212(19) \times 10^{-6}\ Hm^{-1}$
Electron Rest Mass	$m_e = 9.1093837015(28) \times 10^{-31}\ kg$
Proton Rest Mass	$m_p = 1.67262192369(51) \times 10^{-27}\ kg$
Neutron Rest Mass	$m_n = 1.67492749804(95) \times 10^{-27}\ kg$
Elementary Charge	$e = 1.602176634 \times 10^{-19}\ C$ (exact)

List of Symbols

n_e	electron density	cm^{-3}
n_c	critical electron density	cm^{-3}
v_{the}	electron thermal velocity	ms^{-1}
v_{thi}	ion thermal velocity	ms^{-1}
a_0	normalized peak laser amplitude	$eE/m_e c\omega_0$
ω_{pe}	plasma electron angular frequency	$rads^{-1}$
λ_{pe}	plasma electron wavelength	m

Chapter 1

Introduction

1.1 Introduction

This Ph.D. thesis summarizes the studies of plasma physics and laser matter interactions that fall within the following subject areas: (1) high intensity short pulse laser plasma sources of energetic particles and radiation, (2) laser amplification and beam combining, and (3) high energy density plasmas with applications to inertial confinement fusion (ICF).

The ability of a plasma to sustain large gradients of electric fields has been explored for some time in application to laser wake field accelerators (LWFA). This thesis includes work on investigating different aspects of LWFA with the aim of improving accelerator schemes in terms of stability, energy and numbers of accelerated electrons. We have proposed the first application of the use of a Backward Raman Amplifier (BRA) for enhancing LWFA [58] and the use of Stimulated Raman Scattering (SRS) as a diagnostic to LWFA [37]. Much of the studies in this thesis on LWFA have been closely related to experiments, in particular a collaboration with University of Michigan has led to research projects where numerical and theoretical models were compared and validated with experimental data.

Inertial confinement fusion (ICF) is considered a possible future energy source and research on ICF has over the years led to numerous breakthroughs in laser technology and laser plasma sciences however, ICF still faces issues with implosion symmetry and energy coupling. Plasma diagnostics are essential to understanding plasma conditions and this is critical to validating models to ensure predictive capability. This thesis presents detailed simulations relevant to improving and diagnosing plasma conditions relevant to ICF. We have also studied different realizations of the pump probe schemes in which laser plasmas are used as optical systems operating at laser intensities many orders of magnitude beyond the breaking point of traditional optics. In our published work we have shown that a process similar to Crossed Beam Energy Transfer (CBET) can be used as a single shot laser plasma diagnostic [59].

The research in this thesis is based on my broad experiences with several large-scale numerical simulation tools. For studies of intense ultra-fast laser plasmas, it is necessary to perform kinetic simulations that account for fast particles and nonlocal transport. I have become an expert with the PIC codes SCPIC from University of Alberta, and the massively parallel OSIRIS code supported and constantly developed by an international collaboration. I have also become familiar with many PIC algorithms and written modifications to SCPIC and a number of my own PIC codes.

When performing studies of long pulse high energy laser plasma interactions, it is still desirable to perform kinetic simulations however, these simulations would often require an unreasonable amount of computation time. Due to the large time and space scales of these lasers and plasmas, a fluid description of the plasma is often adequate and requires a fraction of the computing resources. Ray tracing codes are often used for these types of studies and allow for large angle beam deflection, but typically neglect the fine structures of lasers such as the speckles introduced by random phases. We have employed the parallel 3D paraxial nonlinear fluid code pF3D from Lawrence Livermore National Laboratory (LLNL). I have also written many modifications to pF3D and my own paraxial propagators and hydrodynamic simulations. My massively parallel and GPU compatible ray tracing code was used to make several figures in this thesis and was used to produce a video that took third place in the interdisciplinary national "Visualize This!" competition in 2019.

1.2 Stimulated Scattering and Plasma Photonics

In laser produced plasmas stimulated scatterings are parametric instabilities that involve electromagnetic waves scattering from plasma electron (Raman) or ion acoustic (Brillouin) waves. Stimulated scattering typically results in light redirection or energy transfer between two electromagnetic waves. The scattering can be in many directions but gain is usually greatest in the backward direction. Stimulated Raman and Brillouin Scattering (SRS and SBS) can be modeled using a three wave coupling approximation. A stimulated electromagnetic pump wave (ω_0,k_0) decays into two daughter waves ($\omega_{1,2}$,$k_{1,2}$). The waves achieve resonance when the following wave matching conditions are met.

$$\omega_0 = \omega_1 + \omega_2, \quad \vec{k}_0 = \vec{k}_1 + \vec{k}_2, \tag{1.1}$$

Here $\omega_{0,1,2}$ is the frequency and $k_{0,1,2}$ is the wavenumber of the waves, Eq. (1.1) is analogous to conservation of energy (ω) and momentum (k). The resonance occurs when two electromagnetic waves ($\omega_{0,1}$) beat to drive an ion acoustic wave (SBS) or an electron plasma wave (SRS), satisfying its dispersion relation in the plasma. The scattered electromagnetic wave (ω_1) is introduced as an additional seed laser pulse or electromagnetic noise in the plasma. Since the daughter waves have lower frequency than the pump ($\omega_1, \omega_2 < \omega_0$) the interaction produces red shifted scattered light. In plasma densities above the critical density ($n_e > n_c$), where plasma electrons respond on timescales faster than the laser frequency ($\omega_{pe} > \omega_0$), light becomes evanescent. Here $\omega_{pe} = \sqrt{n_e q_e^2/(m_e \epsilon_0)}$ is the electron plasma frequency which depends on the electron density n_e, charge q_e, and mass m_e. For SRS, which has electron plasma waves with frequencies close to the plasma frequency ($\omega_2 \approx \omega_{pe}$), this restricts the interaction to occur only in plasma densities less than one quarter of critical ($n_e < n_c/4$) for the pump wave because at quarter critical the electromagnetic daughter wave will have the same frequency as the plasma ($\omega_1 = \omega_{pe}$). The critical density is defined where the laser frequency equals the plasma frequency and can be expressed as $n_c = m_e \epsilon_0 \omega_0^2 / q_e^2$. An example of a Backward Raman Amplifier (BRA) which uses backward SRS to amplify laser pulses is shown in figure 1.1. In SBS the ion acoustic waves (ω_2) have much lower frequency than the electron plasma waves in SRS because of the large ion mass compared to electrons and the weak dependance on the plasma density. SBS couples to the approximately dispersion-less ion acoustic wave $\omega_{ia} \approx k_{ia}c_s$ where c_s is the sound speed. The relatively low frequency ion acoustic waves of SBS mean there is little frequency shift between the electromagnetic pump and seed waves. This allows for SBS to occur in higher plasma densities, wherever the light is not evanescent ($\omega_0 \approx \omega_1 < \omega_{pe}$).

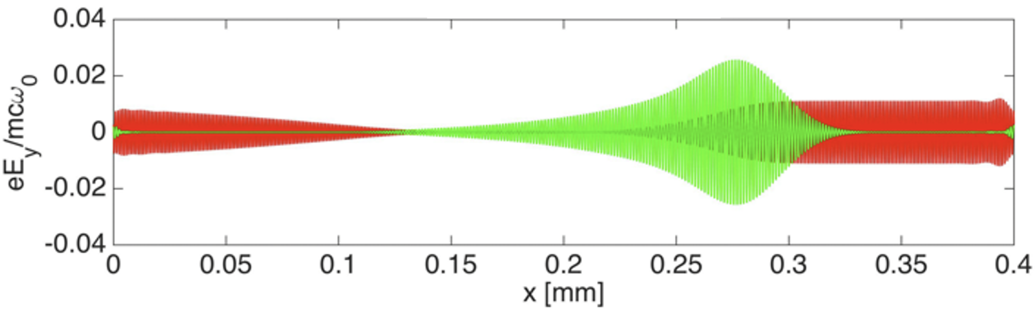

FIGURE 1.1: Electric fields from a 1D PIC simulation of a Backward Raman Amplifier. The short seed laser pulse (green) moves from left to right and is amplified by the long pump laser (red). The seed (ω_1) and pump (ω_0) couple through an electron plasma wave (ω_2) that is not shown.

SRS and SBS have been detrimental in ICF plasmas [31] where laser light is often backscattered. Backscattered light not only reduces energy coupling and implosion symmetry in ICF, but backscattered light also can cause serious damage to the laser optics. The side scattered Brillouin light, or CBET, can result in losses in implosion symmetry. If CBET is well understood it could be harnessed as a means of controlling implosion symmetry [75]. Both SBS and SRS are also investigated for plasma based optical components known as plasma photonics. Plasma photonics components are an attractive method of overcoming material breakdown in strong fields. Plasma photonics components such as amplifiers, polarizers, mirrors, and waveplates have previously been studied [73, 104, 122]. In Chapter 2 of this thesis, the use of SRS is explored as a Backward Raman Amplifier BRA to sustain a laser pulse while it generates a wake to accelerate particles in a plasma. In Chapter 5, the use of SBS is explored in the development of theoretical model for a new plasma diagnostic.

1.3 Laser Wakefield Acceleration

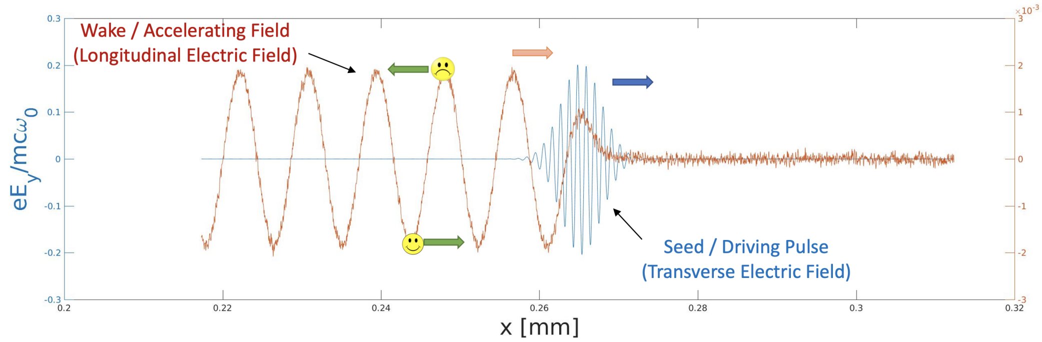

FIGURE 1.2: Electric fields from a 1D PIC simulation of a Laser Wakefield Accelerator. The short laser pulse (blue) moves from left to right and drives an electrostatic plasma wave (red). Electrons can be accelerated by the plasma wave if they are in the right phase.

The basic principle of Laser Wakefield Acceleration (LWFA) [115] is to use a very short (t_{pulse} ~30fs), high intensity ($I \gg 10^{14} W/cm^2$) laser pulse to generate an electrostatic plasma wave that moves with the laser pulse at a phase velocity close to the speed of light. When some fast electrons are injected into the right phase of the wake, they will experience acceleration from the electrostatic field as they move with the wave. However, since the wake actually moves with a phase velocity less than the speed of light, the particles will eventually enter the decelerating phase of the wake.

This is considered the non-relativistic or linear regime of LWFA where the electron oscillation velocity in the laser field is much less than the speed of light ($a_0 \equiv eE/(m_e c \omega_0) < 1$). This regime has the advantage of smooth sinusoidal density perturbations and regular electrostatic fields, but this regime also requires pre-accelerated electrons to be injected into the right phase of the wake in order to be accelerated.

Laser wakefield acceleration currently faces three significant limitations to the amount and energy of the accelerated charge. These limitations are commonly referred to as "pump depletion", "particle dephasing", and "laser diffraction". Pump depletion occurs as the laser gives up energy to create plasma waves and accelerate charge. As the laser loses energy it is no longer able to drive a strong or efficient wake. In a plasma lasers travel slower than the speed of light $v_g \approx c\sqrt{1 - n_e^2/n_c^2} = c\sqrt{1 - \omega_{pe}^2/\omega_0^2}$, where v_g is the group velocity of the laser in the linear regime. The wake originates from the location of the short laser pulse at constant phase so that the phase velocity of the wake is equal to the group velocity of the laser. When particles are accelerated to high energies, they may travel faster than the driving laser and out run the region in which they experience forward acceleration so that dephasing occurs. Since the amplitude of the wake depends on the intensity of the driving pulse, the driving pulse should be focused close to its diffraction limit over as long a distance as possible. To achieve a small focal spot the laser must be focused tightly, and hence it is also subject to rapid defocusing and particles may move transversely to escape the accelerating fields.

To overcome the limitations of pump depletion and laser diffraction in the linear regime of LWFA we propose the use of a backward Raman amplifier in Chapter 2. The principle idea behind Raman amplification is to counter propagate a short seed and a long pump laser pulse. The short pulse is chosen to be downshifted by the plasma frequency and wavenumber from the long pulse. When the pulses overlap, they beat at the plasma frequency creating an electrostatic wave that resonantly couples to amplify the Seed. To apply this to LWFA we use our wake driving pulse as the seed and add a BRA pump, by using this method we can directly apply corrections to the pulse as it propagates within the plasma.

Today many lasers operate in the relativistic or blowout regime where the electron oscillation velocity in the laser field becomes relativistic ($a_0 \equiv eE/(m_e c\omega_0) > 1$). In the relativistic regime many non-linear phenomena occur. The laser pulse may be capable of expelling most or all the plasma electrons from its path resulting in a plasma wavelength ($\sim \lambda_{pe}^3$) sized bubble structure that propagates with the laser. Here $\lambda_{pe} = 2\pi c/\omega_{pe}$ is the electron plasma wavelength which is characteristic to electron plasma waves moving close to the speed of light. In the blowout regime electrons may be self-injected into the accelerating phase of the wake and the bubble structure helps to optically guide the laser pulse. While there are many advantages to the blowout regime, it is often difficult to model or diagnose. In Chapter 3 of this thesis, simulations and experimental results are presented to investigate SRS as a diagnostic of LWFA in the blowout regime.

To drive a strong wake in the linear or blowout regime one usually wants the laser pulse length to be on the order of half the plasma wavelength ($ct_{pulse} \sim \lambda_{pe}/2$) depending on its shape, when the pulse is optimized like this it is said to resonantly drive the wake. If the wake driving laser pulse is longer than the plasma wavelength ($ct_{pulse} > \lambda_{pe}$) the density perturbations of the wake may overlap the pulse and result in self-modulation. In the self-modulated regime the laser breaks into a series of pulses each with duration of approximately half a plasma wavelength. The process of self-modulation takes time and the resulting train of pulses is associated with a cascading of the laser frequencies in steps of the plasma frequency. The self-modulated regime can be an effective way of accelerating large amounts of charge, but often has much higher beam emittance and energy spread than the blowout regime.

The process of self-modulation occurs due to periodic variations in the refractive index overlapping the laser caused by the density perturbations of the wake. When laser light co-propagates and overlaps with a positive density gradient it is red shifted, and blue shifted when co-propagating on a negative density gradient. It has been shown that one can control shifts in a second laser pulse by appropriately delaying it from a wake generating pulse [131]. In the short pulse regime ($ct_{pulse} \sim \lambda_{pe}/2$) the wake driving laser pulse sits on a predominately positive plasma density gradient and experiences red-shifting. In Chapter 4 of this thesis, this red shifting mechanism is explored in the blow out regime to optimize mid-infrared radiation production from a LWFA.

1.4 Inertial Confinement Fusion

Inertial Confinement Fusion (ICF) aims to use lasers to drive an imploding fuel capsule to ignite a controlled fusion reaction with the goal of clean and efficient energy production. The fuel capsule typically contains a few milligrams mix of Deuterium (D) and Tritium (T), which when compressed and heated undergoes fusion to produce alpha particles (α) and neutrons (n) as shown below.

$$D + T \rightarrow \alpha(3.5MeV) + n(14.1MeV), \tag{1.2}$$

When significant reactions start to occur the alpha particles may begin to heat the fuel resulting in a self-heating feedback that can lead to ignition where most of the fuel is consumed. Whether directly or indirectly driven, the fuel capsule implodes due to the inward force of its ablating surface. The surface layer of the target is made of material that can rapidly expand from heat and shock waves driven by radiation so that by conservation of momentum there is a large radially inward force on the fuel inside the capsule. In the direct drive approach, such as at the Laboratory for Laser Energetics (LLE), 60 laser beams point directly at the fuel capsule to irradiate it. In the indirect drive approach at LLNL's National Ignition Facility (NIF), 192 laser beams are pointed onto the inner walls of a gold hohlraum to create X-rays in a symmetric oven like environment containing fuel capsule (c.f. figure A.14). Asymmetries in the drive lasers or perturbations on the surface of the capsule may cause asymmetric implosions which can strongly effect the yield. In direct drive ICF, the lasers create an unwanted expanding plasma from gold walls of the hohlraum that may block the lasers path, to hold back the expanding plasma, the hohlraum is typically filled with a light gas mixture such as helium and hydrogen. The gas is quickly ionized by the lasers, creating an under dense plasma ($n_e < n_c$) where LPI can occur. Both direct and indirect drive ICF face challenges with CBET, SRS, and SBS in the low density plasma surrounding the capsule. When ignited the fuel capsules can provide on the order of 100MJ of energy. A 1GW fusion reactor would require about 10 implosions per second. Currently NIF's repetition rate is on the order several hours per shots, however researchers hope to first demonstrate ignition then improve laser efficiency and repetition rate.

1.5 Fluid Modeling and Shock Formation

The fluid description of a laser produced plasma has been explored extensively in the context of ICF. Hydrodynamic processes become relevant for long pulse ($\sim$ns) lasers and long scale length interactions ($\sim$cm), where acoustic processes are relevant and significant ion motion may occur. While a fluid description of a plasma neglects kinetic effects, hydrodynamic equations are often used due to their simplicity and accuracy for large scales of time and space. In hydrodynamic models, emergent properties of the plasma such as temperature and pressure are sufficiently accurate descriptions of the physics.

In ICF plasmas lasers deposit energy to the plasma primarily through inverse Bremsstrahlung [49]. The ponderomotive force of a laser has been shown to cause density depressions in plasmas [19]. Laser self-guiding in density depressions can lead to instabilities such as in beam spraying [60]. In a flowing plasma a laser can be redirected [96], and the ponderomotive force of the laser beam can even cause shocks in super sonic flows. The NIF's lasers are configured to enter a cylindrical Hohlraum through a Laser Entrance Hole (LEH) on the top and bottom (c.f. figure A.14). In this geometry the lasers overlap in the LEH and heat the plasma inside. As the plasma is created and expands inside the Hohlraum it flows out the LEHs passing through the overlapping lasers. The conditions at the LEH are not well known and can have a significant impact on CBET [75]. If the plasma flowing out the LEH is supersonic, the ponderomotive force of the crossing lasers may be able to slow the plasma to subsonic causing shocks which can dramatically alter plasma conditions over relatively short distances.

In this thesis the hydrodynamics of plasmas interacting with lasers is explored in chapters 5 and 6. In Chapter 5 hydrodynamics simulations are used to study the energy transfer between crossed lasers governed by an ion acoustic wave. In Chapter 6 the ponderomotive drag force of a laser beam on a flowing plasma is investigated and theoretical scaling [29] of shock formation is confirmed in hydrodynamics simulations.

Chapter 2

Enhancement and control of laser wakefields via a backward Raman amplifier

2.1 Introduction

The ability to create large amplitude plasma waves traveling near the speed of light using a laser pulse has led to several scientific breakthroughs such as laser wakefield acceleration (LWFA) [21], betatron x-ray sources [1, 45, 99], and terahertz generation [50]. In general the amplitude and application of these plasma waves can be limited by laser diffraction, depletion, and particle dephasing in the LWFA. In the strongly nonlinear, blow-out regime of the LWFA, dephasing of the relativistic electrons from the accelerating fields, the small charge of the accelerated bunch, and inability to accelerate positive charge for uses such as electron-positron colliders are limitations of this blow-out regime. Several different approaches have been proposed to overcome these drawbacks such as combining the blow-out and the direct laser acceleration scheme [135]. Staged LWFA accelerators [111] involve a pre-accelerated electron beam from the plasma "bubble" and a long wake field wave in the second acceleration stage. The alternative scenarios of LWFAs usually involve several laser beams and often employ linear wakes over a long acceleration length [14]. Inevitably they result in an increase in the particle beam emittance and come at a cost of increased size and complexity of the accelerator.

In this chapter we propose another approach, using a Backward Raman Amplifier (BRA) to maintain the driving laser pulse and hence to enhance and control the wakefield generation. Backward Raman amplification and compression[62, 63, 105] has been proposed as a laser amplification scheme; it has, however, seen mixed success in experimental demonstrations [87, 88, 134]. The experimental efficiency of the BRA scheme is reported to be less than 10%, which is below various theoretical predictions [119]. Clearly theoretical understanding of the BRA and of related physical processes remains incomplete. The role of wakefield generation that is emphasized in this chapter is one of these physical processes that have not been discussed before in the context of the BRA. This in spite of the fact that wake generation is an inevitable feature of short pulse propagation in a plasma, which as we will demonstrate, causes a frequency shift of the seed pulse, and thus affects the BRA coupling. While the overall goal for BRA up to now has been to maximize laser pulse amplification, we consider its use as a control mechanism during plasma wake generation. Specifically, we examine the first application of BRA to amplify and sustain a short seed laser pulse while simultaneously enhancing wakefield generation in a plasma. This chapter will review short pulse propagation in the context of LWFA (Section 2.2 A), followed by a theoretical model for the BRA (Section 2.2 B), and present the results of combining the two (Section 2.5.1). We will describe the wake's effects on the BRA (Section 2.6) and use a chirped pump in the BRA scheme in order to enhance the wakefield generation (Section 2.7). Finally, our results are summarized in the conclusion (Section 2.8).

2.2 Introduction of Methods and Basic Processes

The two processes, wake generation and BRA, have been extensively studied on their own. Before examining their nonlinear coupling and interactions we will first review the relevant properties of the linear wake and the backward Raman amplifier. The summary of known results presented below will be useful in further developments of the BRA for the wake field enhancement scenario.

The primary simulation tool in our studies is the relativistic particle-in-cell (PIC) code SCPIC [90] which has been written on the basis of the code Mandor [95] and

Case	Density n_e/n_c	f-number	t_{pulse} [fs]	$T_e[eV]$
1	0.0035	30	30	100
2	0.015	30	30	100
3	0.05	40	100	50
4	0.0035	15	30	100
5	0.0035	13	30	100
6	0.0035	10	30	100

TABLE 2.1: List of all simulations cases.

has already been used in many high intensity laser-plasma applications for electron acceleration and LWFA [67, 78, 81, 82]. As in similar studies [84, 128, 129], we employ a moving window with the speed of light c. Simulations presented in this chapter will be labeled with a case number, corresponding to the seed parameters listed in Table 2.1. In all BRA cases the plane wave pump intensity is $1 \times 10^{14} W/cm^2$, and the wave length is 1.064μm. In addition to PIC simulations we will consider a reduced description of the BRA based on a three wave coupling model. The wave coupling equations provide a useful description of the BRA that can be apply to long time and large distances of laser pump and seed interactions in cases where the multidimensional effects, related for example to laser pulse diffraction, are not dominant.

2.3 Wake Generation

The focus of this section is on short non-relativistic pulses with a pulse duration, t_{pulse} (FWHM), comparable in spatial extent to the plasma wavelength $ct_{pulse} \sim \lambda_p$ (with $\lambda_p = 2\pi/k_p$ and $k_p = \omega_p/c$, where ω_p is the plasma electron frequency and c is the speed of light in a vacuum). The primary effect of short pulses on the background plasma is wake generation in the form of a longitudinal plasma wave at wave length λ_p and phase velocity $v_{ph} \approx c$. We denote in the following such pulses as "seed" pulses with the field amplitude a_1. In the linear approximation, the plasma electron density perturbation associated with the wake, δn_w, is given by [21]

$$\frac{\delta n_w}{n_0}(\zeta, y, z) = -\frac{c/v_{g1}}{4k_p}\int_{\zeta}^{\infty} d\zeta' \sin[k_p'(\zeta - \zeta')] \nabla^2_{\zeta', y, z} |a_1|^2, \tag{2.1}$$

where $\zeta = x - v_{g1}t$ denotes the coordinate in the frame where the seed pulse moves with the group velocity v_{g1} in x-direction, n_0 denotes the background plasma electron density, and where the seed electric field amplitude is given by $a_1 = \frac{eE_1}{m_e c \omega_1} = 8.55 \times 10^{-10}(I_1 \lambda_1^2 [Wcm^{-2}\mu m^2])^{1/2}$ in terms of the intensity of the short seed laser pulse I_1 and its wavelength λ_1 (λ_1 =1.13μm when $n_e = 0.0035 n_c$, where n_c is the critical electron density for this laser frequency), $k'_p = \omega_{pe}/v_{g1}$ and $\nabla^2_{\zeta',y,z} = \partial^2_{\zeta'^2} + \partial^2_{y^2} + \partial^2_{z^2}$ is the Laplace operator. To illustrate the accuracy of this expression, Eq. (2.1), we compare it in Fig. 2.1a with results from SCPIC simulations for a seed pulse having initially a Gaussian envelope with full-half-width-maximum (FWHM) of t_{pulse} =30fs in time (and $l_s = ct_{pulse} \approx 9\mu$m in length) and the peak seed pulse of amplitude $a_1 = 0.205$ in a plasma with density $n_e/n_c = 0.0035$ cf. Ref. [109]. This simulation corresponds to case "1", see herefore Table 2.1 for all simulation cases discussed.

The generation of the wake is not a resonant process but Eq. (2.1) predicts maximum response for $l_s = \lambda_p/2$. Alternatively, longer pulses $l_s > \lambda_p$ give rise to "self-modulated" (SM) solutions where the wake Langmuir wave is generated in the plasma overlapping the laser pulse and couples resonantly to the seed via forward Raman instability.

The simulation shown in Figures 2.1d,e,f, corresponding to case "2" (see Table 2.1) illustrates, the regime of a self-modulated seed pulse with a large-amplitude wake. Except for the higher plasma density, n_e/n_c=0.015, resulting in a shorter plasma wave length λ_p, case "2" has the same conditions as case "1".

To obtain sufficiently high intensities for wakefield generation, laser pulses must first undergo optical focusing. As a result of focusing, the spot size radius of the laser in a vacuum evolves as can be described by: $r(x) = r_0\sqrt{1 + x^2/Z_R^2}$, where $r(x)$ is the radius of the laser spot size that depends on the propagation distance x from the best focus, and on the Rayleigh length Z_R determined by $Z_R = \pi f^2 \lambda$ where f is the mirror's f-number and λ the laser wave length. The Rayleigh length indicates the distance of laser propagation where the laser spot size is doubled in area, reducing its intensity by a factor of $2/\sqrt{2}/1$ in 3D/2D/1D. Since the amplitude of the wake depends on a_1^2 in Eq. (2.1), optimum wake generation requires the driving pulse to be focused close to its diffraction limit r_0 over as long a distance as possible. This can be achieved through the use of large f-number optics; however, physical constraints

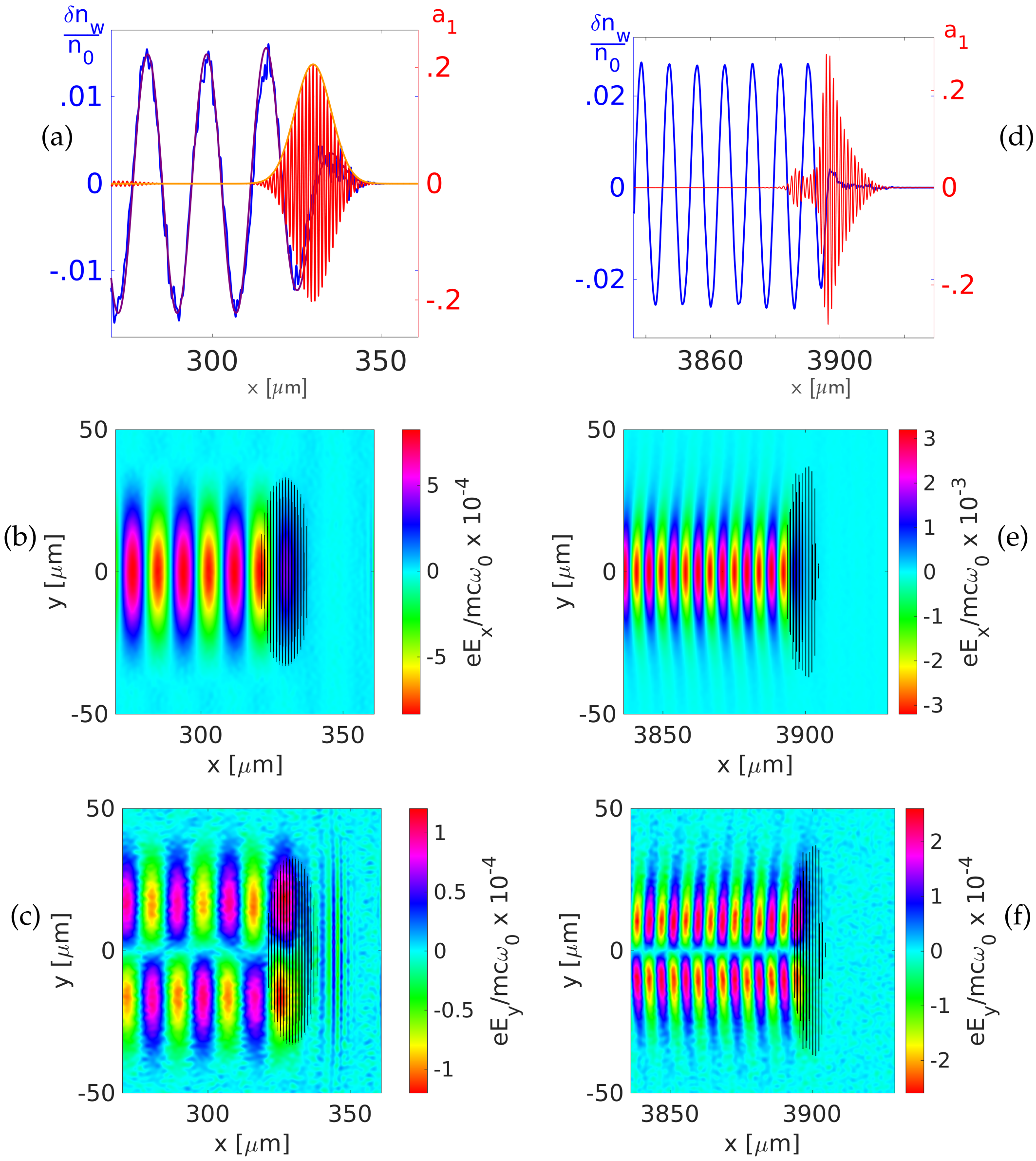

FIGURE 2.1: In the short pulse regime, case "1" (see Table 2.1): (a) 1D cut in x at $y = 0$ of fields and density from 2D PIC and theory, (b) Longitudinal wakefield from PIC, (c) Transverse wakefield from PIC. In the self-modulated regime, case "2": (d) 1D cut of fields and density from PIC, (e) Longitudinal wakefield from PIC, (f) Transverse component of wakefield from PIC. In both cases the initial seed amplitude is $a_1 = 0.205$, and initial seed duration is 30fs. Plasma densities are respectively $n_e/n_c = 0.0035$ (case "1") (a)-(c) and $n_e/n_c = 0.015$ (case "2") (d)-(f), taken at time $t = 1.16$ps in the short pulse regime, and $t = 13.19$ps in the self-modulated regime. Both PIC simulations were run with 30cells/μm resolution, and 9 particles/cell, the simulation domains were 150x300μm for case "1" and 200x200μm for case "2".

on the focusing distance limit the maximum f-number available in laboratory and therefore pulse diffraction can be the significant limiting factor in non-relativistic wakefield acceleration.

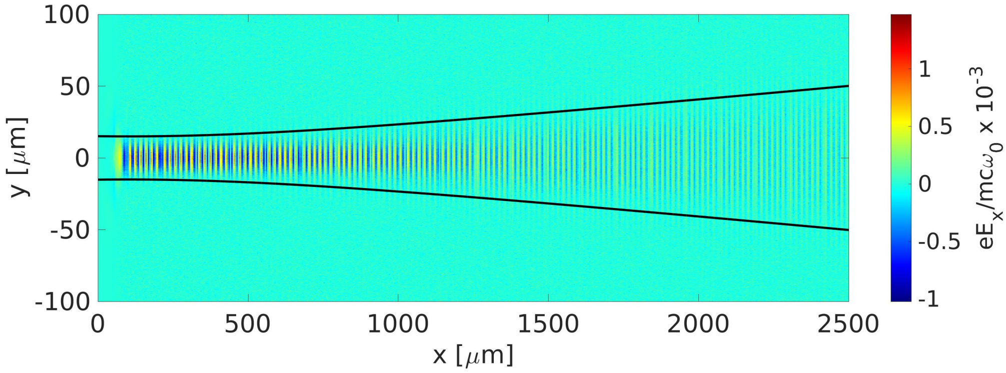

FIGURE 2.2: Wake amplitude vs Propagation Distance reconstructed from subsequent moving window frames of 2D PIC simulation case "4". The laser is focused to the start of the plasma at $x = 100\mu$m and propogates from left to right leaving a wake in the plasma. The theoretical spot size of the laser from is overlayed in black lines with a corresponding Rayleigh length $Z_R = 1200\mu$m. After propagating $2Z_R$ the wake amplitude is reduced to approximatly 1/3 its initial amplitude.

Although electron acceleration in the wake fields will not be discussed at length, we consider a dephasing time/length as a characteristic physical constraint for the BRA coupling. Depending on the plasma density and laser wave length, particle dephasing can occur when particles are accelerated to velocities higher than the phase velocity of the wake. These particles eventually overshoot the accelerating phase and are decelerated. Particle dephasing places a length constraint on the region of acceleration. For a highly relativistic electron, in a wake of radial extent much greater than λ_p, the linear dephasing length can be calculated using the relative velocity difference between the particle and wake, the particle beam moves at velocity approximately c, while the wake's phase velocity $v_{ph} = c\sqrt{1 - n_e/n_c}$. This results in the dephasing constraint $(c - v_{ph})t_d = \lambda_p/2$. Defining the dephasing length as $L_d = ct_d$, results in $\lambda_p/2 = L_d[1 - (1 - \lambda^2/\lambda_p^2)^{1/2}]$ being $\approx L_d\lambda^2/2\lambda_p^2$ for $n_e/n_c \ll 1$, so that the dephasing length can be approximated as [21], $L_d \approx \lambda_p^3/\lambda^2$. For a given laser wavelength and plasma density the dephasing length is a constant barrier on particle acceleration that is underutilized due to the diffraction of low f-number lasers. To ensure the wakefield is maintained over the extent of the dephasing length we propose the use of a backward Raman amplifier which allows for corrections to be applied to the wake generating laser during its propagation in the plasma.

2.4 Backward Raman Amplifier

Backward Raman Amplification (BRA) involves the use of a long pump pulse (ω_0, k_0) counterpropagating with respect to the short seed pulse ($\omega_1 = \omega_0 - \omega_{pe}$, $k_1 = k_p - k_0$). When the two lasers overlap they beat at the plasma frequency, exciting a Langmuir wave ($\omega_L \approx \omega_{pe}, k_L \approx 2k_0 - k_p$) that resonantly couples to the seed. Energy flows from pump to seed, resulting in amplification and compression of the seed.

BRA is typically modeled in 1D with a set of three coupled equations for the slowly-varying field envelopes of the waves, the pump wave a_0, the seed a_1, and the plasma (Langmuir) wave a_L.[63] We will compare in the following the results from PIC simulations of the BRA with solutions of this 3-wave coupling model defined by the following set of equations : [63],

$$\left[\partial_\tau - (|v_{g0}| + v_{g1})\partial_\zeta\right] a_0 = -\gamma_0 a_L \hat{a}_1 \,, \tag{2.2}$$

$$\partial_\tau \hat{a}_1 = \gamma_0 a_0 a_L^* \,, \tag{2.3}$$

$$\left[\partial_\tau - v_{g1}\partial_\zeta + \nu\right] a_L = \gamma_0 a_0 \hat{a}_1^*, \tag{2.4}$$

where $a_{0,1} \equiv eE_0/(m_e c\omega_{0,1})$ are the normalized amplitudes of the electromagnetic fields $E_{0,1}$ of the pump (0) and the seed (1) wave, with $\hat{a}_1 = (\omega_0/\omega_1)^{1/2} a_1$, and with $(\omega_{0,1}, \vec{k}_{0,1})$ as the corresponding frequencies and wave vectors; $a_L = (\omega_L/\omega_0)^{1/2} eE_L/(m_e c\omega_p)$ denotes the normalized amplitude of the Langmuir wave electric field, E_L, with $(\omega_L, \vec{k}_L)$ and the coupling constant reads $\gamma_0 = (k_L c/4)\omega_p/(\omega_L\omega_1)^{1/2}$. The equations are written in the stationary frame of the seed pulse, using the variables $\zeta = x - v_{g1}t$, $\tau = t$, where v_{g0} and v_{g1} are the pump and seed wave group velocities, and where the Langmuir wave group velocity has been neglected. The damping coefficient ν has been added to the Langmuir wave equation (2.4). Its functional form and magnitude can simply be the linear Landau damping $\nu_L = (\pi\omega_{pe}^3/2k^2)\partial f_M/\partial v \,|_{v=\omega_L/k}$ evaluated at the Maxwellian distribution function, f_M. On the long time scale ν_L may be modified due to nonlinear evolution of Langmuir waves that may include electron trapping and wave coupling. Such long time effects do not usually arise during BRA coupling for short seed pulse durations as in the example of Fig. 2.3.

Figure 2.3 illustrates the comparison between PIC simulation and the 3-wave coupling model for parameters corresponding to case "3", leading to the π-pulse solution [63] of Stimulated Raman Scattering (SRS). The seed pulse amplitude at time $t = 3.57$ps, has already experienced amplification with respect to its initial amplitude $a_1 = 0.011$. Amplification is due to the pump laser – propagating from the right to the left – initially at $a_0 = 0.011$, through coupling with the Langmuir wave. The seed pulse duration t_{pulse} is 100fs at FWHM, the plasma density and electron temperature are $n_e/n_c = 0.05$ and $T_e = 50$eV, respectively. The example of case "3", and previous studies based on PIC simulation with similar parameters [84, 101, 128], have been performed in order to validate 3-wave coupling models. Among these studies, Ref. [101] dealt with long time self-similar evolution of 3-wave solutions [63] albeit under idealized conditions of cold background plasma.

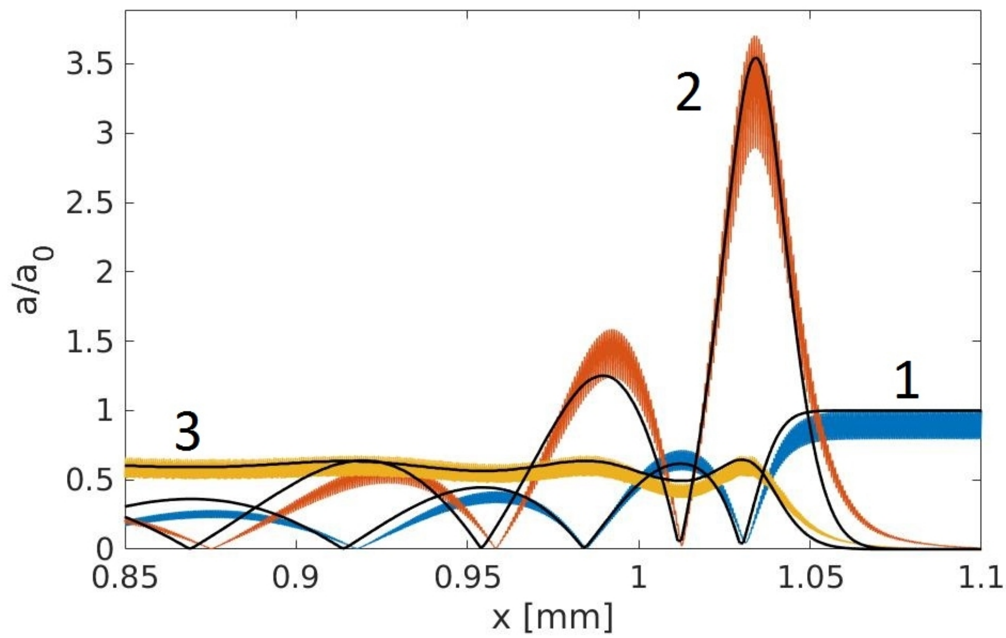

FIGURE 2.3: Comparison of field amplitudes between PIC simulation (color and broadened lines as a result of enveloping the fields) and 3-wave coupling model (solid black lines): for the seed, line **(2)** (with amplitudes $\times 1/2$); for the laser pump, line (**1**); and the Langmuir wave, line **(3)**, at interaction time $t = 3.57$ps. Amplitudes are normalized to the incoming pump amplitude. The PIC simulation was run with a simulation domain of 400μm, 135cells/μm resolution, and 1024 particles/cell.

The good agreement between the 3-wave coupling model (2.2), (2.3), (2.4) and PIC simulation shown in Fig. 2.3 characterizes the initial short time evolution of BRA. As we will discuss below, plasma wake generation and subsequent seed pulse frequency shift, and self-modulation of the relatively long electromagnetic pulse are among nonlinear effects that limit application of a straightforward 3-wave coupling model. Such limitations motivate a need for PIC simulations when the reduced wave coupling models of BRA are derived.

The different modes in k-space are illustrated in Fig. 2.4 that shows the electric field spectrum with electrostatic components in orange and electromagnetic components in blue. The laser pump mode at k_0, the wake at $k_p = \omega_{pe}/c$, the seed at $k_1 = k_0 - k_p$, and the Langmuir waves from Raman coupling $k_L \approx 2k_0 - k_p$. The one dimensional Fourier transform is taken in space and is presented as "FFT(E_y)" and "FFT(E_x)" for the Fourier transform of E_y and E_x, respectively into k_x.

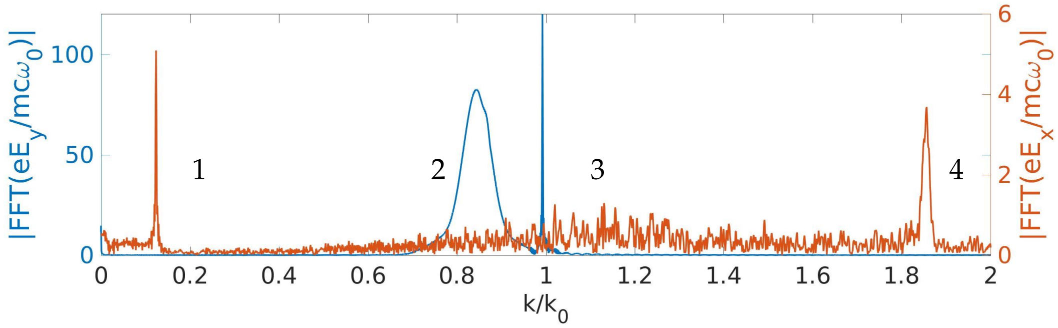

FIGURE 2.4: Electric field power spectrum vs wavenumber, showing electrostatic components in orange and electromagnetic components in blue. (1) Wake at the plasma wavnumber $k_p = \omega_{pe}/c$. (2) Seed at k_1 downshifted by k_p from the pump. (3) Pump defined to be k_0. (4) Langmuir waves from Raman coupling $k_L \approx 2k_0 - k_p$. Simulation parameters correspond to case "2".

2.5 Backward Raman Amplifier for Laser Wakefield Generation

In this section we will demonstrate the control and enhancement of the laser produced wakefield by combining it with the backward Raman amplifier scheme. For this purpose we present the results of simulations where we bring together both effects, BRA and wakefield, in order to optimize and sustain the laser generated wakefield. We first present the results of 2D PIC simulations for the plasma conditions corresponding to the case "1" from the Table 2.1 except for the plane wave limit of the seed and the pump pulses. The discussion of these results will introduce important physical processes related to BRA and wake coupling. Next we will consider BRA as the mechanism that overcomes diffraction of the seed pulse and extends wake generation to at least the timescales on the order of the particle dephasing length, Sec. 2.5.1. In the Sec. 2.6 we will present results on timescales much greater than the dephasing length and consider the effects of wakefield generation on the resonance coupling of the BRA. We will also revise a theoretical model for both laser wakefield generation and backward Raman amplification and consider chirp of the pump, cf. Sec. 2.7, as the mechanism mitigating frequency and wavelength dephasing due to the wake generation.

The results below correspond to a 30 fs FWHM seed laser pulse of intensity $5 \times 10^{16} W/cm^2$ at best focus and a flat top plane wave pump of intensity $1 \times 10^{14} W/cm^2$, in a plasma of density $n_e = 0.0035 n_c$. The parameters are chosen such that the seed efficiently excites plasma waves of the wake $(ct_{seed} = \lambda_p/2)$ in the non-relativistic regime ($a_1 = 0.205$), and the pump intensity is sufficiently low such that it does not produce backscattered SRS from the particle noise before interaction with the seed pulse. The spatial SRS gain coefficient of a pump wave, $G = L_x \gamma_0^2 |a_0|^2 / |\nu_L v_{g1}|$, requires the length $L_x \approx 70mm$ to reach $G > 1$ values for the parameters of this example. This estimate corresponds to the background electron temperature of 100 eV and the SRS Langmuir wave of the BRA at $k_L \approx 0.46 k_D$. Recent work [120] has preposed the use of a "flying focus" on the BRA pump to combat parasitic precursors, such a setup could possibly support larger pump intensities, and hence larger amplification of the seed.

While the low electron density of this example is an optimal choice for the wake generation by the 30 fs laser pulse, the electron temperature of 100 eV is consistent with the experimental conditions of gas jet plasmas [16]. The resulting large ratio $k_L/k_D \approx 0.46$ of the BRA Langmuir wave characterizes the kinetic regime of the SRS [66, 97] and of the Langmuir wave nonlinear evolution [5]. This leads to strong linear Landau damping, $\nu_L \approx 0.14 \omega_{pe}$, and in the nonlinear regime, to electron trapping and to trapped particle modulational instability [5, 66, 97]. However, the nonlinear physics of Langmuir wave evolution – clearly identifiable in simulation results below – becomes important only on time scales longer than the short seed pulse duration, and therefore it has negligible effect on the BRA and the wakefield generation. Consistently, simulations run at different temperatures (50eV, $k_L \approx 0.32k_D$ and 200eV, $k_L \approx 0.65k_D$) show only small variations in the resulting seed and wake amplitudes (see Fig. 2.9a,b).

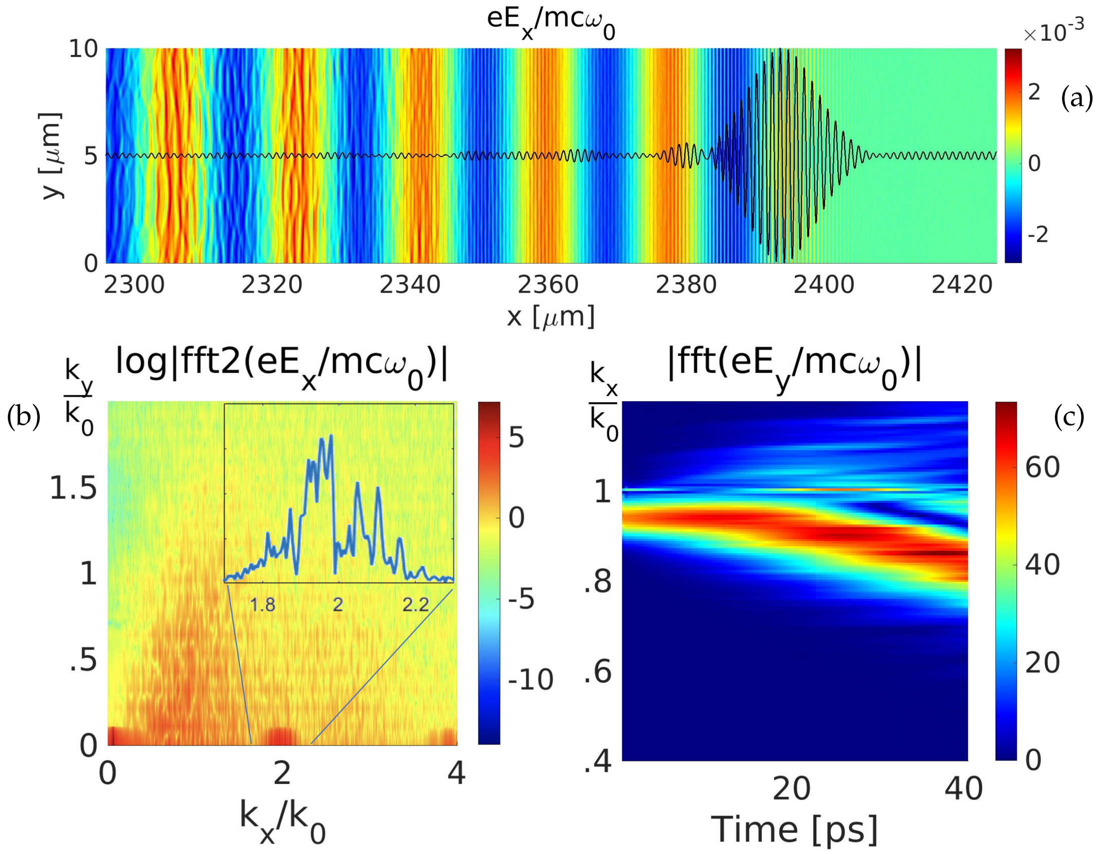

FIGURE 2.5: From 2D plane wave PIC simulation with conditions of case “1": (a) snapshot of the longitudinal electric field in the $x-y$-plane at $t = 8.0$ps (x: propagation direction; red/blue color corresponds to positive/negative field values, respectively); the superposed black line shows the transverse field of the seed pulse and pump from a cut at $y = L_y/2$; (b) spectrum of the electrostatic field in the k_x-k_y plane with subfigure showing a line-out at k_y=0, both at the same time instant as in panel (a); (c) spectrum of electromagnetic field (summed over k_y) as a function of time. The PIC simulation was run with a simulation domain of 10x200μm, 40cells/μm resolution, and 16 particles/cell.

Figure 2.5 shows the results of a 2D plane wave seed and pump simulation with parameters of case “1", the transverse dimension of 10μm and the transverse periodic boundary conditions. The three panels in Fig. 2.5 illustrate the main physical processes involved in the simultaneous BRA and the wakefield generation. Figure 2.5a displays longitudinal electric field of the Langmuir waves due to SRS at

$k_L \approx 0.46k_D$ and the wake at $k_p = \omega_{pe}/c \approx 0.014k_D$. Superimposed is the 1D cut at $y = 5\mu m$ of the transverse electric field due to the seed and the pump lasers. At the time of Fig. 2.5, $t = 8ps$, the wake is well developed and extends hundreds of microns behind the seed. We have estimated the bounce frequency of trapped electrons in the SRS driven Langmuir wave. At the maximum amplitude of the Langmuir wave electric field such that $eE_L/mc\omega_L \approx 0.02$ (see Fig. 2.6) the bounce frequency $\omega_b = (k_L eE_L/m)^{1/2} \approx 9.3 \times 10^{13} 1/s$ and therefore the characteristic trapping time $\tau_b = 2\pi/\omega_b = 67.5$fs is longer than the time of the seed pulse duration and the BRA coupling. On the other hand the freely propagating (to the left) SRS Langmuir waves experience effects of the trapped particles that result in the transverse modulations of their wavefronts on the longer time scale corresponding to the trapped particle modulational instability [5, 66, 97]. This is seen on the left of Fig. 2.5a, far behind the leading seed pulse, and in the two dimensional Fourier transform of the longitudinal fields in Fig. 2.5b. The two dimensional Fourier transforms are taken in space and are presented as "fft2(E_x)" and "fft(E_y)" for the Fourier transform of E_x and E_y, respectively into k_x and k_y, and k_x respectively, (see figure label). The spectra are calculated over the whole length and width of the simulation window and in addition to the wake ($k_x = k_p = 0.059k_0, k_y \approx 0$) and the SRS Langmuir wave ($k_x = k_L = 1.94k_0, k_y \approx 0$) one can see broad continua of transverse components, resulting from the trapped particle modulational instability [5, 66, 97] and the second harmonic of the k_L-wave. The detailed analysis of the spectra about $k_x \approx 2k_0$ has revealed additional components at $k_L \pm nk_p$ and $\omega_L \pm n\omega_p$ (cf. insert in Fig. 2.5b) that result from the coupling between strong wakefield wave (k_p, ω_p) and SRS driven Langmuir wave. Such coupling takes time and we have found no evidence that it actually affects the BRA interaction due to short seed pulse duration. These extra spectral components in the Langmuir wave fields can modify damping and contribute to frequency shifts, but again, only on the longer time scale than the Raman amplification process.

The focus of this chapter is on coupling between two nonlinear processes, wakefield generation and BRA. We will demonstrate that wakefield generation can be extended over large plasma distances due to the BRA enhancing the amplitude of the seed pulse. On the other hand, the presence of several spectral components in the electrostatic fields can lead to deleterious effects such as producing different components at $k_L \pm nk_p$ and $\omega_L \pm n\omega_p$ or adding frequency shifts and instabilities due to trapped particles. These effects influence SRS Langmuir wave on the long time scale. We have also found that the time dependent density modifications due to wake produce k-vector and frequency shifts of the electromagnetic seed pulse. This effect is illustrated in Fig. 2.5c and will become central to our discussions in the following sections (cf. Fig. 2.13b). Despite our focus on short seed pulses (that extend half of a plasma wavelength) to maximize wakefield generation, the wake Langmuir waves are always created by high intensity femtosecond laser pulses, and therefore the BRA schemes should verify whether the wake will introduce frequency and wavelength shifts and account for these decoupling effects in the reduced models based on the three wave approximation.

The characteristic feature of the electrostatic field spectra is large separation between the wake at k_p and the SRS Langmuir wave at k_L (cf. spectral components 1 and 4 in Fig. 2.4 respectively). On the other hand the electromagnetic field components of the seed pulse (marked as 2 in Fig. 2.4) and of the pump (number 3), can overlap for lower densities than in case "2" (see table) of Fig. 2.4. This has been the condition of the current case "1" at $n_e/n_c = 0.0035$. Therefore in the comparison between the three wave coupling model, (2.2), (2.3), (2.4) and PIC simulations in Fig. 2.6 we have plotted the seed and pump wave amplitudes together. Note the remarkable agreement for the Langmuir wave amplitudes near the vicinity of the seed and discrepancy on the longer distance scale due to nonlinear effects including particle trapping and coupling to the wake. The three wave coupling model in Fig. 2.6 was solved with the Langmuir wave damping coefficient, $\nu = \nu_L = 0.14\omega_p$. In general we have found weak dependence at the early time, i.e. until the first maximum in the Langmuir wave amplitude, on the damping coefficient ν (cf. also Ref.[66]).

For optimal BRA coupling the seed pulse duration should be long enough such that its spectral bandwidth is localized to the BRA resonance region; however, optimal wake generation requires the seed pulse duration to be of the order of half a plasma wavelength, $ct_{pulse} \sim \lambda_p/2$, and the SRS growth rate increases with plasma density (shorter plasma wavelength). A chirped pump has previously been used to extend coupling in the BRA to all spectral components of a short seed pulse [123].

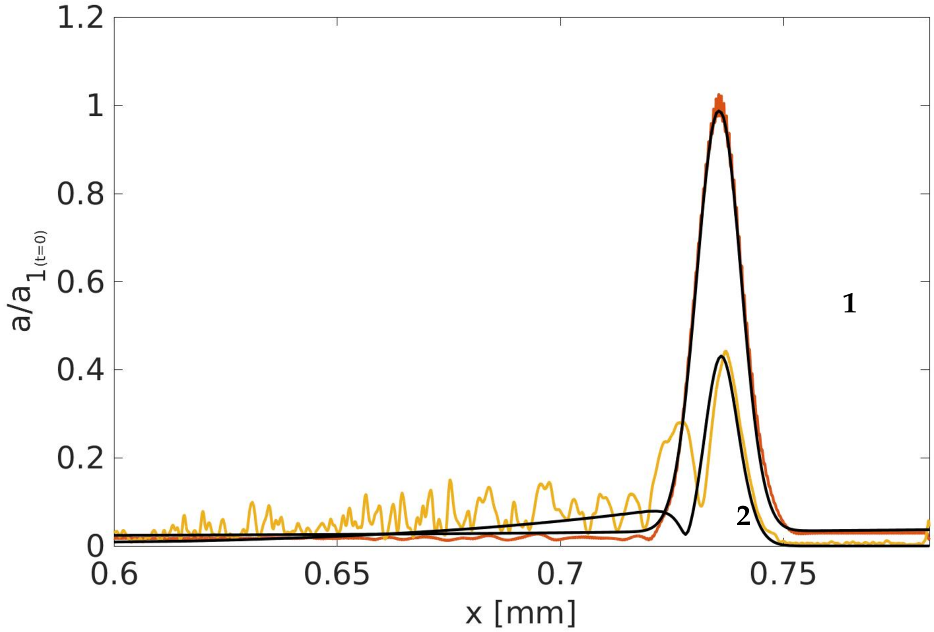

FIGURE 2.6: From 2D plane wave PIC simulation with conditions of case “1": Comparison of field amplitude between PIC simulation (color and broadened lines as a result of enveloping the fields) and 3-wave coupling model (solid black line): for the pump+seed, line (1); and the Langmuir wave, line (2) (with amplitudes $\times$100), at interaction time t = 2.61ps. Amplitudes are normalized to the initial seed amplitude. The PIC simulation was run with a simulation domain of 10x200μm, 40cells/μm resolution, and 16 particles/cell.

The effect of the broad seed pulse spectrum was examined in PIC simulations [93] showing Brillouin coupling [2] in the BRA amplification and compression scheme. Since our seed pulses are short and relatively low intensity, Brillouin coupling is expected to be unimportant. Our plasma density and seed pulse length parameters were chosen to be in a demonstrated region of optimal amplification [129], to be experimentally relevant, and to balance the effects of density on BRA coupling.

2.5.1 Resonant BRA

Figure 2.7 shows the layout of the f/15 simulations (case “4"), where the laser propagation is in the x-direction, and polarization is in the y-direction. In Figures 2.7 we compare the fields resulting from a simulation without BRA, E_x in Fig. 2.7a and E_y in Fig. 2.7b, to the simulation with BRA, Figs. 2.7d and e respectively, for case "4". Figures 2.7c and 2.7f show the difference in each field component between both cases, namely $\Delta E_{x(y)} = E_{x(y)}$(with BRA)$-E_{x(y)}$(without BRA). From the quantity ΔE_y in

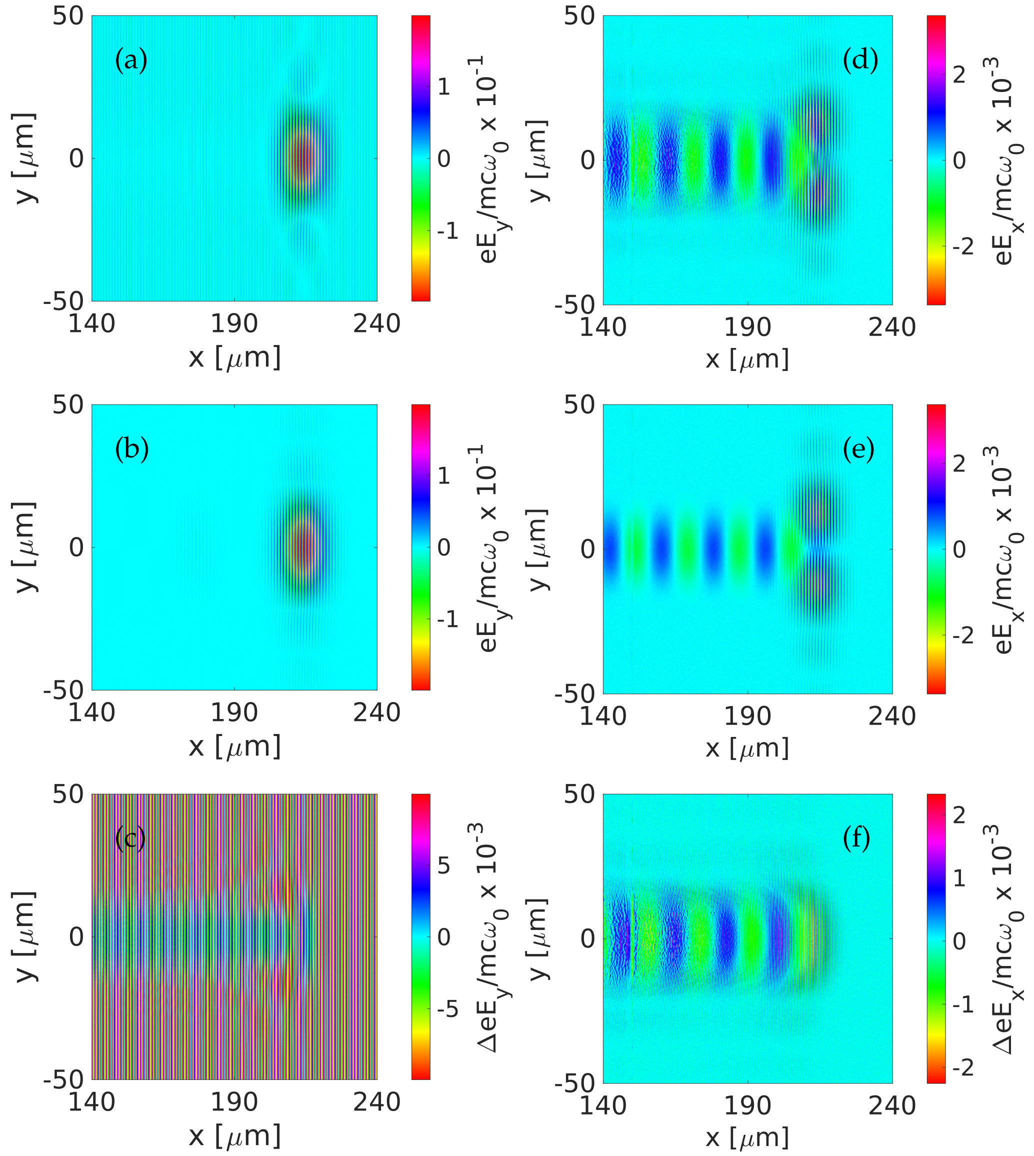

FIGURE 2.7: Simulation results with f/15 at t=0.776ps. Laser polarization is in the y-direction and propagation is in the x-direction. (a) E_y with BRA, (b) E_y without BRA, (c) Difference in E_y between the subcases with and without BRA, (d) E_x with BRA, (e) E_x without BRA, (f) Difference in E_x between the subcases with and without BRA. Subplots (c)& (f) are obtained by $\Delta E_{x(y)} = E_{x(y)}(\text{withoutBRA}) - E_{x(y)}(\text{withBRA})$. Both PIC simulations of case "4" were run with a simulation domain of 150μm x300μm, 30cells/μm resolution, and 9 particles/cell.

Fig.2.7c, it can be seen that the seed pulse is enhanced as it passes through the plane wave pump (oscillation amplitude $\sim 9 \times 10^{-3}$ outside wake region), leaving a trail of depletion in the plane wave pump. Figure 2.7f shows enhancement to the wake due to the amplification of the seed.

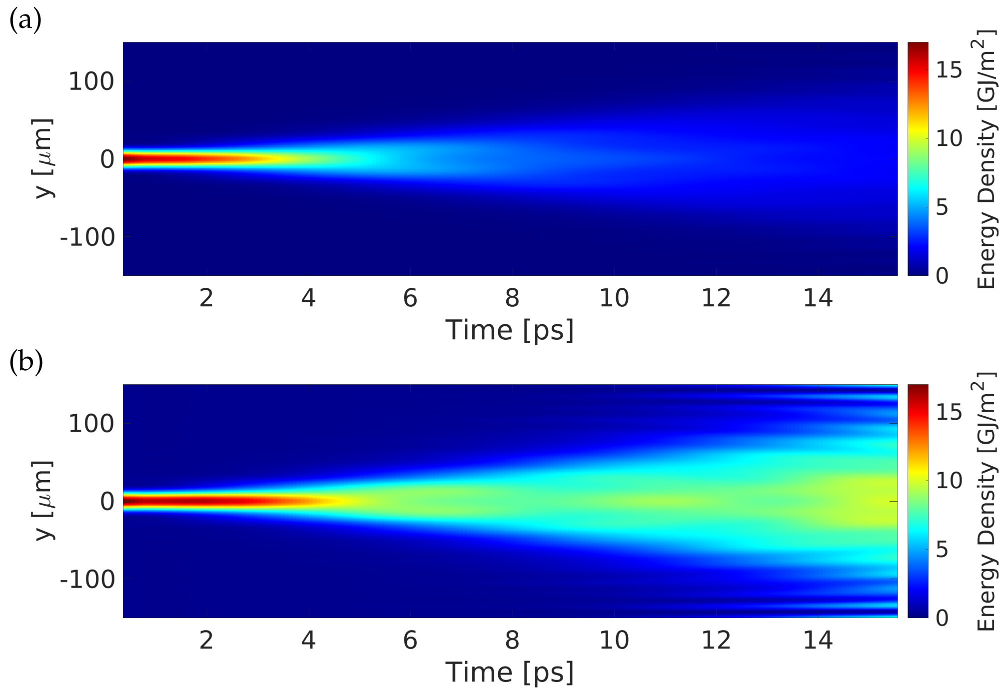

FIGURE 2.8: Evolution of the energy density of a f/15 seed in a plasma vs propagation time and transverse space. a) With no amplifier. b) With a Raman amplifier. The laser is at maximum focus at $t = 0.2ps$. Simulation parameters correspond to those of case “4".

Figure 2.8 shows the time evolution of the seed’s energy density with and without BRA. Without BRA the f/15 seed quickly diffracts resulting in much lower wake amplitude. With BRA the f/15 seed still diffracts, see Fig. 2.8b,however the energy density is nearly maintained by the BRA allowing the seed to continue to produce a large wake.

In the f/30 case, Figs. 2.9a and 2.9d, the amplifier operates faster than the pulse diffraction. This leads to significant enhancement of the pulse and wake until BBRA decoupling by the wake induced frequency shift. In the f/15 case, Figs. 2.9b and 2.9e, the amplifier provides additional energy but at early times the pulse diffracts quicker than it can be replenished. In the f/15 case the competition between diffraction and amplification reaches a balance and the wake is maintained at nearly the same or higher amplitude than the unamplified pulse as shown in Fig. 2.9e. In the higher density plasma of case “2" the seed experiences modulation by its wake (Fig. 2.1d) which – despite diffraction – results in a focusing that increases the seed amplitude with or without the BRA. When a BRA is applied to case “2" there is improved BRA coupling due to the higher plasma density, this results in a large enhancement to

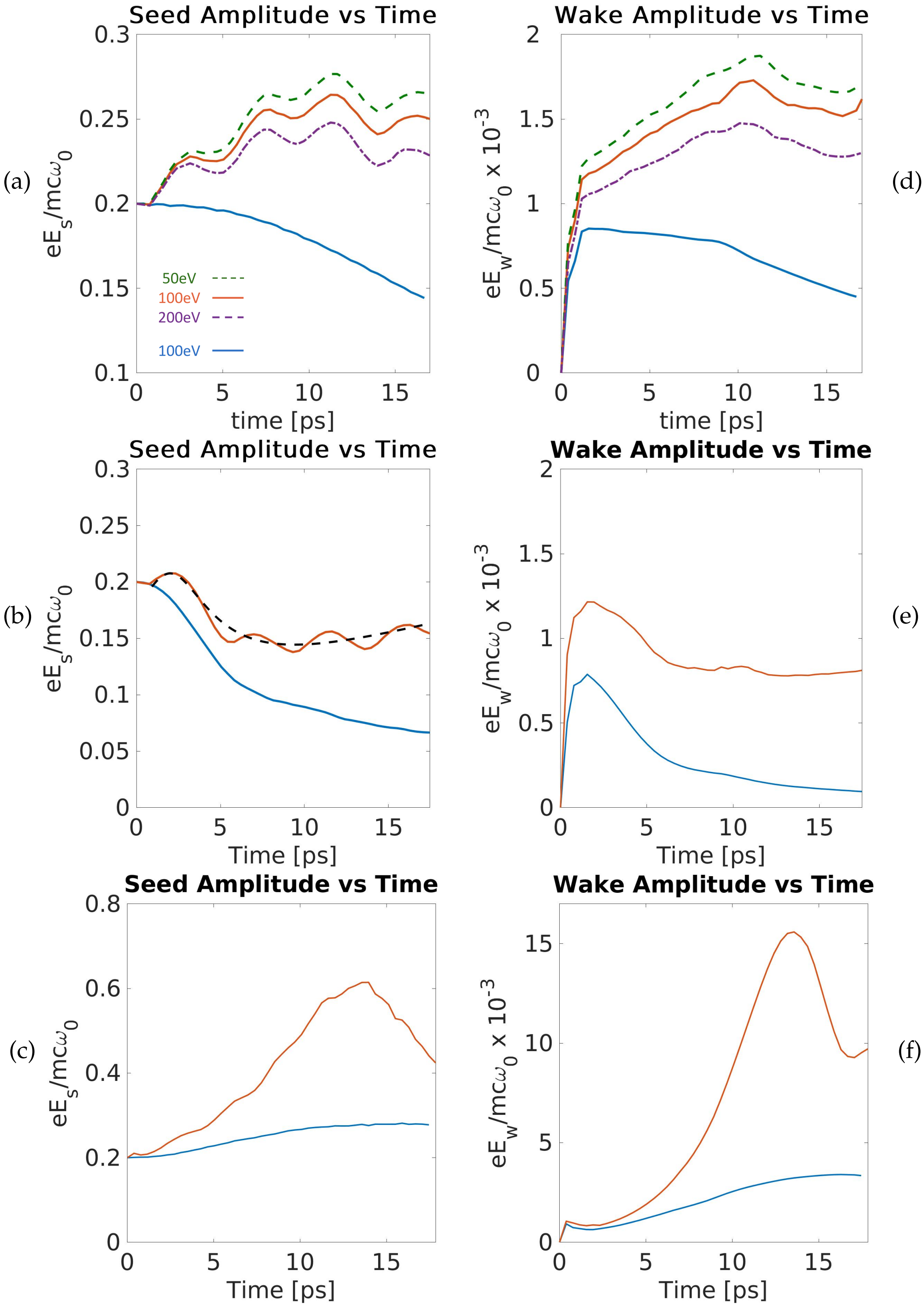

FIGURE 2.9: Comparison of seed and wake amplitudes with (red) and without (blue) BRA. (a) Seed amplitude comparison f/30, (b) Seed amplitude comparison f/15, (c) Seed amplitude comparison SM f/30, (d) Wake amplitude comparison f/30, (e) Wake amplitude comparison f/15, (f) Wake amplitude comparison SM f/30. Simulation parameters correspond to those of case "1" for (a) & (d), case "4" for (b) & (e), and case "2" for (c) & (f).

both the seed and wake amplitude as shown in Figs. 2.9c and 2.9f.

A simple model that is consistent with PIC simulations is proposed to describe competition between diffraction effects and the BRA. Assuming that the seed pulse is well approximated by the Gaussian solution to the wave equation during the BRA interaction, we can model the intensity evolution of the seed taking into account both the effects of diffraction and the BRA. Typical results of the BRA for the wake generation are illustrated in Figs. 2.9. Appart from case “3", all our BRA simulations are in the superradiant regime[20, 38, 105] ($\omega_{pe} \leq 2\omega_0\sqrt{a_0 a_1}$) where the laser pump is strongly depleted as it transfers energy to the seed. This can be clearly observed in Fig. 2.7c displaying depleted pump behind the right propagating seed pulse. With the parameter $0 \leq \alpha \leq 1$ being the efficiency of the energy flow from pump to seed, the incremental energy ($d\mathcal{E}$) transfer from pump to seed during time dt, is $d\mathcal{E}_1 = -d\mathcal{E}_0 = 2\alpha I_0 A_1(t)dt$. Where $A_1(t)$ is the time dependant spot size area of the seed laser, and the factor of 2 arises due to the counterpropagation of the pump and seed. Integrating this results in order to obtain the seed intensity evolution gives

$$I_1(t) = \left[\frac{2\alpha c}{l_s}\int_0^t I_0(t')\left[1+\left(\frac{ct'}{Z_R}\right)^2\right]^{\frac{d-1}{2}}dt' + I_1(0)\right]\left[1+\left(\frac{ct}{Z_R}\right)^2\right]^{\frac{1-d}{2}}, \tag{2.5}$$

where d indicates the spatial dimension of the solution, i.e. d =2 or =3 for 2D or 3D respectively, $l_s = ct_{pulse}$, and Z_R is the Rayleigh length of the seed pulse. The solution to Eq. (2.5) with $\alpha = 0.45$ efficiency and constant pump intensity $I_0 = 1 \times 10^{14} W/cm^2$ shows good agreement with PIC simulation case “4" in Fig. 2.9b. We can estimate the energy transfer from the pump to the seed in order to balance intensity loss due to diffraction. To determine the pump intensity constraint one can set $\frac{\partial I_1}{\partial t} = 0$ to get the solution:

$$I_0(t) = I_1(0)\frac{d-1}{2}\frac{l_s}{\alpha Z_R}\left[1+\left(\frac{ct}{Z_R}\right)^2\right]^{-1}\frac{ct}{Z_R}, \tag{2.6}$$

One can verify this result by substituting Eq. (2.6) into Eq. (2.5) to confirm $I_1(t) = I_1(0)$. Since diffraction results in a dynamic loss in seed intensity, the pump requirements $I_0(t)$ (2.6) are not constant in time, but can be evaluated near the seed's Rayleigh length ($t \approx Z_R/c$, where losses are strongest) to find a constant pump intensity that ensures diffraction is always overcome. As seen in PIC simulation case “4" (c.f. Fig. 2.9b) Eq. (2.6) (with $\alpha = 1$) predicts a BRA pump of intensity $3 \times 10^{14} W/cm^2$ while our BRA pump intensity is $1 \times 10^{14} W/cm^2$ hence it is impossible for our pump to overcome diffraction near the Rayleigh length (simulation time, $t \approx 4ps$) but our pump is more than sufficient to maintain the pulse at later times.

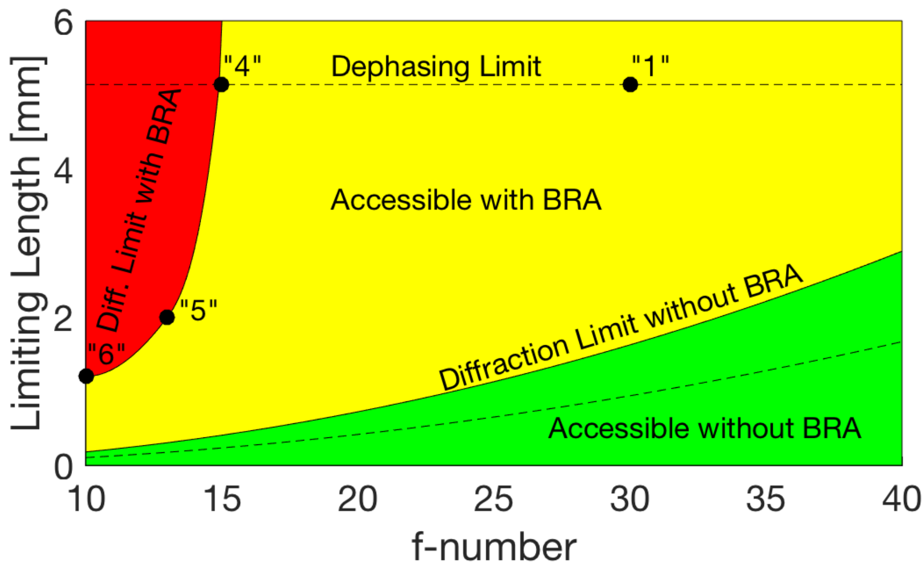

FIGURE 2.10: Limiting lengths for particle energy gain (in 2D) as a function of the seed pulse aperture (f-number) for a 30fs driving pulse in a plasma of density $n_e = 0.0035 n_c$. LWFA without BRA is restricted to the green region; when a BRA is applied diffraction is overcome allowing access to the yellow region. Markers indicate results from PIC simulations (run until the dephasing time t≈17ps). The diffraction limit is defined to be the length at which diffraction causes the wake amplitude to be ≤75% of its maximum unamplified value. The 3D diffraction limit without BRA is shown by the dashed line; the dephasing length remains constant in 3D.

Figure 2.10 summarizes the results of 2D PIC simulations of BRA applied to LWFA. Efficient particle acceleration can be limited by diffraction of the pulse, but is ultimately dictated by the particle dephasing length. For a range of experimentally relevant f-numbers, Fig. 2.10 demonstrates that BRA applied to LWFA can help maintain the wake amplitude of diffracting lasers and allow for better or full use of the particle dephasing limit. Simulation results in our standard parameters (cases “1",“4",“5",“6") show that when BRA is applied to seed lasers with f-numbers of 15 or larger, diffraction is completely overcome, but enhancement cannot continue indefinitely. In the next section we will discuss a new saturation mechanism of the BRA in context to wake generation.

2.6 Loss of the BRA resonance due to the wake effects

In this section we examine the BRA applied to LWFA at times exceeding particle dephasing. For our standard parameters (cases “1" & “4") particle dephasing happens at $t \approx 17ps$ ($t \approx 1.5ps$ for SM case “2"), however BRA and LWFA applications that are not concerned about dephasing (ex: betatron x-ray sources) may still take advantage of the enhancement via BRA.

As shown in Fig. 2.9a and d, at late times the BRA eventually decouples from the seed resulting in a loss of seed and wake amplitude. This decoupling can be attributed to the frequency and wavelength shifts in the seed pictured in Fig. 2.11.

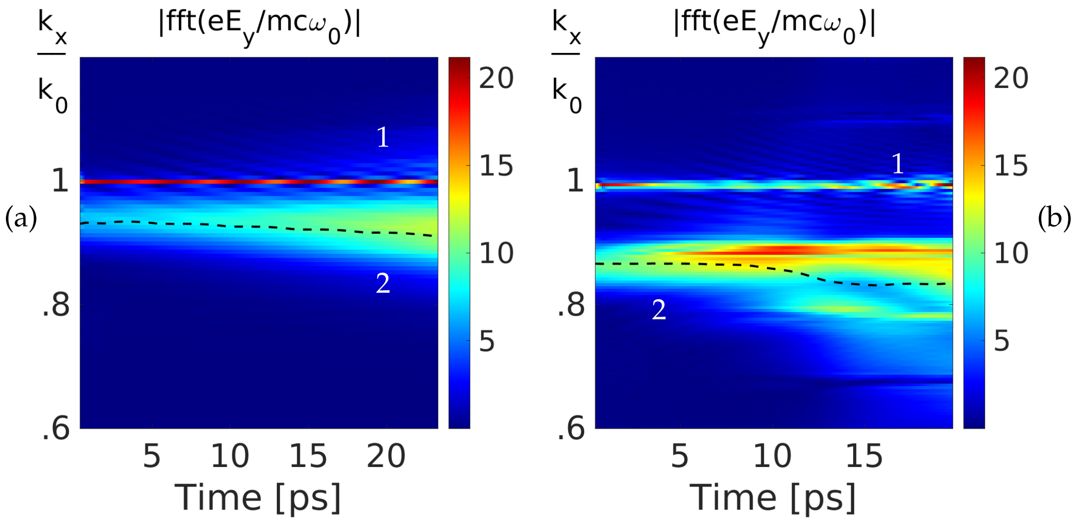

FIGURE 2.11: Longitudinal wavenumbers of electromagnetic fields vs time from 2D PIC Simulations (a) case “1", (b) case “2", showing a decoupling between pump and seed attributed to the red-shifting of the seed. Line **1** is the pump at k_0, line **2** shows the mean wavenumber of the redshifting seed.

It has been shown [107] that a short laser pulse that propagates in plasma with a density profile due to the wake's Langmuir wave, $\delta n_w/n_0$, will develop frequency shifts that can be described by :

$$\delta k_1 = -\frac{\omega_p^2 \tau}{2\omega_1 n_0}\frac{\partial \delta n_w}{\partial \zeta}, \quad \delta\omega_1 = \frac{\omega_p^2}{2\omega_1}\frac{\delta n_w}{n_0} + \delta k_1 v_{g1} \tag{2.7}$$

with $\delta k_1 = \partial_x \Phi = \partial_\zeta \Phi$ and $\delta\omega_1 = -\partial_t \Phi$, where $\Phi(\zeta,\tau) = -\omega_p^2 \delta n_w \tau/(2\omega_1 n_0)$. The characteristic linear dependence of the δk_1 in time, $\tau = t$ is clearly seen in SCPIC simulations and well reproduced by Eq.(2.7). The resulting red shift in the wavelength and frequency follows from the geometry of the wake Langmuir wave, i.e.

the seed pulse propagates together with the front of the wake experiencing constant and predominantly positive density gradient [cf. Eq. (2.7)]. The theoretical curve in Fig. 2.12b has been calculated using Eqs. (2.1) and (2.7), by taking the average of the wave-vector shift (2.7) over the seed pulse length,

$$\langle \delta k_1 \rangle = l_s^{-1} \int_0^{l_s} d\zeta' \delta k_1(\zeta') = -k_0 \frac{\omega_p t}{6\pi^2} \frac{n_e}{n_c} |a_1(0)|^2 \,, \tag{2.8}$$

where we assumed $k_p l_s = \pi$ and $v_{g1} \simeq c$.

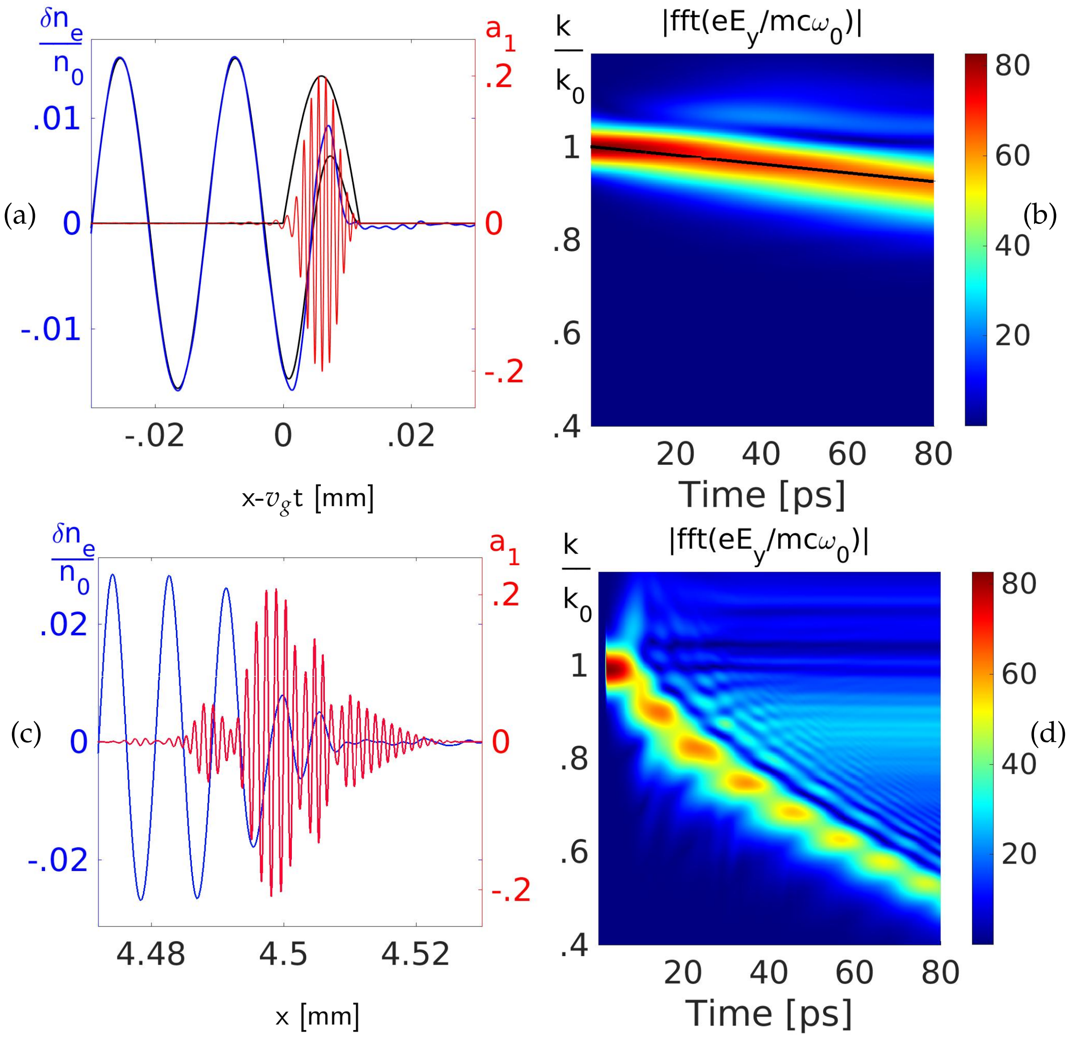

FIGURE 2.12: In the short pulse regime, case "1": (a) Fields and density from 1D PIC and theory at $t = 4.9$ps, theoretical curves overlaid in black. (b) Spectrum of transverse field from 1D PIC with theory shown in black. In the self-modulated regime, case "2": (c) fields and density from 1D PIC at $t = 17.2$ps and (d) spectrum of transverse field from 1D PIC. In both cases the initial seed amplitude is $a_1 = 0.205$, and initial seed duration is 30fs. Plasma density are respectively $n_e/n_c = 0.0035$ and $n_e/n_c = 0.015$. Both PIC simulations were run with a simulation domain of 600μm, 60cells/μm resolution, and 128 particles/cell.

Note that the dramatic frequency cascading of the self-modulated pulse in Fig. 2.12d is entirely due to the coupling between the wake and subsequent stages of forward Raman scattering. This pulse never reaches intensities that would lead to relativistic self-focusing that is usually associated with the self-modulated regime [77].

To model the frequency shifts in the seed, the system of the 3-wave coupling equations[63], Eqs. (2.2-2.4) has to be modified by introducing in Eq. (2.3) the frequency shift term $\delta\omega$. Equation (2.3) in the system Eqs. (2.2-2.4) is hence replaced by

$$[\partial_\tau + i\delta\omega]\, \hat{a}_1 = \gamma_0 a_0 a_L^* \, . \tag{2.9}$$

This modification is necessary to account for the effects of the plasma wake on the BRA. For very short seed pulses as proposed in [64, 105] the wake can have dramatic effects leading to the loss of resonance between BRA modes.

Stationary solutions to Eqs. (2.2),(2.9), and (2.4) are closely reproduce PIC simulations and are displayed in Fig. 2.13b to illustrate the need for including wake generation into theories involving short laser pulses such as BRA.

We will demonstrate how BRA can be applied to enhance the plasma wake when a chirped pump is employed. In absence of a frequency mismatch, i. e. $\delta\omega = 0$ in Eq. (2.3), the waves satisfy the usual matching conditions, $\omega_0 = \omega_1 + \omega_L$, $\vec{k}_0 = \vec{k}_L + \vec{k}_1$ ($k_0 = -k_1 + k_L$ for backscatter, with $k_a = |\vec{k}_a|, a = 0, 1, L$). When we describe the application of BRA to wake enhancement, we will consider short pulses on the order of the plasma wavelength λ_p. Any application of the wave coupling model Eqs. (2.2-2.4) in description of BRA must include a nonlinearity of the wake where $\delta n_w \sim |a_1|^2$ in the phase shift of Eq. (2.7).

Figure 2.13a shows the results of SCPIC simulations at $t = 40$ps for the seed pulse amplitude a_1 and the pump amplitude a_0 and for the normalized amplitude of the electrostatic field, a_L, associated with the wake and Langmuir waves participating in the BRA that are characterized by short wavelength and are concentrated in the front part of the seed pulse. For this simulation with $n_e/n_c = 0.0035$, the initial seed pulse duration is $\tau_L = 30$fs measured as the FWHM of a Gaussian envelope, and the left-propagating laser pump amplitude $a_0 = 0.0091$ (case “1"). An important feature of our BRA application to enhance the plasma wake is the wavelength separation between two main Langmuir wave components, i.e. the wake and BRA excited perturbations. Our attempt to describe interactions, as seen in Figs. 2.13a and b, i.e. BRA and the wake generation, by means of the 3-wave coupling model, Eqs. (2.2), (2.3), and (2.4) can be well approximated by a function for the nonlinear shift in Eq. (2.3) of the following form,

$$\delta\omega = -g_1\sqrt{n_e/n_c}\,\omega_p|\hat{a}_1|^2\,, \tag{2.10}$$

where the numerical constant $g_1 = 1/(12\pi)$ was calculated for a sinusoidal model of the seed envelope. Fig. 2.13b shows the results of this model compared with SCPIC results using numerical solutions to the 3-wave coupling model (line 3), and integrating Eq. 2.10 with the seed amplitude obtained from PIC (line 2). SCPIC simulations show decoupling between the pump a_0 and the seed $\hat{a}_1$ due to the nonlinear evolution of the seed. This more complicated and nonuniform (within the pulse) frequency shift is absent in the 3-wave coupling model which shows further growth of the seed before saturation, leading to a larger frequency shifting rate. Figure 2.14 shows the wake amplitude versus seed propagation time from 1D simulations for different conditions. Figure 2.14a line 2 illustrates the enhancement of the wake amplitude due to BRA coupling until the decoupling at $t = 40$ ps due to nonlinear evolution of the seed.

2.7 Chirping the Pump

To overcome this decoupling due to the shift in the seed, a frequency-chirped pump can be used. To first order, the frequency of the seed follows Eq. (2.7). In this approximation a linearly chirped pump [123] can prolong coupling and increase wake production as shown in Fig. 2.14a line 3 illustrating the enhancement of the wake and delayed decoupling in this case. However, as the seed is amplified it produces a larger amplitude wake resulting in a non-linear change in frequency, and eventually a linearly chirped pump will not suffice to maintain coupling.

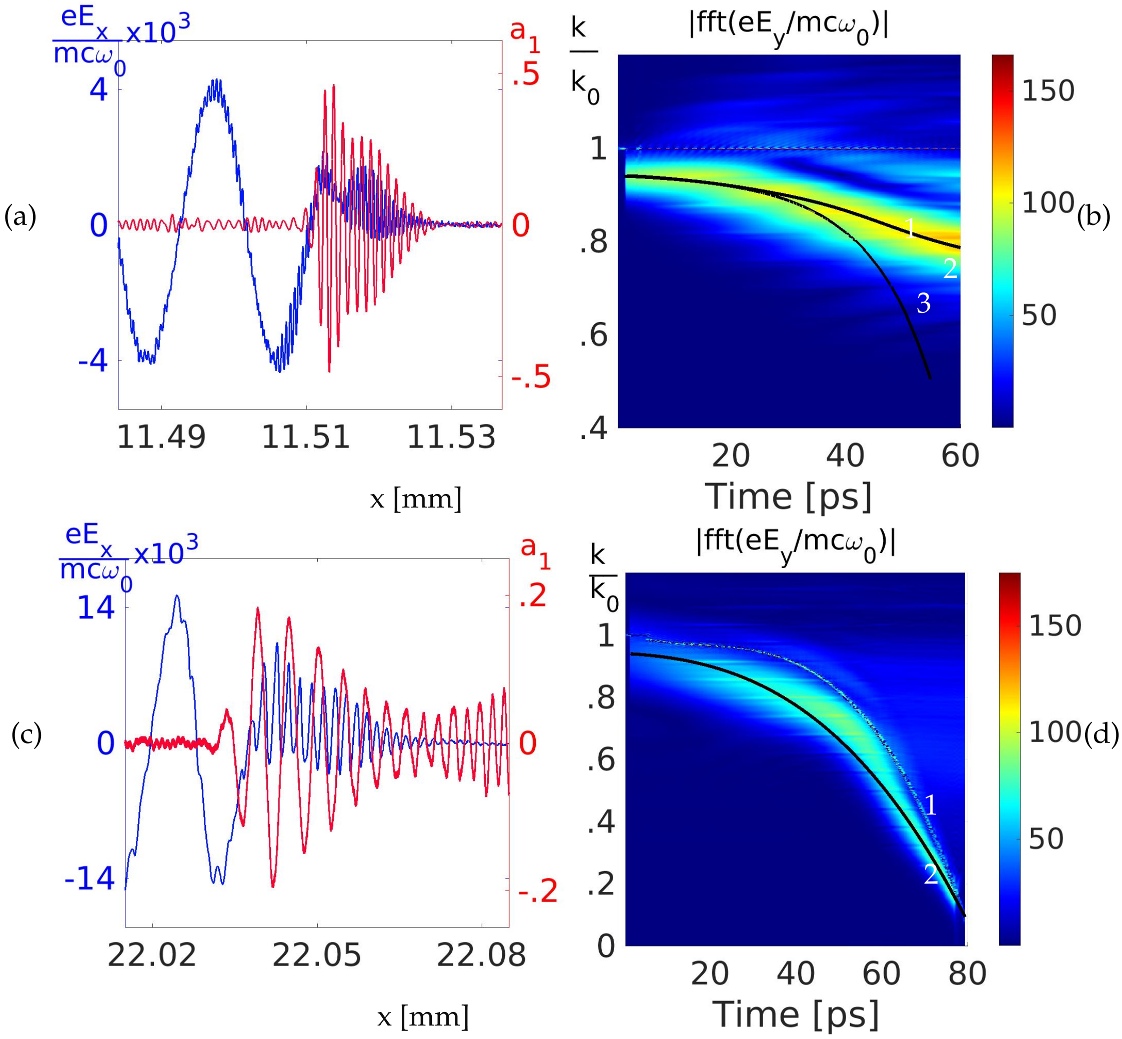

FIGURE 2.13: For the case "4" with constant pump: (a) fields $\hat{a}_1$ and a_L from PIC at t = 40ps; (b) spectrum of transverse electric field (containing both pump and seed components) from PIC and from theory; line **1**: for constant pump (line at $k = k_0$), line **2**: solution to Eq. 2.10 obtained from the amplitude of the seed in PIC, and line **3**: solution to Eq. 2.10 obtained from a numerical solution to the 3-wave coupling model. For the ideally chirped pump: (c) fields $\hat{a}_1$ and a_L from PIC at t = 75ps; (d) Spectrum of transverse electric field from PIC; line (1) : pump field spectrum prescribed by matching condition, solid line (2): seed spectrum obtained from Eq. 2.11. Both PIC simulations were run with a simulation domain of 600μm, 60cells/μm resolution, and 128 particles/cell.

We can estimate this nonlinear frequency change by using Eq. (2.7). This expression can be easily modified to include the effects of Raman amplification through a linear amplitude growth rate [88, 105] by substituting $a_1(0)$ with $a_1(t) = a_1(0)\ (1 + bt)$, with b as a parameter. Substituting this into Eq. (2.8) and integrating leads to the following approximation of the seed's wavenumber shift:

$$\langle \delta k_1 \rangle (t) = -\frac{k_p^3}{k_1(0)} \frac{v_{g1}}{6\pi} \left(a_1^2(0)t + a_1(0)b\, t^2 + \frac{1}{3} b^2 t^3 \right), \tag{2.11}$$

The pump frequency satisfies the usual matching conditions for coupling when $\omega_0(t) = \omega_0(0) + c\,\langle\delta k_1\rangle(t)$, corresponding to a chirped pump with $\omega_0(0)$ as the unshifted frequency. This result can also be obtained by applying similar steps to the theory given in Ref. [102]. Equation (2.11) underestimates the rate of frequency reduction as it does not account for time evolution of the critical density defined by the changing seed pulse; however, by adjusting the parameter b, it was used to model the spectral evolution of the seed (Fig. 2.13d line 2) and to model a pump that would ensure coupling (Fig. 2.13d line 1). Figs. 2.13c and d and 2.14a line 4 demonstrate such a case where the seed and pump maintain coupling throughout the non-linear shifting process with the value of $b = 0.012\text{ps}^{-1}$. One can observe the strong wake enhancement in Fig. 2.14a line 4 as the seed's frequency approaches the plasma frequency, and the seed is slowed down dramatically. Fig. 2.13c shows a snapshot of the pulse and its wake at $t = 75$ps giving a quantitative value for the electric fields, in this simulation $E_w \sim 4.5 \times 10^{10}$V/m. Strong electric fields such as these may be capable of reflecting, and accelerating ions [24].

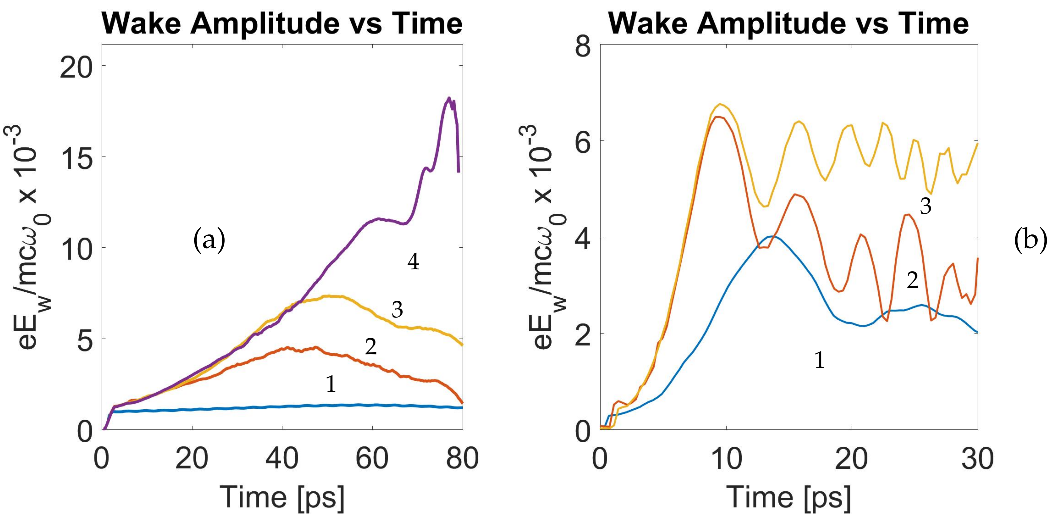

FIGURE 2.14: Wake amplitude versus seed propagation time from 1D simulations for (a) short Gaussian pulses with parameters of case "1" and (b) self modulated pulses with parameters of case "2". In (a), curves correspond to: **1** no pump, **2** constant pump, $\delta k_1 = 0$, **3** linearly chirped pump, δk_1 from Eq. (2.11) with $b = 0$ and **4** ideally chirped pump, δk_1 from Eq. (2.11) with $b = 0.012$ ps^{-1}. In (b) curves correspond to: **1** no pump, **2** constant pump and **3** linearly chirped pump.

To compare our result with realistic experimental conditions, we will consider the instantiations phase of the pump required BRA for coupling. We note that in the presence of a shift in the seed and frequency chirped pump, the Langmuir frequency ω_L may deviate from resonance. However, since our parameters correspond to the superradiant regime[20, 38, 105] ($\omega_{pe} \leq 2\omega_0\sqrt{a_0 a_1}$) where there is increased bandwidth in the Langmuir waves, the interaction is still effective. To satisfy the wavenumber matching conditions $\vec{k}_0 = \vec{k}_L + \vec{k}_1$, one may use the average shift of the seed wavenumber (2.8) (cf Fig. 2.12b) to determine the instantaneous phase of the pump to sustain the original resonance condition: $\Phi_0(x,t) = \omega_0(t + x/c) + \alpha(t + x/c)^2/2$ with $\alpha = -\frac{\omega_0\omega_{pe}}{12\pi^2}\frac{n_e}{n_c}|a_1(0)^2|$, where α is the linear chirp coefficient, and has a value of -2.3x10$^{23}s^{-2}$ for our standard parameters ("1","4","5","6"). Linear chirp coefficients up to 4.47x10$^{23}s^{-2}$ have been obtained in experiments [123] and could be applied to maintain coupling.

When the effects of diffraction are completely overcome and the seed pulse amplitude grows in time, it is necessary to use the non-linear "ideal chirp" prescription (2.11) to maintain coupling. For early times ($t \leq 40ps$) the "ideal chirp" prescription is well approximated by the linear shift (cf. figure 2.14a line 3), but for long durations the non-linear shift is unlikely to be achieved by current CPA lasers. Density tapering[10] could also potentially be used to extend the coupling duration between the pump and the seed. However, the increased plasma densities that are required also result in a greater red-shifting rate of the seed (Eq. 2.8), such that the seed's frequency evolution becomes non-linear and requires a very large, non-linear density gradient that is unlikely to be achieved in experiments.

2.8 Conclusions

We have studied application of the BRA to the enhancement and control of the linear wake generation over a long plasma region. This has been achieved by energy transfer to a wake driving pulse via Raman coupling with a laser pump of low intensity and of long pulse duration. Using PIC simulations we have examined a wide range of background plasma conditions, as well as considered results of the previous BRA optimization studies [129]. Wake generation favors low background electron density, such as $n_e = 0.0035n_c$, where it is possible for a 30fs laser seed pulse to have a FWHM comparable with half of a plasma wavelength $\lambda_p/2$. This optimal pulse length for wake generation at higher plasma densities would require shorter laser pulses and therefore will undermine the efficiency of the Raman amplification process. Also wakes at the lower densities are more effective for particle acceleration [21] as e.g. they correspond to a longer dephasing length. The physics of particle acceleration using wakes that were studied in this chapter will be considered in a separate study. We have examined a range of electron temperatures and focused on the experimentally relevant [16] choice of T_e =100 eV. By varying electron temperature we could alter properties of the resonant Langmuir wave driven by the SRS. At T_e =100 eV and $n_e = 0.0035n_c$ the k-vector of the plasma wave, $k_L \approx 0.46k_D$ and BRA operates in the kinetic regime of SRS [5, 66, 97]. However, at the short seed pulse durations kinetic effects related to trapped particle dynamics are only relevant on much longer time scales than BRA coupling. In addition the strong linear Landau damping limits the growth of SRS of the pump wave thus allowing for the long scale plasma to be considered. With the above choice of plasma parameters we have proceeded to examine the role of BRA in countering the limitations imposed by diffraction of the seed pulse and extending the wake generation to plasmas that are longer than the dephasing length. For a range of experimentally relevant f-numbers, Fig. 2.10 summarizes results of 2D PIC simulations and demonstrates that BRA applied to wake generation can help maintain the wake amplitude of diffracting laser pulses.

A great deal of an initial theoretical insight and motivations for experimental measurements of BRA have been based on the solutions to the simple three wave coupling model [62, 63, 105]. Such reduced models are useful in the understanding of BRA in large scale plasma experiments, provided diffraction of the laser pulses is not a factor and the effects of wake generation are included. We have demonstrated good agreement between PIC simulations and the reduced theoretical description at the early times of the BRA coupling. We have extended validity of the wave coupling models by accounting for the impact of the wake on the SRS coupling. This has been accomplished by including frequency and wavelength shifts in the electromagnetic seed equation that are caused by the time dependent, wake related, plasma inhomogeneities. The loss of the resonance coupling in the BRA that follows has been mitigated by introducing frequency chirp in the laser pump. Theory for the pump frequency chirp, in agreement with long time PIC simulations, showed the possibility of trapping the amplified laser seed pulse in a plasma. This results in a large increase in the wake amplitude and the generation of a shock like structure in the electrostatic field that will be further studied for the enhancement of particle acceleration.

Chapter 3

Stimulated Raman Scattering from a Relativistic Laser Wakefield Accelerator

3.1 Relativistic Laser Wakefield Acceleration

As the driving laser intensity becomes stronger, LWFA reaches a non-linear regime called the blowout or bubble regime for short pulses. At sufficiently high intensity the laser pulse is capable of completely expelling all the electrons from its path. In the relativistic regime LWFA is associated with the formation of a nearly spherical bubble-shaped plasma wave that traps and accelerates electrons.

The bubble regime of LWFA has shown significant performance advantages compared to the linear regime. Particularly the bubble regime allows for self-loading of the accelerated electrons. While the bubble regime of LWFA is currently the more active field due to the availability of short high intensity pulses, significant challenges in diagnosing the bubble shape and particle dynamics are still present.

3.2 Introduction

Compact laser wakefield accelerators (LWFA) are part of a new generation of laser and plasma based accelerators, and are capable of generating GeV electron beams

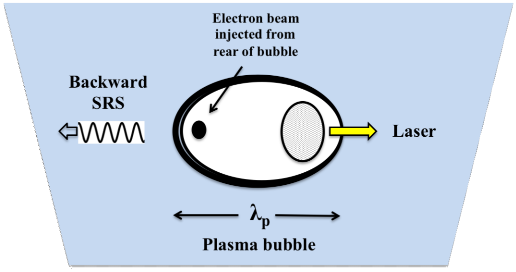

FIGURE 3.1: A schematic of Stimulated Backward Raman Scattering (SBRS) within a laser wakefield plasma bubble. The relativistic plasma wavelength is given by λ_p. The interference of forward going laser light and backward propagating SRS can give rise to a beat structure on the laser wave packet. Image courtesy of Amina Hussein.

over a few centimeters [21, 23, 28, 51, 65, 114, 130]. Plasma wiggler radiation, generated by electron betatron oscillations in wakefield accelerators, results in spatially coherent x-rays having a brightness similar to that achievable with conventional accelerator technology, however with pulses on an unprecedented femtosecond timescale [46, 100].

A LWFA is generated through the interaction of an intense, femtosecond laser pulse with a low density plasma. The ponderomotive force of the high intensity pulse excites plasma waves in its wake that enable the trapping and acceleration of electrons to GeV energies from the longitudinal electric fields in the waves. LWFA at high power is associated with the formation of a nearly spherical bubble-shaped plasma wave that traps and accelerates electrons [70, 86, 92]. Although relativistic plasma waves are produced when the laser pulse duration is less than a plasma period, electron injection and acceleration only occurs when the driving pulse is at relativistic intensity (producing a very large amplitude wave).

SRS is a three-wave interaction that occurs in plasma at densities less than quarter critical ($n_c/4$), where the critical density is $n_c = m_e\omega_0^2/4\pi e^2$. Raman scattering involves the decay of the incident electromagnetic laser wave, ω_0, into an electrostatic plasma wave, ω_{pe}, and a scattered wave, $\omega_{scatt} = \omega_0 - \omega_{pe}$. For $n_e << n_c$, forward SRS results in the generation of relativistic plasma waves with wavelength $\lambda_p \simeq 2\pi c/\omega_{pe}$, while backwards SRS generates non-relativistic waves with a wavelength $\lambda_p \simeq \lambda_0/2$. Interference between forward going light and backward propagating SRS light gives rise to a beat structure on a wave packet, which drives the

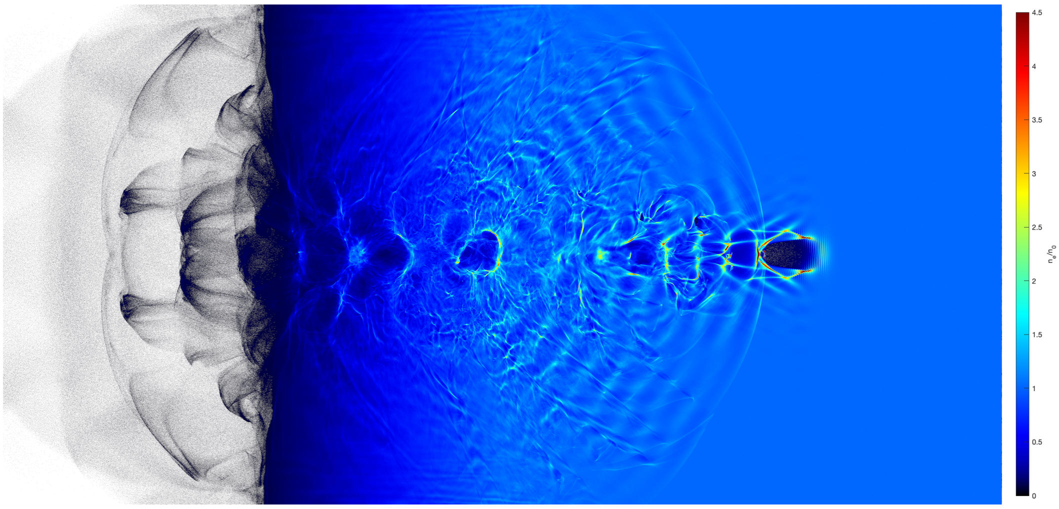

FIGURE 3.2: A SCPIC simulation of LWFA in the Blowout regime. Plasma electron density is shown from low:blue to high:red, while white represents a vacuum. The laser pulse (not shown) is moving to the right and emits SBRS backwards to the left. The simulation domain is 400μm by 200μm with a 100μm vacuum and 100μm linear density ramp leading into the main plasma.

plasma wave growth. A schematic of this interaction is given in Fig. 3.1. In the relativistic regime, where the electric field for electron acceleration is on the order of $m_e c^2/\lambda_p$, the laser pulse duration can be comparable to the growth rate of parametric instabilities such as Stimulated Raman Scattering (SRS) [3, 13, 15, 76, 116].

For "long" pulse durations (nanoseconds), backward Stimulated Raman Scatter (BSRS) can lead to the scattering and redistribution of incident laser light as well as plasma heating and hot electron generation by SRS driven plasma waves. Therefore, the presence of BSRS for inertial confinement fusion-related studies has posed a challenge for effective laser-plasma coupling [31, 132]. The spectral signatures of BSRS have been found to depend on laser intensity. At high intensities with picosecond duration pulses, spectra exhibit broadening and modulation of the frequency spectrum, potentially due to "bursting" of the scattered light from the instability (rapid fluctuations in scattering intensity) [13, 15, 48, 76, 116]. The spectra obtained from BSRS can be used as a diagnostic of the physics of high intensity laser plasma interactions [3, 39, 48, 69, 116].

The duration of BSRS light is related to the propagation time of the laser pulse through the plasma, and therefore can be much longer than the incident laser pulse. The growth rate of the SRS instability depends on the strength of the laser electric field, E, which is characterized by the dimensionless normalized vector potential, $a = v_{osc}/c = Ee/m_e\omega_0 c \propto I^{1/2}\lambda$, where v_{osc} is the peak quiver velocity, ω_0 and λ are the laser frequency and wavelength, respectively, and I is the laser intensity. For high-intensity laser pulses ($I > 10^{18}$ W/cm^2), the peak quiver velocity of an electron in the laser field, can approach the speed of light, resulting in growth rates of the SRS instability that exceed the electron plasma frequency. This is known as the *strongly coupled* regime, and is associated with components shifted to multiples of the plasma frequency ω_{pe}, resulting in a highly broadened spectrum that is not clearly connected to the laser spectrum [3].

Strongly coupled SRS measurements from picosecond duration ($\simeq$ 800 fs) pulses have been previously made, with the width of the spectra exceeding the plasma frequency [15]. A transition from classical to anomalous (broadened) BSRS with increasing laser intensity has been observed experimentally from 600 fs laser pulses [13]. Additionally, measurements from 450 fs high-intensity (I $> 10^{18}$ W/cm^2) laser pulses have yielded spectra with large-amplitude modulations [116]. Experimental measurements of BSRS from 120 fs pulses at sub-relativistic intensities have also been reported, where the amount of backscattered light was found to decrease at low pressures due to the ponderomotive expulsion of electrons along the laser axis [61]. BSRS measurements have also been made during LWFA with laser powers up to 8 TW (max intensity of $\simeq 2 \times 10^{19}$ W/cm^2). Kaganovich et al. [42] observed saturation of BSRS signal due to strong self-focusing at increasing gas pressures (plasma densities). Their experimental results were consistent with BSRS generation in the weakly nonlinear regime, where the growth rate of SRS is positive only in a very narrow spectral region, resulting in a frequency component of the laser pulse with a width less than ω_{pe}.

The observation of these broadened, highly modulated BSRS spectra, which are not predicted by the standard parametric theory of SRS, highlights the role of nonlinear dynamics in electron plasma wave generation [124, 125]. For high-intensity, short-pulse interactions, very large amplitude electron plasma waves are produced, in which the oscillating electrons can have very high velocities. To account for the relativistic correction to electron mass (nonlinear detuning) at these intensities, Kono and Škorić included a nonlinear term in their one-dimensional model of SRS in a weakly-collisional plasma [47]. Their theory predicts a saturation of backscattered light for lower laser pump amplitudes, given by the ratio of the electron quiver velocity in a laser pump field to the speed of light ($eE_0/m_e\omega_0 c$), revealing quasiperiodic structures. However, with increasing pump strength, pronounced spectral broadening and chaotic bursting of back-scattered emission was observed, indicating a transition to chaos and eventual loss of coherent modulation. 1D-PIC simulations of Raman backscattered spectra were found to produce modulated spectra with increasing complexity as a function of pump strength, agreeing with experimental measurements from a 0.8 ps laser pulse by Darrow et al. [15]. Therefore, the extreme broadening of backscattered spectra may indicate scattering from many unstable plasma modes in the strongly coupled regime due to loss of coherence of plasma waves during wavebreaking [3, 15, 127]. Broadening may also be due to spatiotemporal localization (bursting) of the Raman scattered light within the laser pulse from a rapid saturation of the SRS instability [125, 127].

Additionally, electron injection and trapping during LWFA is connected with the wave breaking of electron plasma waves (EPW) having phase velocities approaching the speed of light [127]. Instabilities with a self-modulating laser pump can couple to relativistic plasma waves, creating new sidebands in the forward spectra, and contributing to the growth and ultimate breaking of these EPWs [3, 127]. However, severe side scattered SRS has been found to degrade electron beam quality in LWFA through the seeding of filamentation instabilities in the electron beam, as well as erosion of the incident laser pulse [69].

Backward SRS in the strongly coupled (strongly non-linear) regime during LWFA have not previously been observed experimentally. In the bubble regime of LWFA, the importance of this phenomenon is also unclear, however the backward SRS may generate large amplitude short wavelength plasma waves in a partially "evacuated" plasma bubble, which may affect the dynamics of electron injection and acceleration in this regime. Previous studies motivate measurements of backscattered spectra produced at these ultra-short pulse durations as a diagnostic of the interaction. Of particular interest is the efficiency and control of electron self-injection, which may potentially enable optimization of the LFWA mechanism, and generation of electron beams with higher charge. The utilization of BSRS to generate a counter-propagating photon beam could also be used to produce X-rays by the Compton scattering of photons on energetic electrons accelerated by LWFA [41, 86]. This method of all-optical Compton scattering could produce X-rays with a wide range of energies up to 1 MeV, and could provide a compact alternative to existing linear electron accelerator devices. Photons generated via BSRS may provide a more tractable realization of all-optical Compton scattering as compared to the use of two separate ultrashort pulses to generate the energetic electron-photon interaction.

In this chapter we will describe experiments and supporting simulations conducted using the HERCULES laser system at the University of Michigan to produce experimental measurements of backward SRS generated during LWFA in the strongly coupled regime. Resultant backscattered spectra were found to be highly modulated and significantly red-shifted beyond 830 nm in cases where electrons were accelerated. A correlation between the total amount of BSRS and charge of the accelerated electron beam was observed for laser powers exceeding 100 TW. The amount of BSRS (characterized by the intensity of the of the measured spectrum beyond 830 nm) was also found to increase as a function of plasma density at these powers. For laser powers above 100 TW, where the ponderomotive force of the laser is higher, the BSRS signal was significantly less red-shifted, while still correlating with electron beam charge and plasma density. For laser powers below 50 TW, no such correlations were observed. Therefore, it is clear that the red-shift broadening of the backward SRS spectrum is associated with increased electron beam charge in a LWFA. These experiments were explained by two-dimensional PIC simulations that indicate growth of BSRS until the wakefield bubble is evacuated of electrons due to relativistic self-focusing of the laser. Simulations and experiments indicate that measurement of backward propagating SRS may be used as a diagnostic of bubble formation and trapped electron charge within the bubble. A summary of the experimental setup is given in Section 3.3, PIC simulations are described in Section 3.4, and results and analysis are given in Section 3.5.

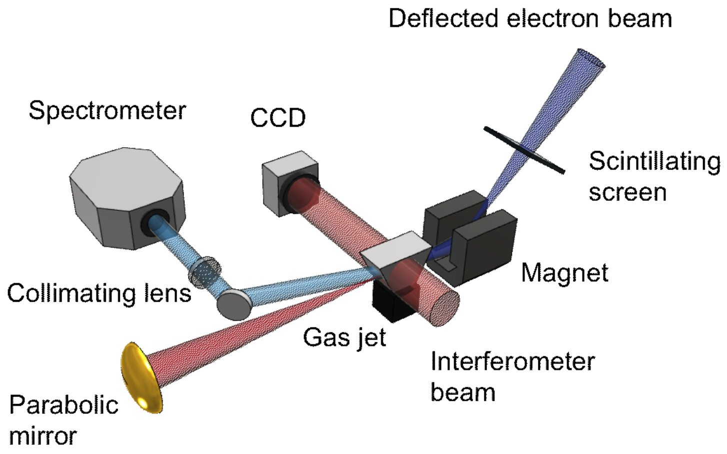

FIGURE 3.3: Experimental setup for measurements of Backward Stimulated Raman Scatter on the HERCULES laser (800 nm, 30 fs, 30-200 TW, 4" diameter, focused with an f/10 parabola, shown in red). Interferometry measurements of electron density were made using a probe beam from a pellicle in the main interaction beam. An Ocean Optics HR2000 spectrometer resolving 200-1000 nm was used to measure backscatter signal (shown in blue) from the rear of the gas nozzle. Backscattered light was collected using an aluminum mirror and collimated through a 37 cm focal length lens of 125 mm diameter. Electron energies were measured using a 0.8 T magnetic spectrometer, a scintillating LANEX screen and a CCD camera. Image courtesy of Amina Hussein.

3.3 Experimental set-up

At the University of Michigan, experiments were conducted using pulses from the HERCULES Ti:sapphire laser system. The laser operates at a wavelength of 800 nm wavelength, with 30 fs pulse duration. Pulses with powers between 20-180 TW (1.3×10^{19} W/cm^2 - 1.1×10^{20} W/cm^2) were focused using an f/10 off-axis parabolic mirror onto a pulsed gas jets generated from gas jet nozzles between 1.55 mm and 5 mm in diameter. A deformable mirror was used to correct the laser wave front and produces a focal spot with a full-width-half-maximum (FWHM) of 10 μm. Gas jet pressures up to 800 psi helium gas were utilized, yielding plasma densities up to 6×10^{19} cm^{-3}. Backscattered light was collected using an aluminum mirror at an angle of 5.5 degrees from the nozzle and collimated onto the entrance slit of an Ocean Optics HR2000 spectrometer (200-1100 nm). The laser spectral bandwidth was measured to be 30 nm; therefore, for backscattering measurements the area under the red-shifted spectrum was considered for wavelengths beyond 830 nm. This region of the spectrum was chosen for the analysis of backscattered spectrum to avoid errors due to scattered laser light inside the target chamber. An electron spectrometer (using a 0.8 T magnet) with a LANEX phosphor scintillating screen and a charge coupled device camera enabled electron energy detection between 47-800 MeV. Interferometer measurements of the plasma density were obtained using a transverse probe beam. A schematic of the setup is given in Fig. 3.3.

3.4 Particle-in-cell simulation parameters

Two-dimensional simulations of a 30 fs, 800 nm laser pulse at 100 TW and 140 TW in varying plasma densities were performed using the relativistic particle-in-cell (PIC) code SCPIC [91], which has previously been used to study electron acceleration in the bubble regime [68]. These simulations provide additional insight on the kinetic processes leading to SRS and particle loading. Simulations used a domain of 400μm $\times$ 200μm with resolution 12,000 $\times$ 6,000 cells (30/μm) and 16 particles per cell. Electron plasma densities of (0.5-2)$\times 10^{19}$ cm^{-3} were simulated, assuming a plasma temperature of 50 eV. Several diagnostic probes were placed on the simulation boundaries to record SRS as the laser propagates in the x-direction through the plasma. A linear density ramp of 100 μm from vacuum to full density was included in the model.

3.5 Results and Analysis

A typical experimental backward SRS spectrum obtained from 30 fs laser pulses at 50 TW and 180 TW is given in Fig. 3.4a. A background backscatter shot without gas is also plotted for comparison. Dramatic broadening and modulation of the BSRS spectrum is observed at all powers with the generation of an electron beam. The laser intensity is centered at 800 nm and a red-shift in the BSRS spectrum was considered as signal extending beyond 830 nm (with 30 nm taken as the nominal spread of the laser wavelength). The integrated area under the red-shifted BSRS

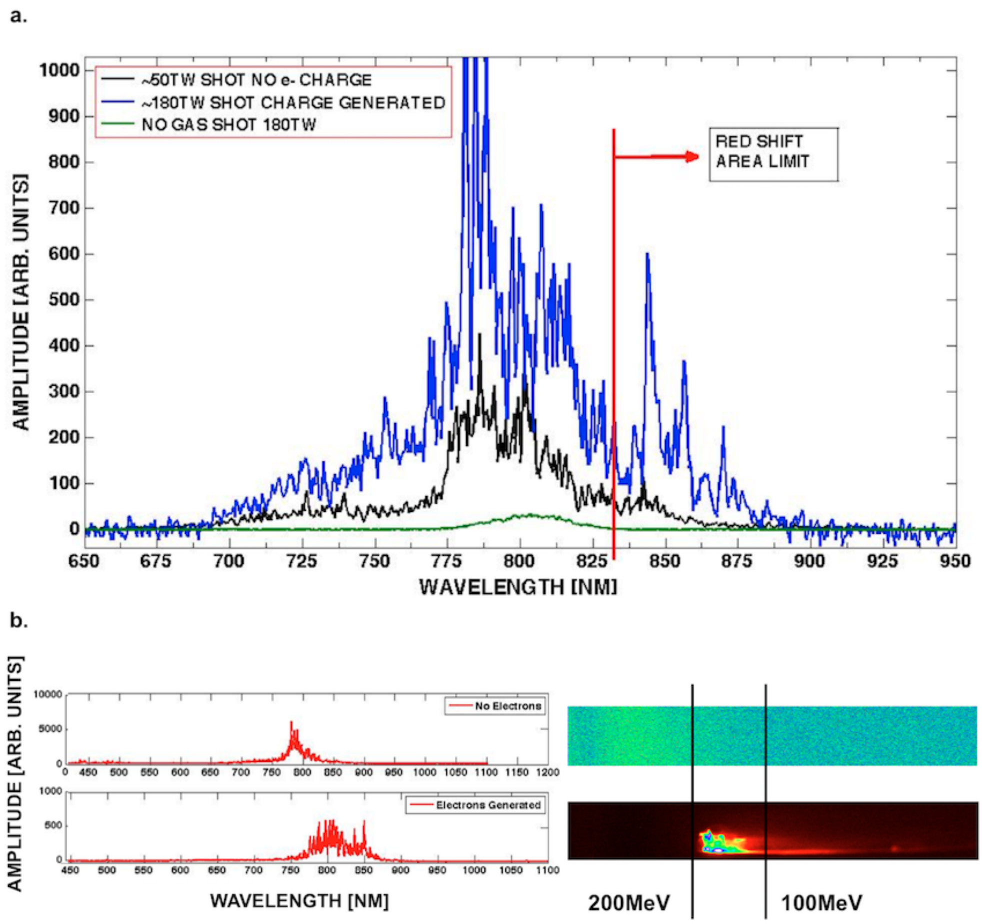

FIGURE 3.4: **(a.)** Example of Backward SRS spectrum, from a 180 TW laser shot producing electrons (blue), a 50 TW shot in which electrons were not produced (black), and a 180 TW shot without gas (green). The red-shifted area was considered as signal extending beyond 830 nm. **(b.)** Measured BSRS spectra and associated electron signal on the scintillating LANEX screen, demonstrating broadening and red-shifting of the BSRS spectrum with electron generation. Image courtesy of Amina Hussein.

spectrum is taken as a Figure of Merit of the total BSRS signal, since the measured spectrum is approximately symmetric.

The spectrum measured without gas in Fig. 3.4a resembles the laser spectrum and results from stray light scatting inside the target chamber. We note here that the signal level within the incident laser spectrum is negligibly weaker than the shots with gas and the BSRS signal dominates the signal. The observed broadening and modulation of the BSRS spectrum are similar to measurements at longer pulse durations in the strongly coupled regime [13, 15]. However, the modulation of the spectrum is more pronounced than any previously observed.

A comparison between BSRS spectrum with and without electron generation is

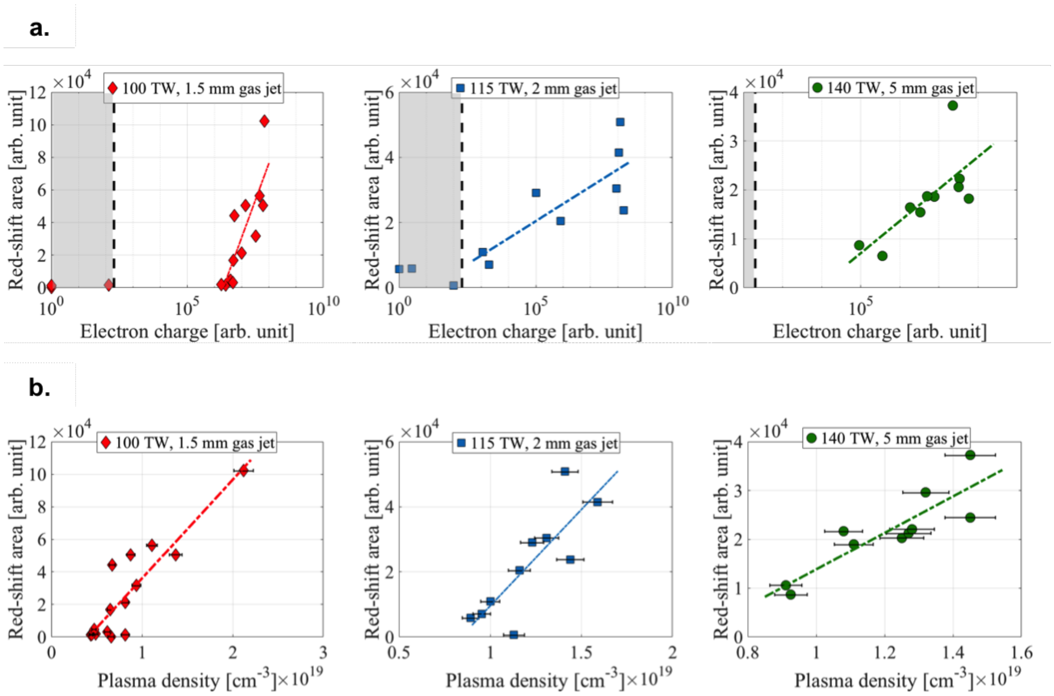

FIGURE 3.5: Total area under the red-shifted BSRS spectrum (representing the total BSRS signal) for helium gas at 100 TW, 115 TW and 140 TW, for three gas jet nozzles, where the quoted length refers to the nozzle diameter. Error bars for the integrated spectrum are the same size as the plotted points. **(a)** The total BSRS signal is plotted as a function of integrated charge, on a semilogarithmic scale. An increase in BSRS signal as a function of charge generation is observed for all powers, and all nozzle diameters. Linear least square fits are shown to demonstrate this trend. Electron signal below 200 counts is considered background, and is represented by a shaded region. Error bars for the integrated charge are negligible relative to the signal and are not plotted. **(b)** The total BSRS signal was found to increase as a function of plasma density at each laser power and nozzle diameter. Linear least square fits are shown. At all powers and nozzle densities, the electron charge was found to increase with plasma density. Image courtesy of Amina Hussein.

given in Fig. 3.4b with associated electron signal. These measurements were obtained at a laser power of 30 TW, using a 1.5 mm diameter gas jet nozzle. No specific correlations between the energy spread of the electron beams and the amount of SRS were observed. Electron measurements shown in this figure correspond to signal on a scintillating LANEX screen. The contrast on each LANEX image is optimized to show variation in the signal above background, therefore these images do not have the same contrast.

BSRS broadening was found to increase with electron beam charge generation and plasma density for laser powers at and above 100 TW. Measurements taken at 100 TW, 115 TW and 140 TW, with 1.5 mm, 2mm and 5 mm diameter gas jet nozzles,

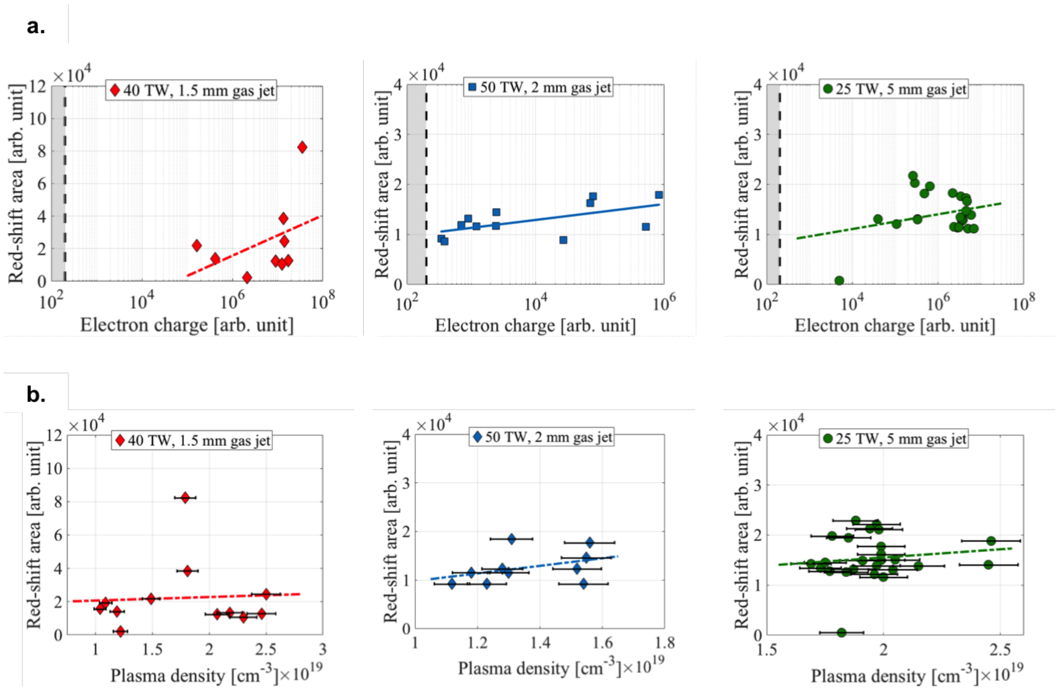

FIGURE 3.6: Total area under the red-shifted BSRS spectrum (representing the total BSRS signal) for helium gas at 50 TW and below, for three gas jet nozzles, where the quoted length refers to the nozzle diameter. Error bars for the integrated spectrum are the same size as the plotted points. **(a)** A clear correlation between BSRS signal and electron charge does not emerge. Linear least square fits are shown. Electron signal below 200 counts is considered background, and is represented by a shaded region. **(b)** No clear relationship between plasma density and the total BSRS signal is observed; linear least square fits are shown. Additionally, no relationship between the electron charge and plasma density was found for powers at and below 50 TW. Image courtesy of Amina Hussein.

respectively, are presented in Fig. 3.5. The integrated signal in the red-shifted BSRS spectrum as a function of electron charge is plotted on a semilogarithmic scale in Fig. 3.5a, and as a function of plasma density in Fig. 3.5b. Plasma density was determined from interferometry images. Electron charge, presented in arbitrary units, refers to the integrated intensity of electron signal from the electron spectrometer onto the scintillating screen. All signal below 200 counts is considered background, and for all shots with near-zero BSRS there was also near-zero electron charge. For each power and nozzle diameter, each plotted point corresponds to a single laser shot from a single experimental run. The plotted data reflects all points obtained under the same experimental conditions (quoted power and nozzle diameter).

Linear least squares fits are plotted for each power to highlight an increase in BSRS as a function of electron charge on a semilogarithmic scale in Fig. 3.5a, and an increase in BSRS as a function of plasma density on a linear scale in Fig. 3.5b. However, these fits should not be considered as a scaling, as the process is highly non-linear. Note that the y-axis varies for each plot, with the total BSRS signal decreasing with increasing power. The total BSRS signal is greatest at 100 TW. Additionally, at laser powers at and above 100 TW, the integrated electron charge was found to increase with increasing plasma density. Correlations between BSRS signal and electron and plasma density are persistent for all nozzle diameters.

For powers of 50 TW and below, variations in the BSRS signal with electron charge is not as dramatic. This is shown in Fig. 3.6a. For helium gas targets at powers from 25 TW to 50 TW a clear trend is not obvious across all powers and nozzle diameters. Linear least squares fit to the semilogarithmic plot as a function of electron charge are shown for comparison with Fig. 3.5a; the total red-shifted area (and therefore the total BSRS), does not appear to increase with the total charge in the resultant electron beam. Additionally, at these lower powers, no clear correlation between the total BSRS signal and plasma density is observed. This data is plotted in Fig. 3.6b. Linear least squares fits are also shown for comparison with the high power trends in Fig. 3.5b. No obvious trend between BSRS signal and plasma length can be observed.

The results in Fig. 3.5 and Fig. 3.6 indicate that the intensity and broadening of the BSRS spectrum is most pronounced at powers above 100 TW. Additionally, the

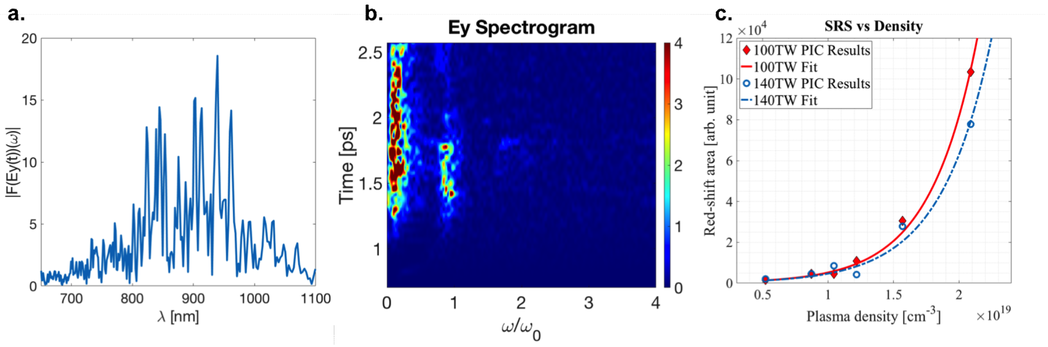

FIGURE 3.7: PIC simulations reveal a finite duration to the backward traveling SRS signal. **(a)** An example BSRS sample from PIC simulations indicating red-shifting and broadening as observed in experimental data. **(b)** Time history of backscattered light frequency from PIC simulations at the diagnostic probe from the 100 TW laser in a plasma of density 2.09×10^{19} cm^{-3}. Results show plasma waves at $\omega_{pe} \simeq 0.1\omega_0$ (electrostatic waves that reach the probe) and backward traveling SRS at $\omega_{SRS} \simeq 0.9\omega_0$. **(c)** An increase in the total BSRS signal as a function of plasma density is observed, where total signal is represented by the integrated red-shifted area of the simulated BSRS spectrum beyond 830 nm. Exponential fits to the data are shown.

total area under the BSRS spectrum at powers below 100 TW was nearly half that observed for higher laser powers. The increased bandwidth and "spikey" structure of BSRS spectrum may indicate very rapid growth rate and saturation of the backward SRS instability at high laser powers.

Two-dimensional PIC simulations enabled a detailed analysis of BSRS generation in a LWFA. Backward SRS signal was observed in the SCPIC simulations and the time history was recorded. Typical probe spectra are shown in Fig. 3.7a and Fig. 3.7b. Numerical simulations also reproduce the highly modulated experimental backscatter spectrum, indicating the applicability of PIC simulations for modeling SRS in LWFA interactions.

The BSRS spectrum was recorded from PIC simulation probes for laser powers of 100 and 140 TW. The integrated area under the red-shifted spectrum (beyond 830 nm), representing the total BSRS signal, is plotted as a function of plasma density in Fig. 3.7c. Each point corresponds to a single laser event. An increase in the total BSRS signal as a function of plasma density is observed and exponential fits to the data are shown. As in the experiments, PIC simulations show an increase in the SRS signal with plasma density and confirm that the 100 TW laser pulse typically produces more SRS than the 140 TW laser pulse.

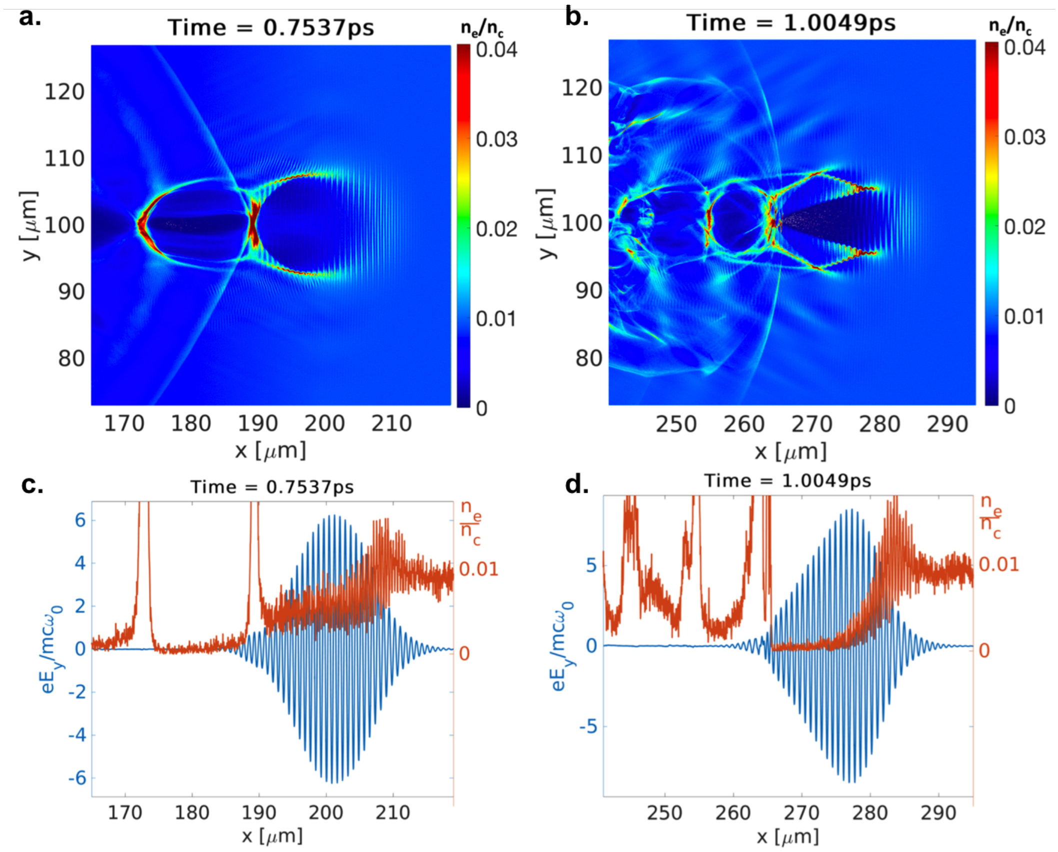

FIGURE 3.8: 2D PIC simulations of the 100 TW laser in a plasma of density $1.56 \times 10^{19}\text{cm}^{-3}$. **(a)** Plasma electron density at t = 0.75 ps, showing finite electron density inside the LWFA bubble resulting in SRS. **(b)** Plasma electron density at t = 1.00 ps, showing complete evacuation of electrons from the LWFA bubble due to relativistic self-focusing of the laser. **(c)** Laser amplitude and plasma density versus propagation distance 1D cut along x, at $y = L_y/2 = 100\ \mu m$ at t = 0.75 ps and **(d)** t = 1.00 ps.

PIC simulation results reveal a finite duration to the BSRS signal, as shown in the backscatter diagnostic probe of Fig. 3.7b. While bubble formation begins almost immediately upon the laser entering the plasma, the bubble is not completely evacuated of electrons until the laser is self-focused to sufficiently high intensity. During the period when there is finite electron plasma density inside the bubble, BSRS is produced from the laser, and once the bubble is evacuated the scattering stops.

A significant BSRS signal is observed only in simulations where the laser intensity is below the critical intensity for complete blowout of electron density in a bubble [57]. For 100 TW laser power, complete blowout occurs at plasma densities below 1.2×10^{19} cm^{-3} (c.f. Fig. 3.7c). At higher densities, the balance between the ponderomotive force of the laser and the force that arises due to the charge separation may allow for finite electron density inside the bubble.

For all the sub-critical laser intensity simulations, the evacuation of the wakefield bubble and termination of backward SRS occurred at about 700 fs after the laser entered the plasma. Fig. 3.8 shows 2D simulations and line-outs of plasma electron density as a function of time, indicating complete evacuation of electrons due to relativistic self-focusing of the laser after a propagation time of about 1 ps (simulation time).

By using the theory for complete electron blowout given by [21, 57], one can estimate the amplitude of the laser pulse required for complete evacuation of the bubble, for a given plasma density. Laser pulses with initial electric field amplitude below this threshold will first undergo relativistic self-focusing before complete evacuation of the bubble occurs.

Combining the laser amplitude requirements with a theory for relativistic self-focusing [108, 110] results in a critical length parameter that determines the distance the laser pulse must travel in the plasma before it[21]s bubble is completely evacuated:

$$z_c = Z_R \sqrt{\left[\frac{a_0}{a_c} - 1\right]\left(1 - \frac{P}{P_c}\right)^{-1}} \tag{3.1}$$

$$a_c = \left[\frac{b^2}{2} + \frac{1}{2}(b^4 + 4b^2)^{1/2}\right]^{-1/2} \tag{3.2}$$

$$b = \Big((k_p r_0)/2\Big)^2 \tag{3.3}$$

where the real component of z_c is defined to be the critical length for blowout (i.e. restricting $a_0 \leq a_c$ and $P > P_c$), Z_R is the laser Rayleigh length, a_0 is the initial normalized amplitude of the laser, a_c is the critical laser amplitude for complete blowout [21, 57], P/P_c is the ratio of the laser power to the critical power for relativistic self-focusing with $P_c = 17(\omega/\omega_pe)^2[GW]$ [21], $k_p = \omega_{pe}/c$ is the plasma wavenumber, and r_0 is the diffraction limited spot size of the laser.

The amplitude threshold for the blowout increases with density, and the critical power P_c for the relativistic self-focusing decreases with higher plasma densities. This results in a nearly constant critical length z_c (independent of plasma density) for lasers with initial amplitude below the threshold for complete bubble evacuation. The critical length (3.1) $z_c \approx 33$ μm for 100 TW lasers, corresponding to $n_e > 1.2 \times 10^{19}$ cm^{-3}. To estimate z_c from the simulation results, cf. Figs. 3.8c,d, one could evaluate the distance between the beginning of the homogeneous plasma at the end of the density ramp, $x \approx 200\mu m$ in Fig. 3.8c, and the location of the fully evacuated electron density in Fig. 3.8d at $x \approx 270\mu m$. The extent of the critical length, $z_c \approx 70\mu m$, observed in PIC simulations corresponds very well to the region of the strong BSRS signal and corresponding duration of the scattered signal at the probe (see Fig. 6b and note that due to the counter propagation of the laser and its SRS, the duration of the scattered light signal is expected to be $2z_c$/c). Also, $z_c \approx 70\mu m$ remains nearly constant in all runs at different plasma densities. The observed discrepancy between theoretical prediction and PIC results are well within the expected limitation of the scaling argument in Equation (3.1) and rough estimates based on the simulation results in Fig. 3.8.

While finite densities in the bubble (due to sub-critical laser amplitudes for the full electron evacuation) result in the strongest BSRS signals in the short PIC simulations, there is always SRS present due to plasma density at the front of the bubble (see Fig. 7d), which is also lower for higher intensity lasers because of the steeper density gradient. This BSRS produced at the front of the bubble is less prominent in the short PIC simulations.

PIC simulations indicate that BSRS signal persists until the wakefield bubble is evacuated due to relativistic self-focusing of the laser. Thus, measurement of backward propagating SRS appears to be a result of non-zero electron plasma density within the bubble. One explanation for this correlation is that the BSRS instability may be seeded by noise produced by electron injection into the bubble during self-focusing. Consequently, BSRS signal and time-resolved backscattered spectra may be useful as a diagnostic of bubble formation and trapped electron charge.

3.6 Conclusions

In this chapter, we present PIC simulations and theory in support of the first experimental measurements of backward strongly coupled SRS in the bubble regime of LWFA. The observed spectra are unlike those observed in previous experiments, and are characterized by a very spikey structure, consistent with 2D PIC simulations, cf. Fig. 3.7a. The observed backward Raman spectrum is correlated with enhanced electron charge in the accelerated beam. For laser powers at and above 100 TW, the integrated BSRS spectrum at wavelengths beyond 830 nm (representing the total BSRS signal) was found to increase with both electron charge and plasma density. For laser powers below 100 TW, no such correlation was observed.

Two-dimensional PIC simulations show a correlation between BSRS signal and plasma electron density within the laser wakefield bubble. For increasing laser intensities, the intensity and duration of the BSRS signal decreases as electron density within the bubble is rapidly depleted. The BSRS signal is enhanced when the electron density in the bubble is nonzero. The broadened, highly modulated spectra obtained from backscattered light are also observed in PIC simulations. They are results of rapid variations in the background plasma conditions during bubble formation and scattering of backscattered light on the secondary plasma wakes that are formed behind the primary bubble containing the short laser pulse. It has has been shown in the past that wake formation contributes to the frequency shifts of the laser pulse [58, 103], and this in turn affects spectrum of the scattered light.

These results indicate that at highest powers (100 TW and above), the bursting, broadening and modulation of the BSRS frequency spectrum is associated with increased plasma density within the LWFA plasma bubble. The existence of a non-evacuated wakefield bubble, as indicated by backward SRS signal, may be related to enhanced electron injection, resulting in enhanced charge in the accelerated electron beam. The correlation observed between electron beam charge and BSRS is likely due to density fluctuations in the plasma, which may be due to the injection of electrons into a LWFA bubble. These fluctuations can provide a seed for the development of the BSRS instability. Therefore, it is possible that fluctuations due to BSRS can provide feedback for electron injection.

Chapter 4

Mid-Infrared Generation from a Laser Wakefield Accelerator

4.1 Introduction

The mid-IR spectral region corresponds to wavelengths of 2-20μm. Mid-IR contains the frequency range of molecular vibrations and therefore is of significant interest for a number of scientific and technological applications [32, 40]. Ultra-short mid-IR pulses with intensities exceeding $10^{14} W/cm^2$ have exciting applications in new frontiers, from mode-selective photochemistry [7] to driving attosecond, phase-matched high-order harmonics in the X-ray regime [89]. Additionally, for long wavelengths the critical power for self-focusing is reduced, and the critical density reduced, making LWFA driven with long-wavelength pulses an exciting opportunity for the generation of MeV-scale electron beams at moderate laser intensity [56, 133].

The development of ultra-short duration mid-IR sources optimized for power, efficiency and spectral performance is particularly challenging [83, 85]. Nonlinear photonics, fiber lasers and frequency combs are some approaches that have yielded mid-IR sources with sub-picosecond duration [33, 40, 85], and high-intensity, short-pulse mid-IR sources are typically produced using optical parametric amplifiers pumped by 1μm lasers. However, the production of wavelengths extending beyond 5μm is limited by the suitability of nonlinear crystals [83], and for conventional nonlinear optical methods the total energy of mid-IR sources is limited by material damage or instabilities arising from nonlinear beam propagation, as well as the availability of suitable materials.

The use of a plasma medium to generate long wavelengths through non-linear self-phase modulation would mitigate challenges posed by optical damage. In a plasma medium the generation of laser driven plasma waves also produces frequency shifts in laser pulses [22, 79, 118, 131]. As demonstrated earlier in Chapter 2 of this thesis, the co-moving refractive index gradient due to plasma density variations produces time dependent frequency shifts in the laser. This is because the formation of the plasma wake (density perturbation) results in a refractive index gradient that is co-moving with the driving laser pulse. An example of the bubble geometry is shown in figure 4.1. For relativistic laser intensities ($a_0 > 1$) in underdense plasmas ($\omega_{pe}/\omega_0 \ll 1$), the real component of the refractive index seen by the laser is [21, 108]:

$$\eta_r(z) \simeq 1 - \frac{\omega_{pe0}^2}{2\omega_0^2} \frac{n_e(z)}{n_e(0)\gamma(z)} \tag{4.1}$$

where ω_{pe0} is the plasma frequency and ω_0 is the laser frequency. The relativistic factor $\gamma(z) \simeq \sqrt{1 + a(z)^2}$ and the density n_e may vary both transversally and longitudinally. A gradient in $\eta_r(z)$ along the laser propagation axis, due to density gradients in the plasma will lead to an increase and/or decrease of the laser frequency. In the bubble regime of LWFA, a density up-ramp ($dn_e(z)/dz > 0$) at the leading edge of the plasma bubble creates a region of negative gradient in the refractive index ($d\eta_r(z)/dz < 0$), causing a frequency downshift (red-shift) of the laser pulse. Light at the tail of the wake experience a positive refractive index gradient, and therefore are frequency upshifted. In this way, the pulse develops a positive frequency chirp, and a negative group velocity resulting in pulse compression [118]. This results in non-linear dispersion of the laser pulse, and the measurement of this spectrum has been suggested as a diagnostic of wakefield dynamics [17]. At the center of the wake which consists of plasma ions, light will experience negligible frequency variation. Given that the pulse duration is on the order of the plasma wavelength during LWFA, the body of the pulse will reside in a region of falling electron density, and red-shifting will dominate the spectral evolution, producing wavelengths extending into the mid-IR. Additionally, the pulse duration will be compressed by the local reduction in group velocity associated with red-shifting of the spectrum.

Previous studies have explored the production of pulsed mid-infrared radiation

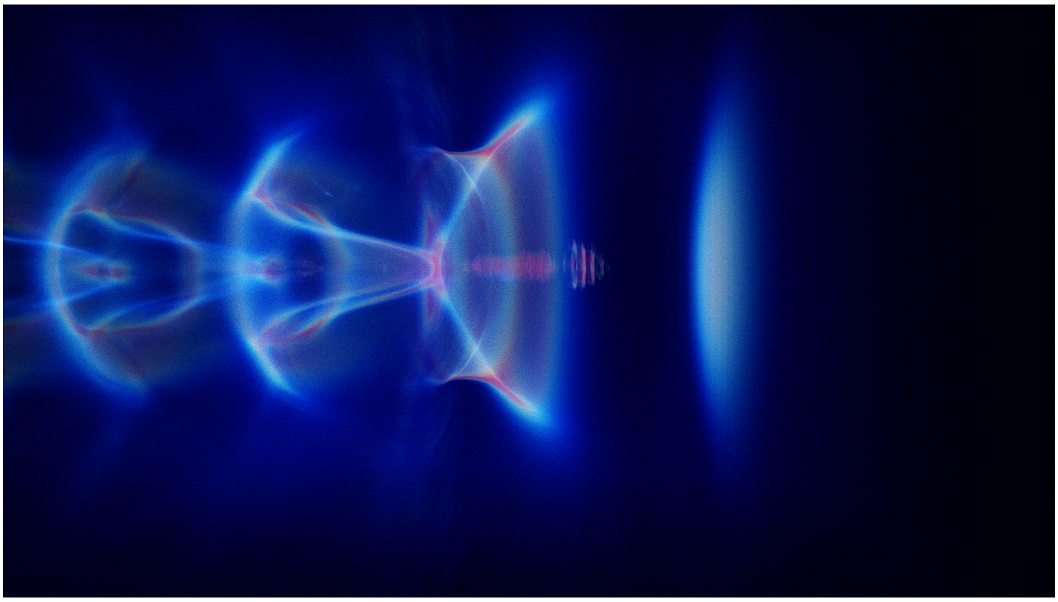

FIGURE 4.1: A 3D OSIRIS PIC simulation of LWFA in the blowout regime, rendered in parallel using Rayven. Plasma electron density is shown from low-blue to high-red, while black represents density below the background. The laser pulse (not shown) is moving to the right and is so intense that it expels all the plasma electrons from its path and creates a bubble-like feature in the plasma. This bubble feature still contains positively charged ions due to their large mass and hence has strong electric fields that pull electrons into the bubble and accelerate them as they ride along with the laser pulse. Note the imprint of the laser field can be seen at the front (right side) of the bubble, and is sitting on a density up-ramp. The imprint of the laser can also be seen as it modulates the particle bunch.

due to spectral broadening during LWFA. Simulations by Zhu et al. [136] investigated the parametric dependence of mid-IR wavelength generation from a 30fs duration intense laser pulse ($a_0 = 0.45$) traveling through under-dense plasma, finding that the efficiency of mid-IR production increased with the ponderomotive force and plateaued after complete blowout of the plasma wave was achieved. Pai et al. [85] measured mid-IR radiation with energy up to 3.5 mJ produced using a 10 TW, 45 fs laser pulse, and found that long wavelength generation was correlated with electron acceleration by LWFA in the bubble regime. Additionally, recent computational work by Nie et al. [83] has demonstrated that tunable pulses with wavelengths extending to 14 μm may be achieved using tailored density plasma targets.

4.2 Experiment

Experiments were performed by Dr. Amina Hussein as part of her Ph.D. research, her and I collaborated on this project which was supported with my simulations and theory. Experiments were conducted using the HERCULES Ti:sapphire laser system at the University of Michigan. The 30fs laser pulse was focused using an f/20 parabolic mirror to a focal spot of 10μm, achieving intensities up to $4.8 \times 10^{19} W/cm^2$ (a_0 4.7). Two types of gas cells were used to produce low-density plasma targets: a (5-20)mm variable length cell, and a (5-20)mm two-stage gas cell with a 1mm rear compartment. Plasma density was controlled by altering the pressure of the gas supply, containing 98% helium and 2% nitrogen mixed gas. Density measurements were made using a shearing Michelson interferometer, yielding maximum plasma densities up to $1.3 \times 10^{19} cm^{-3}$ in the main stage. The density in the second stage cell of 1 mm length was estimated by scaling interferometry measurements by the ratio of the volumes between the stages using the ideal gas equation. Measurements of long wavelength radiation were made using a spectrometer with a range of 900 to 2500nm. Wavelengths below 1050nm were filtered out near the entrance to the spectrometer using a 1μm long pass (LP) filter (25.4mm diameter). See figure 4.2 for a diagram of the experimental setup.

In Figure 4.3, normalized spectra are shown at varying plasma length obtained from single and two stage gas targets. The single stage was fixed at a density of 4.2×10^{18} cm^{-3}; the two stage gas cell has a density of 4.2×10^{18} cm^{-3} in the main (long) stage, while the secondary stage of 1 mm length was varied from 8.3×10^{18} cm^{-3} to 3.3×10^{19} cm^{-3}. All presented spectra are averaged from at least three shots at identical experimental conditions. The color scale shows the average spectrum over multiple shots and is consistent for all plots to demonstrate variations in signal intensity at different conditions.

In the two stage cell, greatest spectral broadening was achieved with an increase in density in the short second cell to 2.2×10^{19} cm^{-3} (Fig. 4.3b), but decreased with increasing density. The generation of longer wavelengths using a short density up-ramp at the rear of the plasma target is consistent with simulations by Nie et al. [83], where self-focusing and further self-compression of the drive pulse and rapid

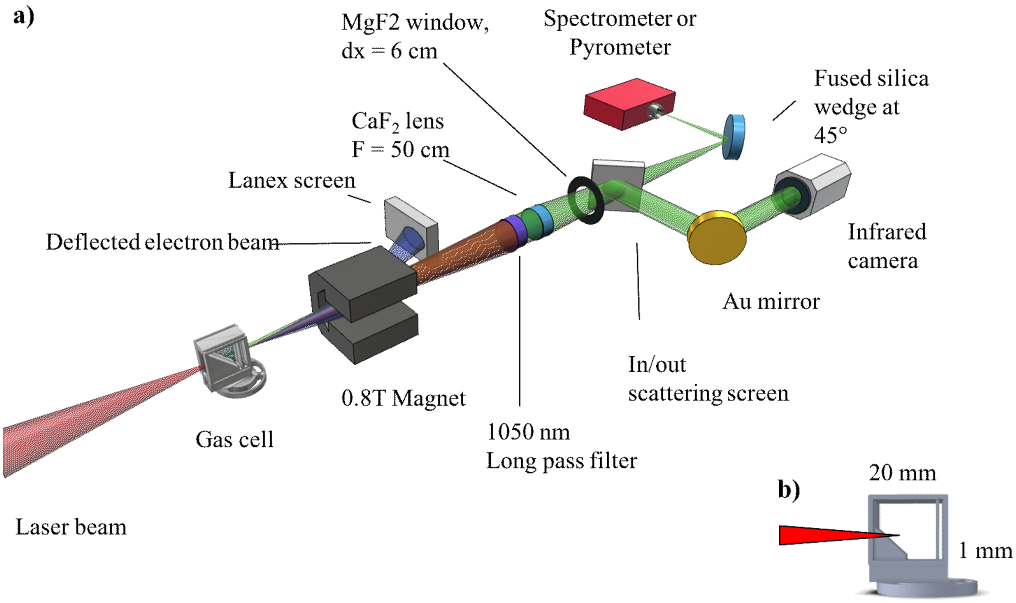

FIGURE 4.2: **a)**Experimental setup for measurement of transmitted mid-IR radiation during LWFA. A 30 fs laser pulse was focused into gas cell targets using an f/20 parabolic mirror. A 0.8 T magnet was used to disperse the electron beam onto a scintillating LANEX screen, from which the electron beam was imaged using a CCD camera. Density measurements were made using a shearing Michelson interferometer. The energy contained in long-wavelength radiation was obtained using a pyrometric detector interchanged with the NIRQuest spectrometer. Beam profile measurements from a scattering screen were obtained using a Xenics midwave thermal infrared camera. **b)** Radiation production was measured from single stage and two-stage variable length gas cells. An example of the two-stage gas cell, with a (5-20) mm variable length first stage and a 1 mm fixed length rear stage is shown in **b)**. Image courtesy of Amina Hussein.

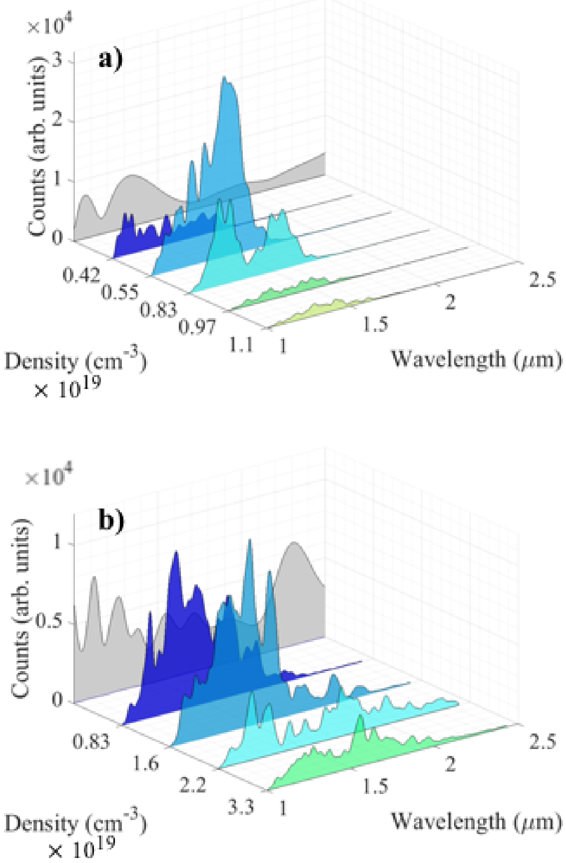

FIGURE 4.3: Spectral line-outs of the exiting mid-IR pulse from: **a)** A single-stage gas cell (L_1= 5 mm, P = 40 ± 6 TW) with varied density $n_{e,1}$, **b)** A two-stage gas cell (L_1 = 9 mm, L_2 = 1 mm, P = 50 ± 3 TW), with $n_{e,1}$ = 4.2× 10^{18} cm^{-3} and varied $n_{e,2}$. PIC spectra are shown in at the back of the plot in solid gray for a) $n_{e,1}$ = 2.0 × 10^{18} cm^{-3}, L_1 = 5 mm, and b) $n_{e,1}$ = 4.0 × 10^{18} cm^{-3}, L_1 = 5 mm, $n_{e,2}$ = 1.2 × 10^{19} cm^{-3}, L_2 = 1 mm. **c)** Mid-IR energy as a function of density in the second stage ($n_{e,2}$) for two first-stage densities ($n_{e,1}$). **d)** Mid-IR beam profile (P = 77 ± 8 TW, $n_{e,1}$ = 2.8 × 10^{18} cm^{-3}, L_1 = 6 mm, $n_{e,2}$ = 2.2 × 10^{18} cm^{-3}, L_2 = 1 mm). Image courtesy of Amina Hussein.

changes in the refractive index, producing greater broadening. Additionally, the generation of long wavelengths decreases with plasma densities above 2.2 × 10^{19} cm^{-3}. This is because the front of the laser pulse must remain in a region of negative refractive index gradient to produce long wavelengths. When the plasma density is too high in the second stage the wakefield bubble may break down, no longer containing the long wavelengths. Therefore, the reduction in signal intensity at the highest densities in Figure 4.3 is due to attenuation of the pulse due to collapse of the bubble cavity in which it is contained.

Prior to the onset of signal attenuation due to collapse of the bubble wave, spectral broadening was found to increase with plasma density due to the associated drop in the critical power for self-focusing which enhances the ponderomotive force, creating greater charge displacement and a steeper refractive index gradient. The highest average wavelength of about 1550 nm was obtained with a ratio of main stage density of approximately 4 between the main and second stages ($n_1 = 4.2 \times 10^{18}$ cm^{-3}, $n_2 = 1.7 \times 10^{19}$ cm^{-3}).

Significant enhancement of the signal intensity, particularly of wavelengths below 2 μm, was obtained with increased laser power. This is consistent with higher ponderomotive force at high power, resulting in steeper density gradients. Above a threshold power value, the conversion efficiency of laser energy to long wavelength radiation was found to plateau due to a saturation of the refractive index gradient caused by complete blow-out of the plasma wave, reducing the extent of the pulse that undergoes spectral broadening.

As shown in Figure 4.3c, mid-IR pulses with energies approaching 15 mJ were obtained using $n_e = 2.8 \times 10^{18}$ cm^{-3} in the main stage and $n_e = 1.4 \times 10^{19}$ cm^{-3} in the second stage (density ratio of 5). Variations in the output energy scale with plasma density due to the requirement of steep density gradients for optimized conversion efficiency of the driving laser pulse into mid-IR radiation. Beam profiles were measured from a scattering screen using a Xenics camera. Variations in the beam profile as a function of density in the second stage indicate that mid-IR sources with uniform spatial intensity can be created during LWFA. The intensity of the beam increased with increasing plasma density, consistent with enhanced spectral broadening and conversion efficiency due to steepening of the density gradient.

Under certain experimental conditions, radiation localized to a specific wavelength range have been obtained experimentally. Examples of these spectra are shown in Figure 4.4, where spectra with sub-100 nm variance have been produced with central wavelengths up to nearly 1.85 μm. The spectra in Figure 4.4 present all spectra with signal above the background level obtained at fixed experimental conditions. Figures 4.4 (a, b, c) all differ by more than one parameter and are subject to shot-to-shot variations, although the overall characteristics of the spectra for a given condition are consistent.

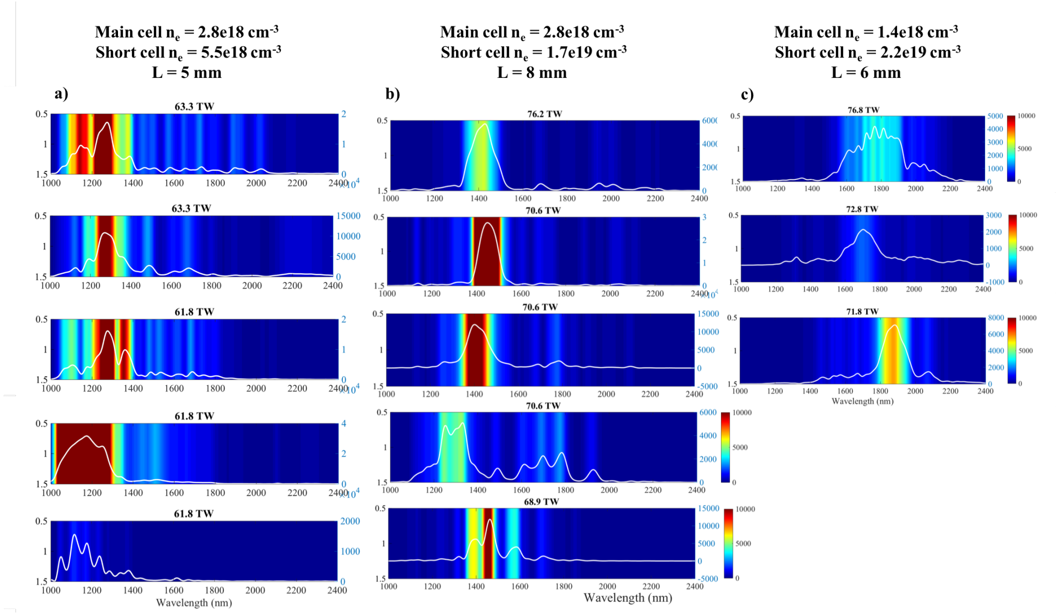

FIGURE 4.4: Multiple shots at three different experimental conditions demonstrate the production of low-divergence spectra and shot-to-shot reproducibility. Image courtesy of Amina Hussein.

In order to investigate the effect of independent parameters on spectral broadening, the Pearson correlation coefficient is applied to the covariance matrix to determine the parameters which are most highly correlated with a desired output. For the greatest production of wavelengths extending from 2 - 2.4 μm (normalized to the total signal in the pulse), plasma length and laser power were found to have the most pronounced effect, followed by the density in the second stage. The energy in the mid-IR pulse was found to be most variable with laser power and densities in the main and short cells. Optimization of mid-IR pulses from an LWFA would be best conducted using high-repetition rate laser systems, where adaptive control methods, like those applied in Ref. [56] could be applied to converge on ideal conditions.

4.3 PIC Simulations

A series of 2D and some 3D particle-in-cell (PIC) simulations were performed in a moving frame using the fully relativistic OSIRIS 4.0 code [25, 26]. The 2D simulation box size was 200 $\times$ 200 μm, with resolution 10,000 $\times$ 10,000 cells (50 cells/μm), and 20 electron particles per cell. An 800 nm, 30 fs, f/20, Gaussian laser pulse with (30 - 60) TW power was simulated. The pulse was linearly polarized in $\hat{z}$ (transverse to the simulation domain) and entered the middle of the box at $y = 0$ μm. Single and two-stage density profiles were simulated, with varying electron densities in the main stage ($n_{e,1}$, with $x_1 = 10$ mm) and second stage ($n_{e,2}$, with 1 mm length), where present. The electron temperature was initialized to $T_e = 10$ eV. An example of the general density profile is shown in figure 4.5.

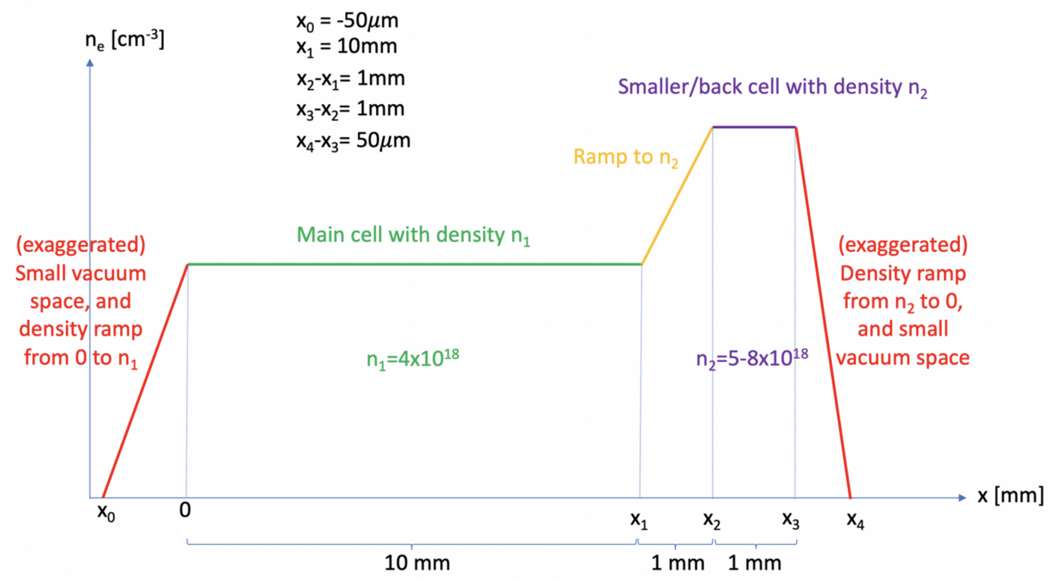

FIGURE 4.5: The general density profile involves two plasma density stages with a linear density ramp between and linear density ramps to the vacuum. Several variations of the plasma profile were simulated with electron densities in the main cell $n_e = 4 \times 10^{18} cm^{-3}$, and in the rear cell $n_e = 5 - 12 \times 10^{18} cm^{-3}$. The electron temperature was initialized to Te=10eV.

Simulation results show bursts of long wavelength (up to 50μm) light originating from the laser pulse after propagating 4.5mm into the plasma. Initially the frequency downshifting results from the density gradient at the leading edge of the laser pulse. The longer wavelength light lags behind the main pulse and passes through the non-linear wake, resulting in further red-shifting due to a forward Raman interaction with the plasma wave. The signature of forward Raman can be observed in the laser spectrum as a series of equally spaced cascades of red-shifting light (see figure 4.6 and 4.3).

As the red-shifted light lags further behind the driving pulse a portion of it interacts with an accelerated particle bunch (see figure 4.8). The result of this interaction is an upshift and scattering of the light. The longest wavelength light interacts with the plasma very strongly (n_e/n_c is large for this light) and rapidly decays inside the

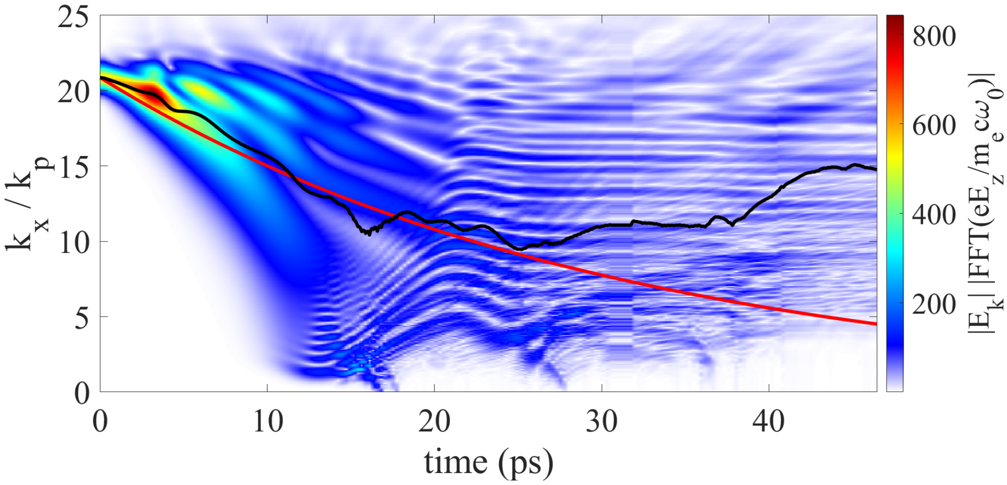

FIGURE 4.6: Laser wavenumber vs time. The initial 800nm pulse undergoes red-shifting and rapid bursting into long wavelengths at $t \approx 16ps$. The signature of forward Raman can be observed in the laser spectrum as a series of equally spaced cascades of red-shifting light.

plasma. Hence if one wants to extract the longest wavelength light, careful tailoring of the plasma density profile must be done so that the light may leave the plasma before it decays. The spectral content of the pulse after the interaction is compared for a PIC simulation and an experiment in figure 4.3. While not identical, the PIC and experimental spectrums share characteristic features that suggest some non-linear forward Raman scattering.

From the particle energy distribution (figure 4.7) one can pick out discrete bunches of accelerated particles. The bunches can be observed to accelerate until their dephasing length or when they interact with the lagging laser light. We are currently looking into whether scattered light from this interaction between the high energy particle bunch and the lagging mid-IR light may be collected and analyzed to be a diagnostic of the particle bunch.

Line-outs of the laser field E_z at $y = 0\ \mu$m were Fourier transformed to show the time history of the spectral content of the laser pulse (Fig. 4.6, note that $\lambda \propto 1/k$). As the long-wavelength light lags behind the driving pulse and passes through the wake, it is modulated on the scale of the plasma wavelength $\sim 1/k_p$ [117], as shown at $t > 10$ ps. A theoretical estimate [103] of the mean wave-number, $\langle k \rangle$, assumes red-shifting at a characteristic length scale of the pump depletion length $L_{pd} \approx 8.7k_0^2/k_p^3$, from conservation of energy and wave action, and is independent of laser amplitude

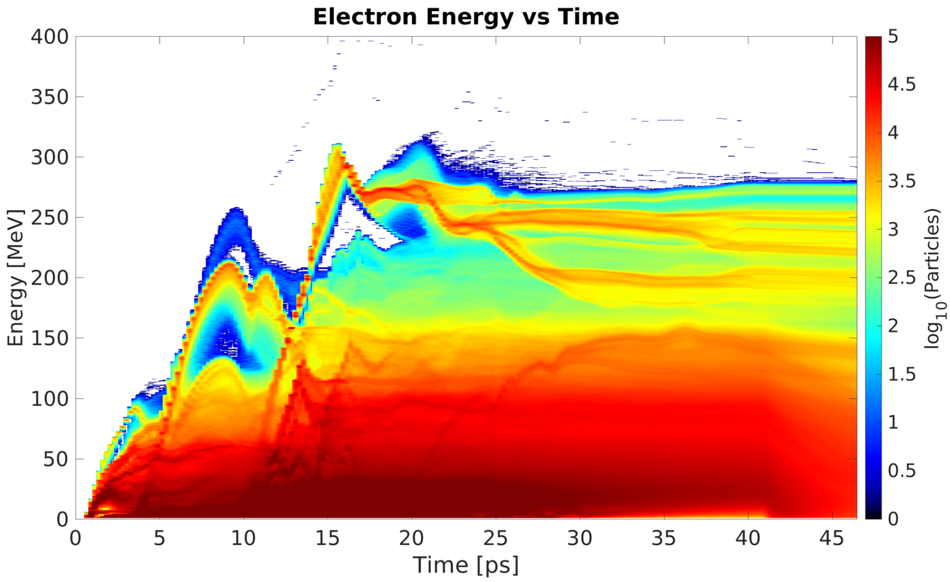

FIGURE 4.7: Electron energy vs time. From the electron energy distribution one can pick out discrete bunches of accelerated particles. The bunches can be observed to accelerate until their dephasing length or when they interact with the lagging laser light at $t \approx 16ps$.

for $a_0 \gg 1$. This can be expressed as $\langle k_{(t)} \rangle = \langle k_{(0)} \rangle e^{-ct/L_{pd}}$. The simulated and theoretical values of the mean wave-number as a function of time are plotted in Fig. 4.8c in solid black and dashed yellow lines, respectively. The theoretical curve shows good agreement with simulations during the time in which the receding light does not interact with the wake ($t < 15$ ps). However, once the receding light interacts with the the backs of the wakefield bubbles it gains spectral components associated with k_p, and the pulse undergoes blue-shifting and a reduction in intensity.

Detailed analysis of 2D PIC simulations show that the long-wavelength light generated during LWFA slips backward relative to the driving laser due to its slower group velocity (Fig. 4.8). Initially, this results in power amplification [113] as the pulse becomes compressed. However, as the receding long-wavelength pulse lags further behind, it approaches the negative density gradient corresponding to the back of the first bubble (Fig. 4.8b). Here, the swallowtail catastrophe [8] occurs due to particles emerging from the sides of the bubble as it propagates forward. Simulations reveal that the pulse is blue-shifted and side-scattered at an angle of approximately 6° from the laser axis by density perturbations of the swallowtail cone behind the first bubble (x = 4885-4880 μm). The side-scattered mid-IR light at 15.9 ps had an average wavelength of 4 μm and intensity on the order of 1% of the initial laser

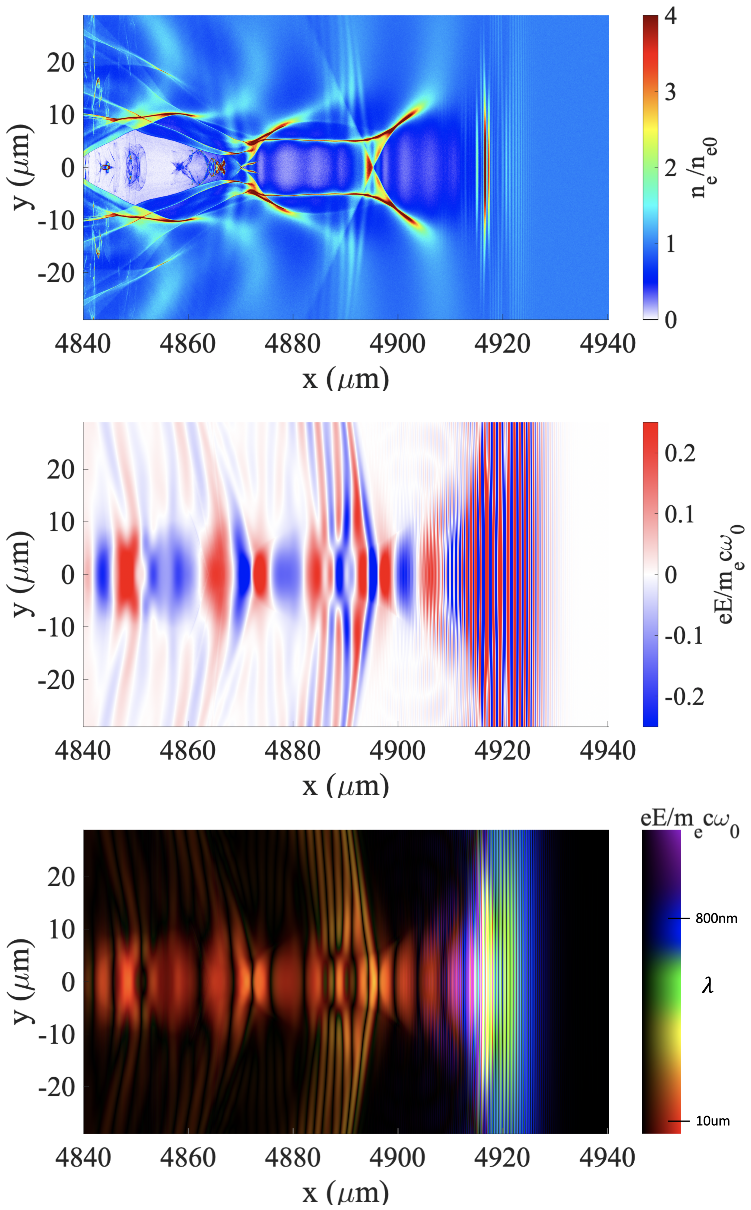

FIGURE 4.8: **a)** Plasma electron density at 15.9 ps into the interaction. The accelerated electron bunch sits at approximately 4870 μm. The colorbar is in units of n_0, i.e. the initial background electron density. **b)** The laser field E_z, shown at 15.9 ps into the interaction. The colorbar is in units of $a_0 \equiv eE/m_e c\omega_0$, the driving laser is deliberately saturated to focus on the receding light. Simulations were performed with a moving frame, where long wavelength radiation is moving backward with respect to the driving laser field. The formation of long wavelength side-scattering is observed at approximately 4800 μm. **c)** The laser field E_z, shown at 15.9 ps into the interaction. With the color indicating the color and the brightness indicating the brightness.

pulse at best-focus.

At approximately 15 ps, the interaction between the relativistic particle bunch and the slowing light may be modeled as a relativistic mirror [9]. Typically in a relativistic mirror model, the mirror and light are considered to be moving in opposite directions, such that the relativistic mirror upshifts the frequency of the light; however, in this case the light and mirror are moving in the same direction, along the direction of laser propagation. In particular, the high energy particle bunch is moving at nearly the speed of light.Laser light at the initial wavelength of 800 nm will move through plasma density of 4.00×10^{18} cm^{-3}, $n_2 = 8.0 \times 10^{18}$ cm^{-3}, at $v_g = 0.9988c$. For 10 μm wavelength light in this plasma, the velocity is reduced to $0.8c$. Therefore, the electron bunch will rapidly outrun long wavelength light. This electron bunch has a high density, exceeding the critical density ($n_e = 2.65n_c$ for 2 μm light and $n_e = 66.5n_c$ for 10 μm light) and therefore acts as a relativistic mirror, blue-shifting and scattering long-wavelength radiation. In this way, the spectrally broadened laser pulse can *decelerate* electrons. The generation of side-scattered long wavelength radiation observed in Figure 4.8b may serve as a diagnostic of bubble or electron dynamics and the detrimental interaction of the laser pulse with the accelerated electron bunch, reducing the efficiency of LWFA and maximum electron beam energy.

In general PIC simulations suggest lower plasma densities result in a slower rate of red-shifting. This is particularly relevant when the bursting into long wavelengths occurs, this process is slowed so that there is effectively more tolerance in the variation of the plasma length that would allow this light to escape. Lower plasma densities also allow for longer wavelength of light to propagate in the plasma without strong interactions or evanescence. The longer plasma wavelength (i.e. bubble size) also allows for more space between the redshifting front of the bubble and the blueshifting rear of the bubble, which may allow for more long wavelength light to escape the plasma, or may be used as a method of controlling the pulse duration.

The 2D PIC simulations systematically show a higher rate of red-shifting than observed in experiments. Since the simulations only allow diffraction of the laser in 1 spatial dimension rather than 2, the rate of diffraction may be underestimated by the simulations. Due to the lower rate of diffraction the pulse is more intense that it ought to be and therefore results in a sharper leading front density gradient. Note that this is not only true for the laser, but the plasma density perturbations themselves.

4.4 Conclusion

The generation of long-wavelength radiation extending to 2.5 μm was studied as a function of plasma density, plasma length, laser pulse and chirp, and laser power. The experimental implementation of tailored density targets using two-stage gas cells was found to enhance the production of long-wavelength radiation. Pulses with of 1 - 2.4 μm wavelength were found to contain up to 15 mJ of energy, with high quality beam profiles and the capability to ablate the surface of a copper target. Further, the sensitivity of spectral features to the co-variance of laser power, plasma density and plasma length indicate that the conditions necessary for control and tunability of a long-wavelength source from an LWFA could be achieved by utilizing high-repetition rate laser systems for adaptive control.

Supporting PIC simulations indicate that slow-moving long-wavelength radiation, which slips backward relative to the driving laser pulse, can interact the accelerated electron bunch, decreasing the energy of the electron beam and blue-shifting and scattering long-wavelength radiation. These results suggest that measurements of side-scattered long-wavelength radiation may serve as a diagnostic of electron dynamics and bunch formation.

Chapter 5

Single Shot High Bandwidth Laser Plasma Probe

5.1 Introduction

Much of the progress in laser plasma physics that has been achieved in recent years has been made possible by improvements in plasma diagnostic techniques, especially Thomson scattering (TS) [30] and proton radiography [55]. TS is the most well established plasma diagnostic [27]. It relies on calculations of the electron density correlation function and recently has been successfully applied in nonequilibrium [30], unstable [98], and shocked [94] plasmas. Proton radiography is unique in its attempt to measure electric and magnetic fields in the plasma, but it strongly relies on plasma simulations and proton trajectory calculations raising questions about the uniqueness and model dependence of the obtained results. We propose in this chapter a novel and complementary plasma diagnostic based on a pump probe interaction. While experimental validation is necessary before the practical benefits and limitations of this diagnostic can be firmly established, the possibility of controlling the interaction volume and single shot nature make it an attractive concept.

In this chapter, theory supported by laser-plasma simulations using the code pF3D [4, 112] is presented to demonstrate that a broadband probe laser can be used to recover the real and imaginary components of a plasma's refractive index in a single shot pump-probe experiment. The novelty of a single shot allows one to probe unique plasma conditions rather than being subject to shot statistics. Similarly, the bandwidth of the probe can also be a valuable tool for saving computational resources to benchmark codes in a single run.

The interaction of two or more crossing laser beams in a plasma is a widely studied topic with applications to implosion symmetry in Inertial Confinement Fusion (ICF) experiments [75], laser amplification and beam combining [43], and plasma photonics [73]. When energy is exchanged between the beams via an ion acoustic wave it is commonly referred to as Cross Beam Energy Transfer (CBET). CBET has previously been demonstrated in experiments at Lawrence Livermore National Laboratory's (LLNL's) NOVA laser [44], and more recently Turnbull et al. [121] have used LLNL's Jupiter Laser Facility to demonstrate that multiple shot pump probe CBET experiments can be used to map out the real and imaginary components of a plasma's refractive index (cf. Fig. 2 from reference [121]). Such experiments are useful in testing and validating CBET theory while the frequency dependent refractive index can provide insight into plasma conditions, although the analysis may be complicated by shot-to shot variations in the laser and plasma itself.

The pump-probe diagnostic proposed in this chapter relies on theoretical calculations of the linear plasma response to the ponderomotive force and it can be performed in a single-shot experiment under controlled conditions ensured by the presence of known pump fields. Similar to Thompson Scattering, this scheme gives information about plasma parameters and distribution functions that is localized to the pump-probe interaction length.

This chapter will first propose a method of acquiring bandwidth in the probe laser and describe the effects of this bandwidth on the laser focal spot (Sec. 5.2). Next we present kinetic modeling of the plasma response (Sec. 5.3), and describe the necessary criteria for the probe to resolve the plasma response (Sec. 5.4). Simulations of the proposed scheme are presented and compared with the kinetic model (Sec. 5.5). We then discuss how to recover plasma parameters from the refractive index (Sec. 5.6). Finally, our results are summarized and discussed (Sec. 5.7).

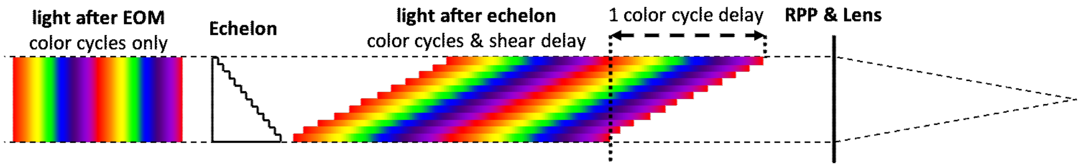

FIGURE 5.1: Schematic showing how an echelon introduces a spatially dependent delay resulting in transverse color cycling across the lens. The echelon has a slower group velocity of light causing a shear in the modulated light. Note the maximum delay is chosen to be $t_d = 2\pi/\omega_m \equiv T_m$ so that there is exactly $N_c = 1$ color cycles across the transverse direction of the pulse.

5.2 Properties of the Probe

We consider a probe beam with bandwidth introduced by an Electro Optical Modulator (EOM) that is similar to Smoothing by Spectral Dispersion (SSD)[106] on large scale laser facilities such as LLNL's National Ignition Facility (NIF) or the Omega laser at the Laboratory for Laser Energetics. The EOM is applied to the probe laser pulse during the stage of pre-amplification when the laser pulse is in a fiber. The EOM's effect is to add a sinusoidal variation in the laser's frequency as a function of time, resulting in a series of Bessel peaks in Fourier space:

$$\vec{E} = Re\left[\vec{E}_0 e^{i[\omega_0 t + \delta_m sin(\omega_m t)]}\right] \tag{5.1}$$

$$= Re\left[\vec{E}_0 \sum_{n=-\infty}^{\infty} J_n(\delta_m) e^{i(\omega_0 - n\omega_m)t}\right], \tag{5.2}$$

where $\vec{E}$ is the electric field vector with amplitude $\vec{E}_0$. The sum is taken over integer values of n, and J_n represents the Bessel function of the first kind. The resulting instantaneous laser frequency is given by $\omega(t) = \omega_0 + \delta_m \omega_m cos(\omega_m t)$, where ω_0 is the initial laser frequency, ω_m is the angular modulation frequency, and δ_m is the modulation depth.

The characteristic Bessel peaks of the bandwidth in the pulse resulting from the EOM (5.2) assume an infinite time duration of the pulse. Since ion acoustic waves require finite time to grow and saturate, the EOM alone may not provide sufficient bandwidth. A quantitative description of this is provided in Sec. 5.4 cf. Eq. (5.31). In order to overcome this limitation we employ an echelon[52, 53] cf. Fig. 5.1. The primary purpose of the echelon is to allow more of the spectral content within the color cycle to be present at the lens at the same time, so that it is all available in the focal spot simultaneously.

After passing through the EOM to introduce bandwidth, the pulse is tilted by an echelon cf. Fig. 5.1. Due to the slower group velocity and varying path length of light inside the echelon, a discrete spatially dependent delay is imposed on the pulse. The delays are optimal when exactly one color cycle is seen along the transverse y-direction of the pulse so that its full bandwidth illuminates the Random Phase Plate (RPP)[18] or Continuous Phase Plate (CPP) at all times. In the setup of Fig. 5.1, the one color cycle delay corresponds to a maximum time delay of $t_d = 2\pi/\omega_m \equiv T_m$ and is defined by the thickest step in the echelon. Since $\omega_0 \gg \omega_m$, the depth of the echelon steps can not be machined accurately relative to the laser wavelength and it introduces a random phase to the pulse on each step. These random phase imprints will cause the laser to focus to a line in the transverse direction, unless narrower random phase shifts are introduced by a smaller RPP/CPP element size.

In this chapter we make use of a RPP to control the laser spot size, shape, and intensity uniformity. In general, the phase plate is not necessary but is common to long pulse laser systems for these reasons. Without a phase plate, the focal spot will be determined by the echelon, and one may recover a smaller focal spot especially along 1 dimension (the x-dimension in our case). What is preferable will depend on the application and practical considerations.

Our choice to use an echelon as opposed to a grating typical in SSD[106] is to avoid the angular dispersion caused by gratings. Even modest amounts of bandwidth in the light incident to a grating result in rapid speckle movement and spreading of the focus cf. Fig. 5.2a. This motion and spreading results from the wavelength dependence in diffraction modes of a grating i.e. $m\lambda_1 = d\sin(\theta_m)$, where λ_1 is the probe laser wavelength, m is the mode number, d is the distance from the grating, and θ_m is the angle corresponding to the maximum of the diffracted light mode.

In the case of an echelon (Fig. 5.2b) there is little speckle movement and focal spread even at relatively large bandwidth. The broadening of the laser focal spot and individual speckles that occurs when bandwidth is applied using an echelon results from the wavelength dependent diffraction limit of the phase elements and aperture.

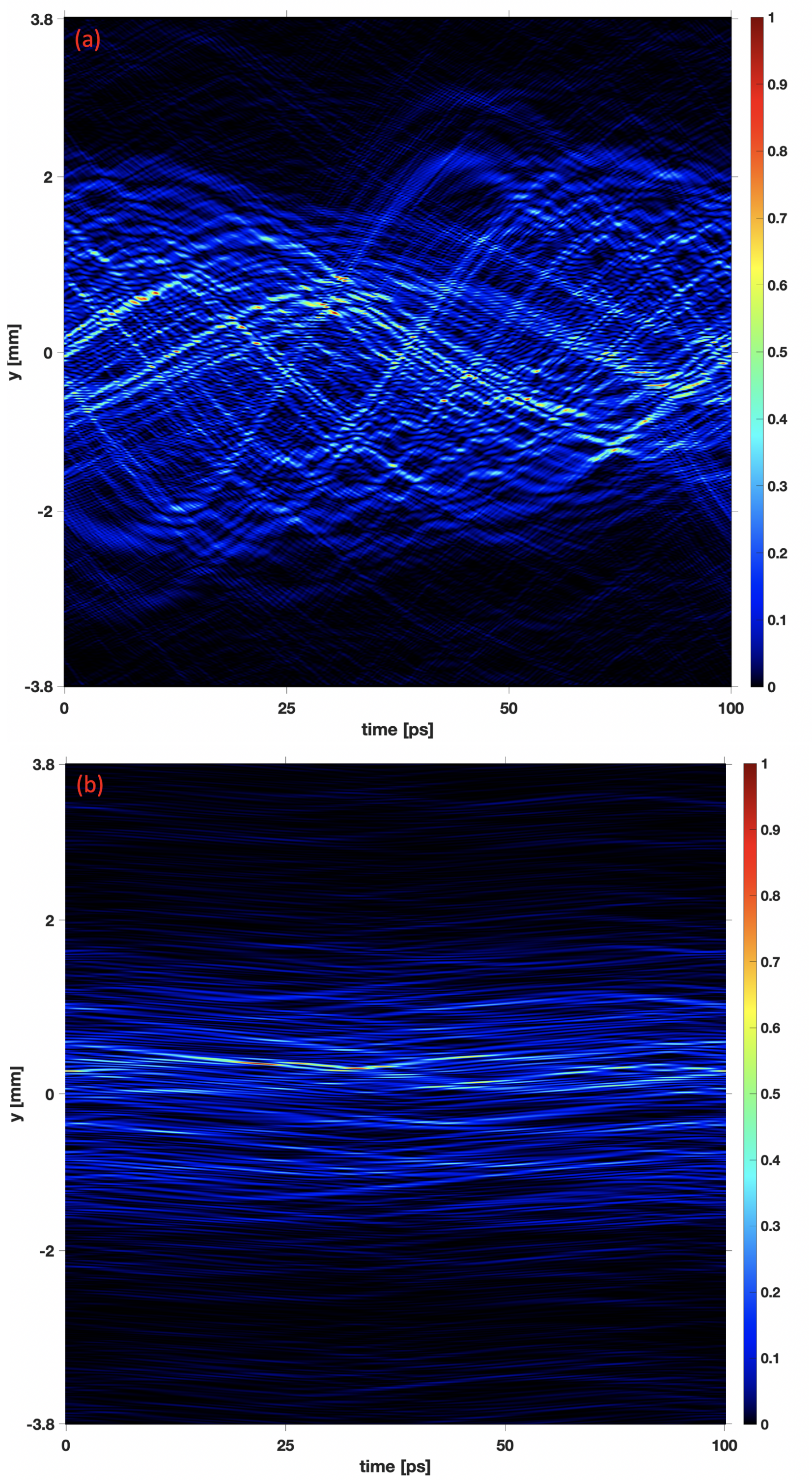

FIGURE 5.2: SSD laser spot intensity in the focal plane as a function of time (x-axis) from 0-1 [T_m] and space (y-axis). Note the sinusoidal motion of the speckles that is introduced by angular dispersion from a grating. (a) Grating with 1 color cycle ω_m=2$\pi\times$10GHz, δ_m=10, $\Delta\theta/\Delta\lambda$=1.5$\times$10^{-4}rad/ and f-number$\approx$ 20. (b) Echelon with 1 color cycle, 20 steps, ω_m=2$\pi\times$10GHz, δ_m=10, and f-number$\approx$ 20.

As seen in Fig. 5.2, at best focus the speckle width is given by $w_{speckle} = F\lambda_1/D_{Lens}$ and the focal spot size is given by $w_{spot} = F\lambda_1/D_{RPP}$, where F is the focal length of the lens, D_{Lens} is the diameter of the beam's aperture, and D_{RPP} is the diameter of the characteristic phase plate elements (see Fig. 5.5, which is described in detail later in the text). Due to the bandwidth in the probe there will be a distribution in the speckle sizes according to $w \propto F\lambda_1/D_{Lens}$.

In contrast, if a grating is used, the dominant cause of speckle and spot motion is due to angular dispersion. To achieve N_c color cycles across the pulse, the shear delay in time introduced by a grating $t_d = d_i[\Delta\theta/\Delta\lambda](\lambda_1/c)$ must equal the number of color cycles times the modulation period, i.e. $t_d = 2\pi N_c/\omega_m$, where d_i is the incident beam diameter, λ_1 corresponds to the central wavelength, and $\Delta\theta/\Delta\lambda$ is the angular dispersion of the grating. By equating these we obtain the angular dispersion associated with a grating that provides N_c color cycles $\Delta\theta/\Delta\lambda = (N_c/d_i)(\omega_1/\omega_m)$.

Modest amounts of angular dispersion are desirable for mitigating LPI and hydrodynamic instabilities in ICF [106]. However, when bandwidth is applied, angular dispersion from a grating causes different colors to focus to different locations as a function of time hence, ion acoustic waves may not be given enough time to grow and saturate to reach steady state everywhere. In the context of our simulations and proposed measurements, when high bandwidth is used angular dispersion should be minimized since it results in spreading of the focal spot and we desire a controlled interaction volume so that localized plasma parameters are observed.

The quantitative measure of these effects can be expressed in terms of the conditions for when the speckle motion (displacement) becomes comparable to the speckle size. For an echelon:

$$\frac{\Delta\lambda}{\lambda_1} > \frac{D_{RPP}}{D_{Lens}}, \tag{5.3}$$

and for a grating:

$$\frac{\Delta\lambda}{\lambda_1} > 2([\frac{\Delta\theta}{\Delta\lambda}]_{Grating} D_{Lens})^{-1}. \tag{5.4}$$

Alternatively, we can use the conditions for when the speckle motion becomes comparable to the spot size. For an echelon:

$$\frac{\Delta\lambda}{\lambda_1} > 1, \tag{5.5}$$

and for a grating:

$$\frac{\Delta\lambda}{\lambda_1} > 2([\frac{\Delta\theta}{\Delta\lambda}]_{Grating} D_{RPP})^{-1}, \tag{5.6}$$

where here $\Delta\lambda \equiv \lambda_{max} - \lambda_{min}$ is the total bandwidth in the probe and $[\frac{\Delta\theta}{\Delta\lambda}]_{Grating}$ is the angular dispersion of the grating. While speckle motion may occur with an echelon (5.3), there is little focal spot spread (5.5) compared with a grating (5.6).

Equations (5.3) and (5.5) describe for an echelon the component of speckle and spot motion resulting from the wavelength-dependent diffraction limit of the phase elements and aperture. However, there is also a sinusoidal component to the echelon's speckle motion resulting from interfering modes as seen in Fig. 5.2b. In the case of Fig. 5.2b the bandwidth is not large (relative to the central frequency) so the spot size is nearly the same as best focus, but the speckle pattern does change with speckles returning in cycles of $T_m = 2\pi/\omega_m$. These interfering modes are the beat wave pattern created by summing contributions of the electric field from different k-vectors (positions on the lens). When there is a uniform phase front incident to the lens, the modes constructively interfere resulting in a diffraction limited spot. When an RPP introduces random phase shifts a speckle pattern emerges in the focal spot due to interference of phase mismatched electric fields. When an echelon is used the changing frequency incident to the echelon steps causes this pattern to move. The speckle motion due to the bandwidth and echelon is equivalent to (and numerically modeled as) a time varying phase offset on each of the echelon steps.

5.3 Linear Plasma Response

We consider the energy transfer between two distinct electromagnetic (EM) wave modes propagating in a plasma. The waves exchange energy through their scattering on the electron density perturbations corresponding to the ion acoustic wave.

We begin with the light wave equation in a plasma:

$$(\partial_t^2 + \omega_{pe}^2 - c^2\nabla^2)\vec{a} = 0, \tag{5.7}$$

where ω_{pe} is the plasma frequency. The electric field amplitude $\vec{a}$ is decomposed into two beating EM waves:

$$\vec{a} = \frac{1}{2}\vec{a}_0 e^{i\phi_0} + \frac{1}{2}\vec{a}_1 e^{i\phi_1} + c.c, \tag{5.8}$$

where $\vec{a}_0$ and $\vec{a}_1$ correspond to the normalized electric field vectors of the pump and the probe respectively. The electric field is normalized as: $\vec{a}_\alpha = e\vec{E}_\alpha / m_e c\omega_\alpha$, where e is the elementary charge and $\phi_\alpha = \vec{k}_\alpha \cdot \vec{x} - \omega_\alpha t$ is the phase of the EM waves ($\alpha = 0, 1$). The electron density is decomposed into the background n_{e0} and fluctuation δn_e:

$$n_e = n_{e0} + \delta n_e, \tag{5.9}$$

where the density perturbation δn_e is the response to the ponderomotive force due to the two beating EM waves with phase $\phi_b \equiv \phi_0 - \phi_1$. The density perturbation is enveloped with respect to the fast varying phase ϕ_b,

$$\delta n_e = \frac{1}{2}\delta\tilde{n}_e e^{i\phi_b} + c.c. \tag{5.10}$$

The plasma frequency ω_{pe} is perturbed from its background value ω_{pe0} by the density modulation,

$$\omega_{pe}^2 = \omega_{pe0}^2(1 + \frac{\delta n_e}{n_{e0}}), \tag{5.11}$$

leading to the nonlinear coupling term in the wave equation (5.7),

$$(\partial_t^2 + \omega_{pe0}^2 - c^2\nabla^2)\vec{a} = -\omega_{pe0}^2 \vec{a}\frac{\delta n_e}{n_{e0}}. \tag{5.12}$$

To determine the density perturbation we consider the linear kinetic response given by the Vlasov equation of the electrons responding to the ponderomotive potential, ϕ_p and electrostatic potential, ϕ_{ES} due to charge separation [74]:

$$\frac{\delta n_e}{n_{e0}} = \frac{ek_b^2}{m_e\omega_{pe}^2}\chi_e(\phi_{ES} + \phi_p). \tag{5.13}$$

We consider the response of ions to the resulting charge separation only:

$$\frac{\delta n_i}{n_{i0}} = \frac{-Zek_b^2}{m_i\omega_{pi}^2}\chi_i\phi_{ES}, \tag{5.14}$$

where k_b is the beat wavenumber associated with ϕ_b, Z is the ion charge number, δn_i is the ion density perturbation, m_i is the ion mass, ω_{pi} is the ion plasma frequency, and χ_β is the species susceptibility ($\beta = e, i$). $\phi_p = -m_e c^2 |a_1||a_0|\cos(\psi_{01})/2e$ is the ponderomotive potential, for which ψ_{01} is the angle between pump and probe polarization vectors. ϕ_{ES} is the electrostatic potential obtained by solving Poisson's equation $-k_b^2\phi_{ES} = e(Z\delta n_i - \delta n_e)/\epsilon_0$ to give $\phi_{ES} = -\phi_p\chi_e/(1 + \chi_e + \chi_i)$.

We define the coefficient:

$$K \equiv \frac{\chi_e(1+\chi_i)}{1+\chi_e+\chi_i}, \tag{5.15}$$

so that the density perturbation may be expressed as:

$$\frac{\delta\tilde{n}_e}{n_e} = -\frac{k_b^2c^2}{\omega_{pe}^2}K|a_1||a_0|\cos(\psi_{01}). \tag{5.16}$$

Assuming a Maxwellian distribution function, the electron and ion susceptibilities take the form:

$$\chi_\beta = -\frac{\omega_{p\beta}^2}{2k_b^2 v_{th\beta}}\mathbb{Z}'\left(\frac{\omega_b}{\sqrt{2}k_b v_{th\beta}}\right), \tag{5.17}$$

where $\mathbb{Z}$ is the plasma dispersion function, $v_{th\beta} = \sqrt{T_\beta/m_\beta}$ is the thermal velocity and m_β and T_β are the mass and temperature of species β.

Substituting Eqs. (5.8) and (5.10) into Eq. (5.12), making the slowly varying envelope approximation ($ka \gg \partial_s a$) and collecting terms of like phase, gives the steady state results:

$$\partial_{s_1}a_1 = i\frac{k_b^2}{8k_1}|a_0|^2 a_1 K^*, \tag{5.18}$$

$$\partial_{s_0} a_0 = i\frac{k_b^2}{8k_0}|a_1|^2 a_0 K. \tag{5.19}$$

For the intensity ($\tilde{I}_\alpha \equiv |a_\alpha|^2$) one obtains:

$$\partial_{s_1} \tilde{I}_1 = \frac{k_b^2}{4k_1}\tilde{I}_0 \tilde{I}_1 K_i, \tag{5.20}$$

$$\partial_{s_0} \tilde{I}_0 = -\frac{k_b^2}{4k_0}\tilde{I}_0 \tilde{I}_1 K_i, \tag{5.21}$$

where s_0 and s_1 represent the distance along propagation of the pump and probe respectively (c.f. Fig. 5.3), and K_i denotes the imaginary component of K. Assuming the probe intensity is much less than the pump intensity so there is negligible pump depletion, we can approximate the pump intensity as a constant and solve Eq. (5.20) for the exponential growth of the probe:

$$\tilde{I}_1(L) = \tilde{I}_1(0) e^{\frac{k_b^2}{4k_1}\tilde{I}_0 K_i L}. \tag{5.22}$$

From the exponential growth we can extract a gain coefficient:

$$G = \frac{k_b^2}{4k_1}\tilde{I}_0 K_i = \ln\left[\frac{\tilde{I}_1(L)}{\tilde{I}_1(0)}\right]/L_{\mathit{eff}}, \tag{5.23}$$

where the first equality in Eq. (5.23) relates to theoretical modeling and the second equality relates to observed quantities in an experiment or simulation. The second equality in (5.23) assumes an average pump intensity $\langle \tilde{I}_0 \rangle$ over effective distance L_{eff}. In this formulation the spatial growth in the probe intensity is expressed as:

$$I_1(L) = I_1(0) e^{G L_{\mathit{eff}}}, \tag{5.24}$$

with the definition:

$$L_{\mathit{eff}} \equiv \frac{1}{\langle I_0 \rangle}\int_0^L I_0(s_1) ds_1. \tag{5.25}$$

L_{eff} is used to express the intensity weighted crossing path length seen by the probe. The definition of L_{eff} is convenient when the pump beam intensity is non-uniform along the probe's path s_1, as shown in Fig. 5.3.

Thus far, modeling of the plasma response accounts for a mono-chromatic pump

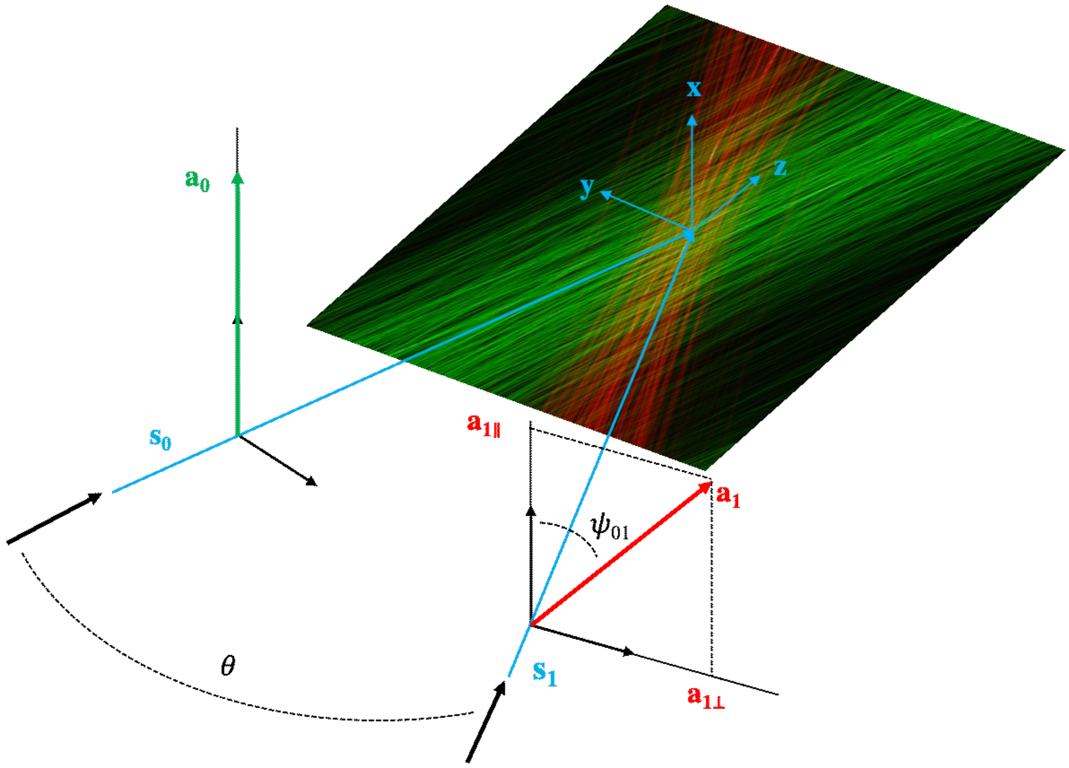

FIGURE 5.3: Schematic of beam crossing geometry and laser polarization. The probe beam (red) contains bandwidth and has much lower intensity than the monochromatic pump beam (green). The probe beam is polarized at $\psi_{01} = 45^o$ relative to the pump's polarization direction, and the beams cross at angle θ. s_0 and s_1 denote the distance along propagation directions of the pump and probe beams respectively.

and probe of variable frequency and wavenumber. If the probe intensity is sufficiently small such that the ion acoustic waves have negligible interaction with each other, we may treat our high bandwidth probe as a collection of independent probes each with a frequency and wavenumber of the Bessel peaks contained in the probe spectrum.

In the absence of a flow, longer wavelengths of the probe ($\Delta\lambda > 0$ where $\Delta\lambda \equiv \lambda_1 - \lambda_0$) will gain energy from the pump, while shorter ones (higher frequency) give energy to the pump. As in Ref. [121], the probe is polarized at 45^o relative to the pump's polarization. Only the parallel component of the probe interacts with the pump while the perpendicular component serves as a reference cf. Fig. 5.3. The power spectrum of both parallel and perpendicular components are recorded, and the ratio of the parallel to perpendicular gives the gain that is used to calculate the imaginary component of the refractive index $\eta_{i(\omega)}$, where the full complex refractive index is $\eta_{(\omega)} \equiv \eta_{r(\omega)} + i\eta_{i(\omega)}$. The spectral intensity gain is given by:

$$G(\omega) \equiv \ln\left[\frac{|E_{1\parallel}(\omega)|^2}{|E_{1\perp}(\omega)|^2}\right]/L_{\mathit{eff}}, \tag{5.26}$$

so that the imaginary component of the refractive index can be calculated via:

$$\eta_i(\omega) = -\frac{\eta_0(\omega)G}{2k_1}, \tag{5.27}$$

with:

$$\eta_0 = \sqrt{1 - \frac{n_e}{n_c}}. \tag{5.28}$$

The real component of the refractive index may be obtained using the Kramers-Kronig relations. Since the signal is analytic, causality implies the real and imaginary components are not independent, so that the real component of the signal can be calculated given the imaginary component:

$$\eta_r(\omega) = -\frac{1}{\pi}P\int_{-\infty}^{\infty}\frac{\eta_i(\omega')}{\omega' - \omega}d\omega', \tag{5.29}$$

where P denotes the Cauchy principal value. The complex refractive index can now be expressed in its usual relation to the electric field of the probe, where the imaginary component of the refractive index modifies the amplitude of the electric field and the real component modifies the phase:

$$E_{1\parallel}(L) = E_{1\parallel}(0)e^{ik_1\frac{\eta}{\eta_0}L_{\mathit{eff}}}. \tag{5.30}$$

Note that this formula assumes that η is constant over the interaction region.

5.4 Resolving Ion Acoustic Resonances

The bandwidth of the probe laser must have narrow spectral spacing and be broad enough to resolve the features of interest, primarily the ion acoustic resonances. If an EOM is used, the probe's frequency spacing is determined by the modulation frequency ω_m, cf. Eq. (5.2). The width of ion acoustic resonances is approximately the damping rate of ion acoustic perturbations, resulting in the requirement $\omega_m \ll \gamma_L$, where γ_L is the Landau damping rate of the ion acoustic wave (we assume collisional effects are negligible for simplicity). This low modulation frequency requirement places a time duration requirement. The laser must be on for at least one modulation cycle T_m to resolve the spectrum; hence low modulation frequencies are desirable for improved spectral resolution but reduce the temporal resolution by increasing the required probe pulse duration and possibly allowing temporal background plasma parameter variations to interfere with the measurement.

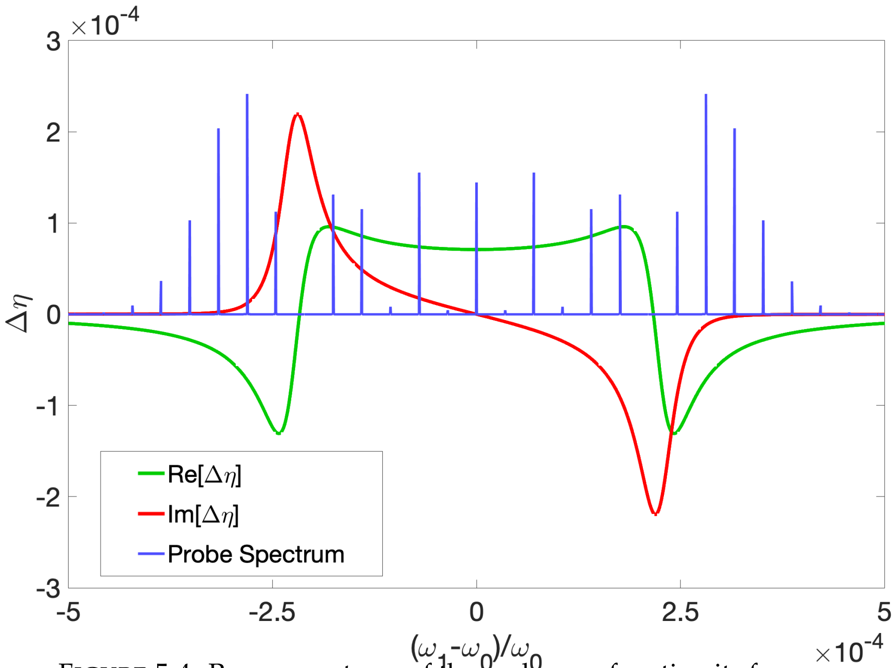

FIGURE 5.4: Power spectrum of the probe as a function its frequency ω_1 (ω_0 represents the pump), superimposed on the refractive index perturbation $\Delta\eta$ for the pF3D simulation "1" conditions. Note the probe spectral line spacing is given by the modulation frequency, and the width of the resonance peak is on the order of the damping rate. This probe spectrum is achieved by using a modulation frequency $\omega_m = 2\pi \times 10$GHz and modulation depth $\delta_m = 10$.

The total bandwidth $\sim 2\delta_m\omega_m$ given by the modulation frequency ω_m, and modulation depth δ_m, needs to be larger than the spectral range to be mapped out. To see both ion acoustic resonances, the total bandwidth must exceed $2\omega_{IAW}$, i.e. $\delta_m\omega_m > \omega_{IAW}$.

If there is a significant flow velocity in the plasma, comparable with the sound speed c_s when projected along the beat wave direction, the frequencies of resonance peaks will be shifted. To recover the spectral locations of the shifted resonance peaks, one can apply a net frequency shift in the probe (relative to the pump) or increase the modulation depth to achieve larger bandwidth within the probe.

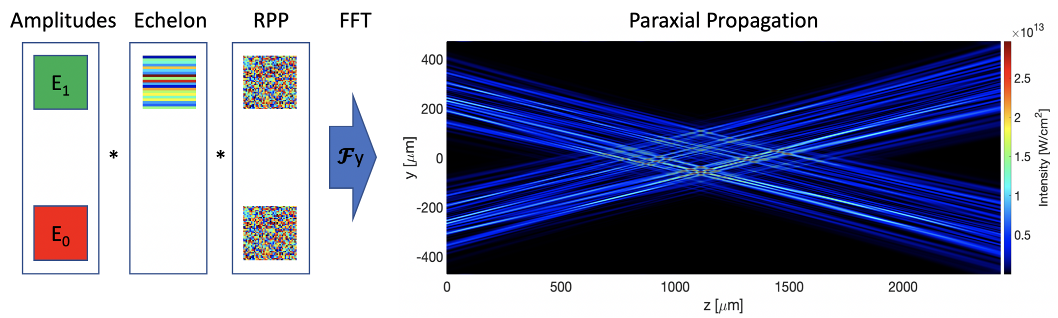

FIGURE 5.5: Initialization of the pF3D paraxial light wave starts with two separated squares (separated in k-space) in the far field (lens), with corresponding amplitudes of the pump and probe beams. The far field amplitude is then multiplied by the echelon and RPP phase masks and Fourier transformed to recover the focal spot. The focal spot is propagated backward via the paraxial approximation to the entrance plane of the simulation box. When the simulation runs the incoming light is propagated forward with the paraxial approximation now including the interaction with the plasma. Note the width of the amplitude squares corresponds to D_{Lens}, the width of the echelon elements corresponds to $D_{Echelon}$, and the width of the RPP elements corresponds to D_{RPP}.

Since ion acoustic waves must be given enough time to grow and saturate, short pulses (normally associated with high bandwidth) cannot be used. The bandwidth must be sustained so that individual ion acoustic wave modes saturate. This requires a slow change in frequency relative to the width of the resonance, during the saturation time t_s from [72] such that:

$$t_s \left[\frac{d\omega}{dt}\right]_{max} \ll \gamma_L, \tag{5.31}$$

where the saturation time[72] is:

$$t_s = 2\frac{\gamma^2}{\gamma_L^2}\frac{s_1}{c}, \tag{5.32}$$

Here, $\gamma^2 \equiv \omega_{pe}^2\omega_b c^2 m_e|a_0|^2/(4\omega_1 m_i c_s^2)$ is the temporal growth rate of the forward Brillouin scattering in the interaction of two crossing laser pulses [72]. Applying this to the instantaneous laser frequency resulting from an EOM gives the slow change in frequency requirement:

$$\delta_m \omega_m^2 t_s \ll \gamma_L, \tag{5.33}$$

In the absence of an echelon or grating (no pulse front tilt), an EOM could be used on its own if it satisfies these conditions. However, the pulse front tilt allows the full bandwidth to be seen at any given time and therefore reduces the slowly varying frequency requirement (5.31) by a factor related to the number of echelon steps. In principle, any method of generating bandwidth that satisfies the criteria (slow change in frequency, broad enough to see resonances, etc.) can be used to recover the gain curve. However, the equally-spaced frequency comb provided by the EOM is common, convenient, and easily characterized.

Since this scheme is dependent on a spectrum of laser beat waves, it is sensitive to the lasers' f-numbers. A finite f-number implies focusing of the laser light over a range of angles (k-vectors). Since each laser contains a range in k-vectors, the beat wave created by the lasers will not be a single k-vector. The spectrum of beat k-vectors is given by the convolution of the distribution of the two crossing laser's wavenumbers. If light incident to the optics is approximately evenly distributed over the square/circular surface, the resulting convolution of k's is a triangular/pyramid (2D/3D) distribution in beat waves. The plasma response is then convolved (blurred) with the spread in k's associated with the beat wave (ion acoustic wave) resulting in the apparent broadening of narrow resonances. This effect is taken into account when determining the plasma response, c.f. Fig. 5.7. In this scheme a higher f-number is generally preferred because it reduces the blurring due to additional beat waves and increases speckle size to allow for more slowly varying envelopes.

The probe laser contains both bandwidth from the EOM and a sweep in k-vectors due to the focusing optics. Hence the probe may beat with itself to satisfy an IAW resonance and transfer energy from its own high frequency components to its own low frequency components. While smaller f-number optics provide a larger spread in perpendicular k-vectors, the larger k-vectors contribution is canceled by their shorter interaction length. So, on average, the self-gain of two resonant spectral lines is given by:

$$GL_{eff} = \frac{n_e}{n_c}\frac{W}{2\delta_m}\frac{Ie^2}{c^3\epsilon_0 m_e m_i c_s \gamma_L}, \tag{5.34}$$

where W is the width of the laser at best focus and ϵ_0 is the permittivity of free space.

The self interaction of the probe scales with its intensity, and can be considered negligible if the the intensity is sufficiently low such that $GL_{eff} \ll 1$.

5.5 Simulations of the Plasma Response

The theoretical framework of the plasma response in Sec. 5.3 and the crossing laser pulse propagations are formulated using kinetic theory (5.13), (5.14), (5.15), and electromagnetic wave equations (5.7), respectively. These are standard elements of the large scale wave interaction codes such as pF3D [6], Harmony [35] or LPSE [80] that are effective numerical tools used in the description of crossed beam energy transfer and laser plasma coupling. Their ability to model large scale laser plasma interactions follows from the hydrodynamical description of the plasma and waves with an accurate account of Landau damping and mode frequencies by means of nonlocal and nonstationary coefficients in the fluid like equations. Our results will demonstrate the accuracy of these models in reproducing the linear plasma response for ion acoustic modes in equilibrium plasmas and the proposed pump-probe experiments could be used in generalizing such descriptions to plasmas away from equilibrium or affected by strong magnetic fields.

An important advantage of laser plasma interaction codes is in the paraxial modeling of electromagnetic wave propagation with all complexities of random phases and optical elements of the proposed experimental set-ups, cf. Fig. 5.5. In this chapter we have used pF3D's hydrodynamic plasma response to self-consistently couple the EM waves to the plasma. In this configuration, the pump and probe are modeled with one enveloped paraxial field containing both lasers (Fig. 5.5). The field is coupled to a quasi-neutral hydrodynamic model of the plasma with coefficients such as damping and equation of state evaluated using kinetic theory. The light wave is governed by[6]:

$$\left(\partial_t + v_g\partial_z - \frac{ic^2 k_0 \nabla_\perp^2}{\omega_0\left(k_0+\sqrt{k_0^2+\nabla_\perp^2}\right)} + \gamma_0 + i\dot{\phi} + \tfrac{1}{2}v_g'\right)\vec{a}$$

$$= -\frac{i}{2\omega_0}\frac{4\pi e^2}{m_e}\delta n_e \vec{a}, \tag{5.35}$$

where $v_g = c^2 k_0/\omega_0$ is the light wave group velocity in the z-direction, v_g' is the z-derivative of the group velocity, γ_0 represents losses in the light wave due to effects such as inverse bremsstrahlung, $k_0 = (\omega_0/c)\sqrt{1 - \overline{n}_{e(z,t)}/n_c}$ is the local z-dependent wavenumber, $\overline{n}_{e(z,t)}$ is the intensity weighted plasma density seen by the lasers at each z-location, $\phi = \int_0^z k_0(z', t)dz'$ is the local phase, $\dot{\phi} \equiv \partial\phi/\partial t$, and δn_e is the perturbation in the fluid electron number density. The plasma fluid response is governed by conservation of mass:

$$\partial_t \rho + \vec{\nabla} \cdot (\rho \vec{v}) = 0, \tag{5.36}$$

conservation of momentum:

$$\partial_t(\rho \vec{v}) + \vec{\nabla} \cdot (\rho \vec{v} \vec{v}) + \vec{\nabla} p = \vec{p}_f + \vec{d}, \tag{5.37}$$

and conservation of energy:

$$\partial_t \mathcal{E} + \vec{\nabla} \cdot [(\mathcal{E} + p)\vec{v}] = \vec{v} \cdot (\vec{p}_f + \vec{d}) + d_e - \vec{\nabla} \cdot \vec{q}_e, \tag{5.38}$$

Here, ρ is the total (approximated as just the ions) mass density, and $\vec{v}$ is the fluid velocity so that the momentum density is $\rho\vec{v}$. $\vec{q}_e = -\kappa_{SH} \vec{\nabla} T_e$ where κ_{SH} is the Spitzer-Härm heat conductivity, and $p = n_e T_e + n_i T_i$ is the total pressure. The light's effect on the density is through the ponderomotive force given by $\vec{p}_f = -e^2 \vec{\nabla}(E^2)/(4 m_e \omega_0^2)$, and $\vec{d} = -\gamma_L \rho \vec{v}$ describes the Landau damping of the fluid momentum, while d_e is the dissipated energy per unit volume per unit time due to Landau damping of ion-acoustic waves.

The energy of the fluid is expressed as:

$$\mathcal{E} = \frac{1}{\gamma - 1} p + \frac{1}{2} \rho |v|^2, \tag{5.39}$$

where $\gamma = C_p/C_v$ is the ratio of specific heats, and takes the value of 3 for a collisionless 1D adiabatic fluid. The rapid electron heat conduction $\vec{q}_e$ modifies the wave dispersion relation so that $\gamma_e = 1$ and $\gamma_i = 3$ in the sound speed expression $c_s = \sqrt{(\gamma_e Z T_e + \gamma_i T_i)/m_i}$.

Two pF3D simulations, case “1" and case “2", are highlighted in this section. The purpose of case “1" is to validate that the high bandwidth probe recovers the same plasma response as probing with a series of monochromatic probes. The purpose of case “2" is to demonstrate agreement between simulation and theory while using moderate f-number RPP beams relevant to long-pulse ICF facilities. Both simulations are performed in 2D in the y-z plane, where z is the paraxial propagation direction, cf. Fig. 5.3. Bandwidth is added to the probe beam which is polarized $\psi_{01} = 45^o$ ($\hat{x}\hat{y}$) relative to the pump ($\hat{x}$). The probe then passes through a simulated 20-step echelon to achieve shear delays resulting in $N_c = 1$ transverse color cycles. The echelon's random phase imprint is included in the simulations, but is masked out when the probe passes through a RPP. Simulations were run for several modulation periods to allow for growth and saturation of the ion acoustic waves, and to spectrally resolve the modulation frequency. Both simulations are performed in a fully ionized He^{2+} plasma with electron temperature $T_e = 220eV$. The pump wavelength is λ_0=1.053μm, and the beams are set to cross at an angle of θ=27^o. Fourier transforms were taken over an integer number of modulation periods $T_m = \frac{2\pi}{\omega_m}$=100ps and 400ps (“1" and “2") so that the Bessel peaks are aligned with the frequency resolution.

The first simulation (“1") uses $T_e/T_i = 2$ and the probe is given bandwidth by a simulated EOM with modulation frequency ω_m=2$\pi\times$10GHz, and modulation depth δ_m=10, giving a total bandwidth of approximately 200GHz or 8Å centered about the pump wavelength λ_0=1.053μm. Both the pump and probe had Gaussian envelopes with focusing optics f-number 100 and 33 respectively. The peak pump intensity is $3.6 \times 10^{12}\mathrm{W/cm^2}$ and the peak probe intensity is $3.4 \times 10^{10}\mathrm{W/cm^2}$. The ion acoustic damping rate for this simulation is $\gamma_L = 0.151\omega_b$ at resonance. Figure (5.6) shows the results of the pF3D simulation “1" using a series of mono-chromatic probes (blue) as in Ref. [121], and a single high bandwidth probe (red). The high bandwidth probe reference ($\hat{y}$) spectrum is shown in yellow. The single shot high bandwidth probe shows very good agreement with monochromatic probing in pF3D simulations.

The second simulation (“2") uses $T_e/T_i = 3$, an EOM with modulation frequency ω_m=2$\pi\times$2.5GHz, and modulation depth δ_m=40, again giving a total bandwidth of approximately 200GHz or 8Å centered about the pump wavelength λ_0=1.053μm.

Both the pump and probe have f-number = 9 focusing optics and a sinc^2 focal spot intensity due to the square aperture. The peak pump intensity is 5×10^{12}W/cm^2 with speckles reaching intensities of 3×10^{13}W/cm^2, giving $\langle I_0 \rangle L_{eff} = 2 \times 10^{11}$W/cm. The peak probe intensity is 5×10^{9}W/cm^2. The ion acoustic damping rate for this simulation is $\gamma_L = 0.078\omega_b$ at resonance. The results of case "2" are compared with theory (Eq. (5.23)) in figures 5.7 and 5.8, and the effects of the finite f-numbers are taken into account by weighting the plasma response with an equal amplitude spread in k-vectors derived from the f-number of the lasers. A fluid theory from Ref. [71] is also plotted in Fig. 5.7 showing slightly better agreement with the shape and location of the resonance peaks when using $\gamma_e = 1$, $\gamma_i = 3$, in the sound speed expression.

In both simulations the pump and probe both are of a sufficiently low intensity such that the ion acoustic waves are expected to be linear. The pump intensity is sufficiently large compared with the probe ($I_0 \gg I_1$) and the gain is kept low so that there is negligible pump depletion and the pump is assumed to be constant intensity.

A line-out of the pump's intensity profile along the trajectory of the probe (path s_1 in Fig. 5.3) is used to calculate theoretical gain. While the RPP causes fluctuations in the intensity along this path, the integral over the intensity profile is approximately consistent within the transverse profile of the probe beam (here, the crossing region is small compared with the focal length of the lasers and high intensity speckles do not cause non-linearities). As in Eqs. (5.22) and (5.23) we can express the gain in terms of an effective distance over which the probe sees the pump's average intensity (5.24) (5.25).

The symmetric Lorentzian-like fluid response shown in Fig. (5.7) deviates slightly from kinetic theory, particularly near $\Delta\lambda = 0$. Since pF3D utilizes a fluid-like plasma model, it is expected to agree with the fluid theory. The slight deviation near the peaks may be attributed to effects such as deviation from the paraxial approximation or numerical dispersion. There is a discontinuity in the imaginary component of the response at $\Delta\lambda = \pm 4$, which is where the amplitude in the spectral lines is diminished to noise level and we have simply substituted zeros. This discontinuity manifests in the real component of the response as a small bump, but can be considered negligible if the probe's bandwidth is large enough to map out the plasma

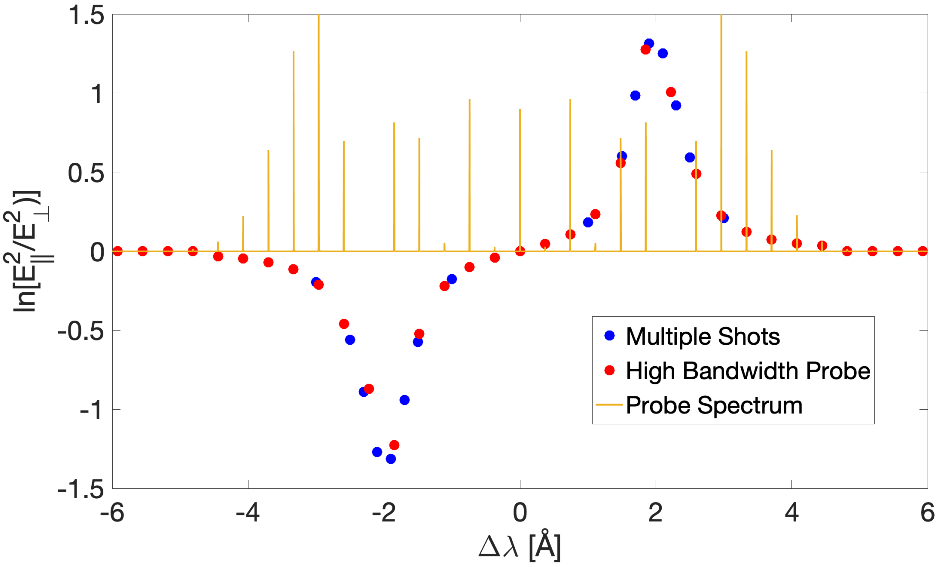

FIGURE 5.6: Simulation case "1" results using a series of monochromatic probes (blue) and a single high bandwidth probe (red). The high bandwidth probe reference spectrum is shown in yellow.

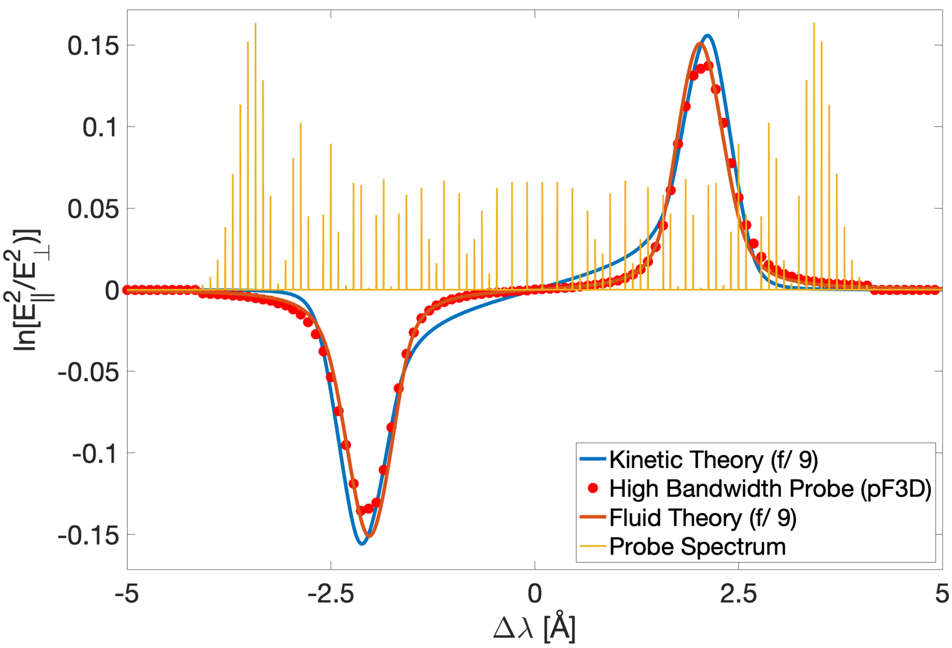

FIGURE 5.7: pF3D simulation case "2" results of the imaginary component of the refractive index compared with theoretical results when the effects of the pump and probe's finite f-number is taken into account.

response.

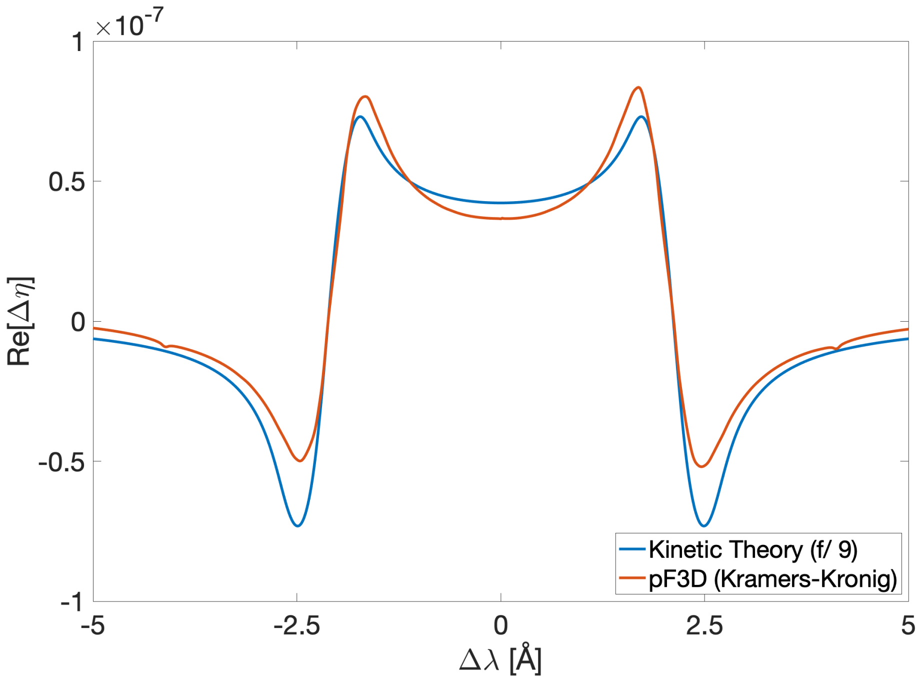

FIGURE 5.8: Real component of the refractive index obtained by using the Kramers-Kronig relations on pF3D simulation case “2" results compared with theoretical results when the effects of the pump and probe’s finite f-number is taken into account.

5.6 Diagnosing the Plasma

In our simulations, the high bandwidth probe has been shown to recover the entire wavelength dependent CBET gain in a single shot. The CBET gain is related to the imaginary component of the plasma’s refractive index and can also be used to recover the real component via the Kramers-Kronig relations. Both the real and imaginary components of the plasma’s refractive index are useful quantities for studying light propagation in a plasma and characterizing plasma photonics components. The real and imaginary components of the refractive index depend directly on the particle distribution function, and could provide insight on non-Maxwellian distribution functions. Below, we demonstrate how several plasma parameters can be recovered in a case where the distributions are Maxwellian.

The frequency spacing between the two ion acoustic resonance peaks is equal to twice the the ion acoustic frequency, while the ion acoustic wavenumber is known from the crossing angle and laser wavelengths [$\vec{k}_b = \vec{k}_0 - \vec{k}_1, k_b \approx 2k_0 \sin(\theta/2)$] so that the sound speed can be calculated:

$$c_s = \frac{\omega_b}{k_b} = \sqrt{\frac{ZT_e + 3T_i}{m_i}}. \tag{5.40}$$

Assuming $ZT_e \gg 3T_i$ and Z and m_i are known, T_e is approximately obtained using:

$$c_s \approx \sqrt{\frac{ZT_e}{m_i}}, \tag{5.41}$$

$$T_e \approx \frac{m_i c_s^2}{Z}. \tag{5.42}$$

The real and imaginary components of the refractive index depend on the coefficient:

$$K \equiv \frac{\chi_e(1+\chi_i)}{1+\chi_e+\chi_i}. \tag{5.43}$$

Taylor expanding the real component of K about $\Delta\lambda = 0$ (i.e. $\omega_b/k_b \equiv v_{ph} = 0$) and assuming $ZT_e \gg 3T_i$ gives the relation:

$$K_{r(\Delta\lambda=0)} \approx -\frac{1}{k_b^2\lambda_{De}^2} = -\frac{1}{k_b^2}\frac{n_e e^2}{\epsilon_0 T_e}, \tag{5.44}$$

and doing the same for the derivative of the imaginary component:

$$K'_{i(\Delta\lambda=0)} \approx -\sqrt{\pi}\frac{T_i}{ZT_e}\frac{1}{k_b^2\lambda_{De}^2} \approx \sqrt{\pi}\frac{T_i}{ZT_e}K_{r(\Delta\lambda=0)}, \tag{5.45}$$

so that if one knows the plasma's electron temperature, one can obtain the electron density from Eq. (5.44) and the ion temperature from Eq. (5.45).

One can detect a flow velocity using the offset of the mean of the resonances from zero. The component of a flow velocity that is parallel to the ion acoustic wave will doppler shift the ion acoustic frequency such that the resonance conditions become:

$$\vec{k}_0 = \vec{k}_1 + \vec{k}_b, \tag{5.46}$$

$$\omega_0 = \omega_1 + \omega_b + \vec{k}_b \cdot \vec{V}_{flow}, \tag{5.47}$$

where $\vec{V}_{flow}$ is the flow velocity. The net effect is to shift the ion acoustic resonances by $\vec{k}_b \cdot \vec{V}_{flow}$, so that the parallel component of the flow velocity can be detected in the refractive index.

While valid, the approximations made above are not always optimal for use in recovering plasma parameters. The expressions are presented in this chapter to show a dependence on the parameters, but in the case of an experiment one should match the refractive index using a kinetic forward model such as Eq. (5.23).

Figures 5.9 and 5.10 show the sensitivity of the refractive index to variations in the parameters n_e, T_e, and T_i of a kinetic forward model compared with the reference conditions of case “2" including the f-number = 9 optics on the pump and probe. As seen in Fig. 5.9 and described by Eqs. (5.40) and (5.45), the ion acoustic resonance frequency is approximately independent of electron density, but it depends strongly on the electron temperature and also on the ion temperature. The slope of the imaginary response at $\Delta\lambda = 0$ depends most strongly on the electron temperature, but is affected by both the ion temperature and electron density. The full width half maximum of the resonances is approximately $2\times$ the ion acoustic damping rate, which depends primarily on ZT_e/T_i for Landau damping. As seen in Fig. 5.10 and described by Eq. 5.44, the real component of the refractive index at $\Delta\lambda = 0$ is sensitive to n_e and T_e while T_i has only a small effect.

For simplicity, we effectively average over the short (speckle-scale) inhomogeneities, which is valid when the system size is significantly larger than a speckle. We also assume in our present analysis that there are no long (larger than speckles) scale gradients. Such assumptions are not requirements, and an inhomogeneous density or temperature profile could certainly be used when attempting to fit a calculated gain to the measured gain by varying plasma parameters.

5.7 Conclusions

In this chapter we have proposed a pump-probe experiment and described the theoretical analysis. To apply this probe in an experiment one must first model the interaction of two crossing beams to ensure that CBET remains in the linear regime without pump depletion and to ensure that ion acoustic resonances will be observed with the available bandwidth. With a theoretical model, one can determine acceptable pump and probe intensities and their crossing angle. Suitable bandwidth is

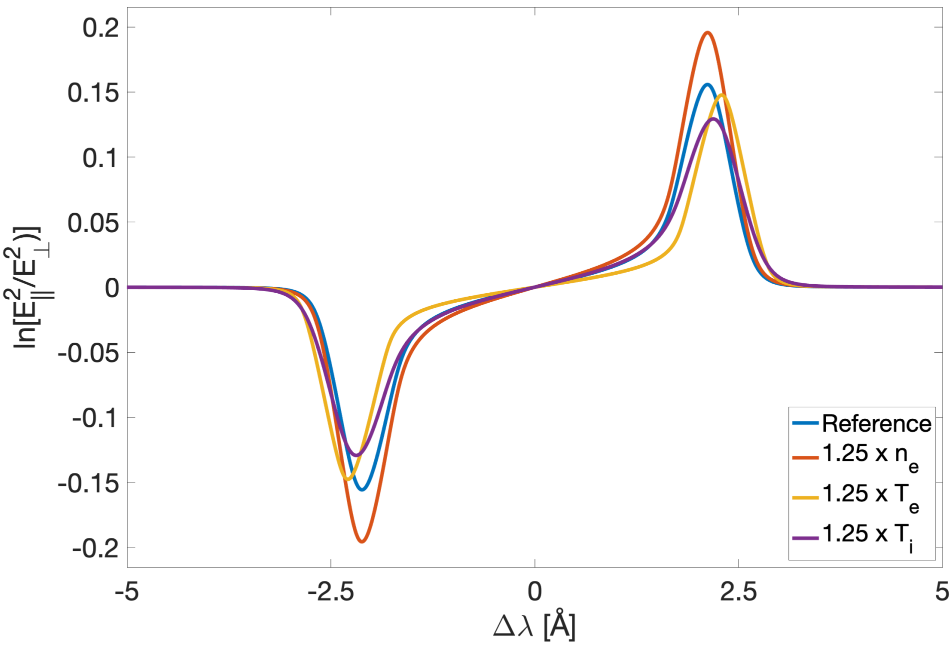

FIGURE 5.9: Variations in the imaginary component of the refractive index for a 1.25× perturbation in n_e (red), T_e (yellow), and T_i (purple). The reference curve (blue) corresponds to the parameters of case "2".

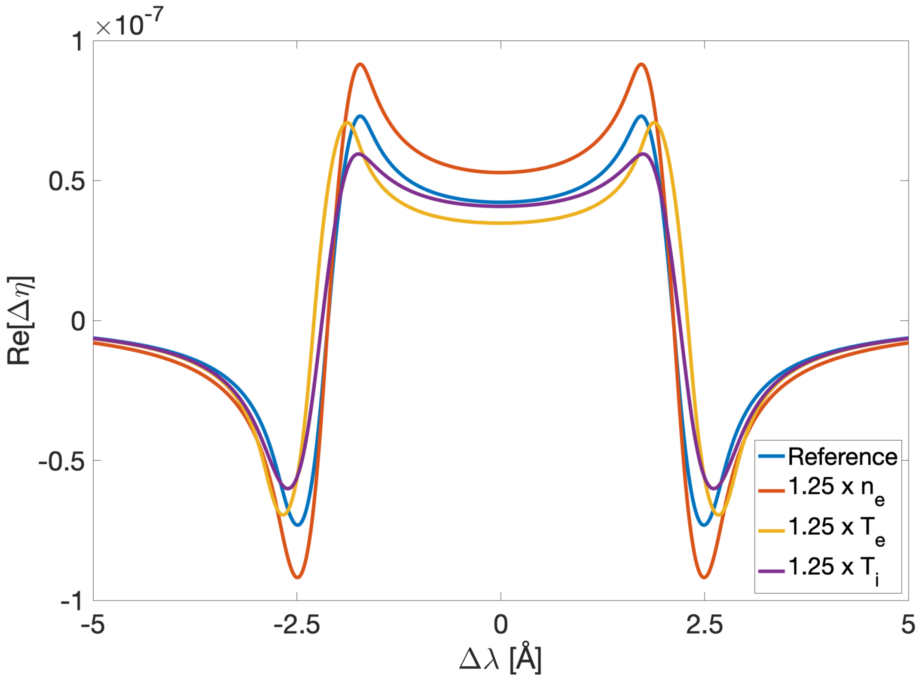

FIGURE 5.10: Variations in the real component of the refractive index for a 1.25× perturbation in n_e (red), T_e (yellow), and T_i (purple). The reference curve (blue) corresponds to the parameters of case "2".

applied to the probe beam using an EOM and echelon. The probe beam is polarized at an angle to the pump so that there is sufficient intensity in the perpendicular and parallel components. Perpendicular polarization results in no energy transfer and serves as the control result for the measurement of spectra of the transmitted probe. The pump and probe beams are crossed so that the overlap volume examines the plasma of interest and the beams remain on for at least one modulation period. The ratio between the spectra of parallel polarized probe that couples to the pump and the reference spectra of perpendicularly polarized probe is used to determine the experimental gain and refractive index. A theoretical model is applied to fit the experimental refractive index in order to determine plasma parameters. The proposed pump-probe experiment has been modeled in this chapter using wave interaction code pF3D.

In summary, we have shown the possibility of recovering a plasma's complex index of refraction with a single shot high-bandwidth pump-probe experiment. We have motivated the use of an echelon for avoiding angular dispersion when high bandwidth is used, and described the necessary properties of the bandwidth required to recover the refractive index. The wavelength-dependent refractive index is directly related to the particle distribution function and can be used to recover plasma parameters including electron and ion temperatures, electron density, and plasma flow velocity. A high bandwidth probe has been demonstrated to be consistent with individual monochromatic probe shots in pF3D simulations (Fig. 5.6) and can additionally be used as an efficient method of benchmarking codes in a single run.

Chapter 6

Bow Shock Formation in a Flowing Plasma with Crossed Laser Beams

6.1 Introduction

Inertial Confinement Fusion (ICF) faces challenges with implosion symmetry, energy coupling and efficacy. Implosion symmetry is known to be strongly affected by Cross Beam Energy Transfer (CBET). If plasma conditions where the lasers cross are known, one can use theory to determine a wavelength shift between inner and outer laser beams to help counteract unwanted CBET induced from plasma flows [75]. As shown in the previous chapter, even when lasers of the same frequency are crossed in a flowing plasma, cross beam energy transfer can still occur. The energy transfer occurs because the ion acoustic wave in a flowing plasma is doppler shifted and in sonic flows ($M \equiv v_{flow}/c_s = 1$) resonance is achieved [11]. In this chapter we discuss some additional effects that occur when lasers propagate in a flowing plasma. The additional effects include shock formation and beam redirection which has recently been studied in this geometry [34, 36]. These effects may alter plasma conditions and beam propagation resulting in changes to the predicted CBET.

While CBET theory has been shown to make accurate predictions in stationary plasmas, the effects of laser speckles are typically neglected when considering flowing plasmas. A lasers speckles ponderomotive force can dig channels in the plasma density which result in a lower index of refraction and act to guide the light along the channels. In a flowing plasma the laser speckle channels will move with the plasma re-directing the laser light along the flow. Since the laser light contains momentum, by conservation of momentum, the speckles exert a ponderomotive drag force on the plasma. We present theory and simulations to show that flowing plasmas may result in additional effects such as deflection and spraying of the beams [60], and shock formation. Figures 6.1a,b compare a pF3D simulation at 10ps (a) and 200ps (b) to demonstrates some effects of a sonic flow on crossing lasers. Figure 1a displays what is typically predicted from CBET theory, and Fig. 1b shows the additional effects of beam bending/spraying.

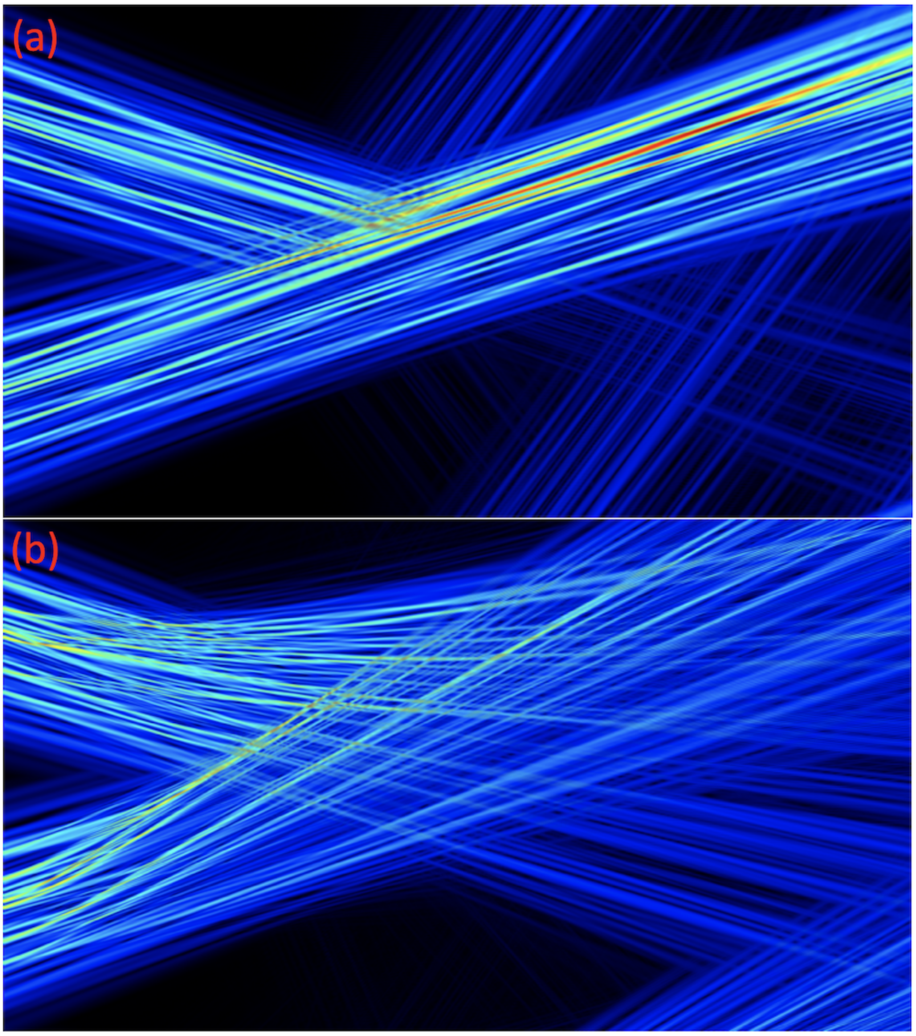

FIGURE 6.1: Crossing lasers intensity in a Mach 1.1 flow at (a) t=10ps. (b) t=200ps. The flow is in the upward direction, while the lasers are traveling to the right. The simulation was run using pF3D. The color bar is normalized to the maximum intensity displayed and the simulation used periodic boundaries along the y-direction.

This chapter will examine physics of the response of flowing plasma to laser beams smoothed with random phase plates. Previously, as verified by theory and simulations, it has been shown that plasma flow with velocity component, $\vec{v}_\perp$, transverse to the direction of laser beam propagation results in laser beam deflection [34]. A flowing plasma skews the density perturbation produced by the ponderomotive force of the laser in the direction of $\vec{v}_\perp$ and this results in a redirection of the laser light propagation. The resulting beam bending and the amplitude of density perturbation are strongly enhanced in the vicinity of the sonic layer, where $v_p = c_s$, i.e. for $M = v_p/c_s = 1$, where the sound velocity is $c_s = (ZT_e/m_i)^{1/2}$ and M is the Mach number.

The physical processes associated with these interactions are illustrated in Fig. 6.2. This plot shows the density perturbation seen at 2ns in pF3D simulations of the plasma flow across a quad of NIF beams at the average plasma conditions corresponding to $\sqrt{\langle v_{osc}^2 \rangle}/v_{the}$=0.28, where v_{the} is the electron thermal velocity, $\sqrt{\langle v_{osc}^2 \rangle} = \sqrt{\langle (eE/m_e\omega_0)^2 \rangle} \propto \sqrt{\langle I\lambda^2 \rangle}$ is the electron quiver velocity in the average laser intensity assuming a constant wavelength. In simulations and in Fig. 6.2 the laser beam propagates in the direction normal to the plane of Fig. 6.2. Laser intensity distribution corresponds to the spot size, scaled by 0.3, in the center of the L_x=L_y=1mm of Fig. 6.2. The plasma flow is in the plane of the figure at $\vec{v}_\perp$=1.2c_s from the bottom up. An emerging bow shock structure is clearly seen on the scale of the whole beam. Density perturbations along the plasma flow are on the order of 20%. A noticeable feature of the flow interaction with the laser beam in the down-stream region is the transverse modulations in plasma density and velocity. These modulations were predicted [96], and result from the layering instability. Further downstream, in the region where there is no direct laser plasma coupling, the modulated flow becomes turbulent as the result of the Kelvin-Helmholtz instability. Accounting for these processes in the modeling of laser plasma coupling in ICF targets will alter our understanding of CBET, scattering instabilities, absorption and transport in the LEH region.

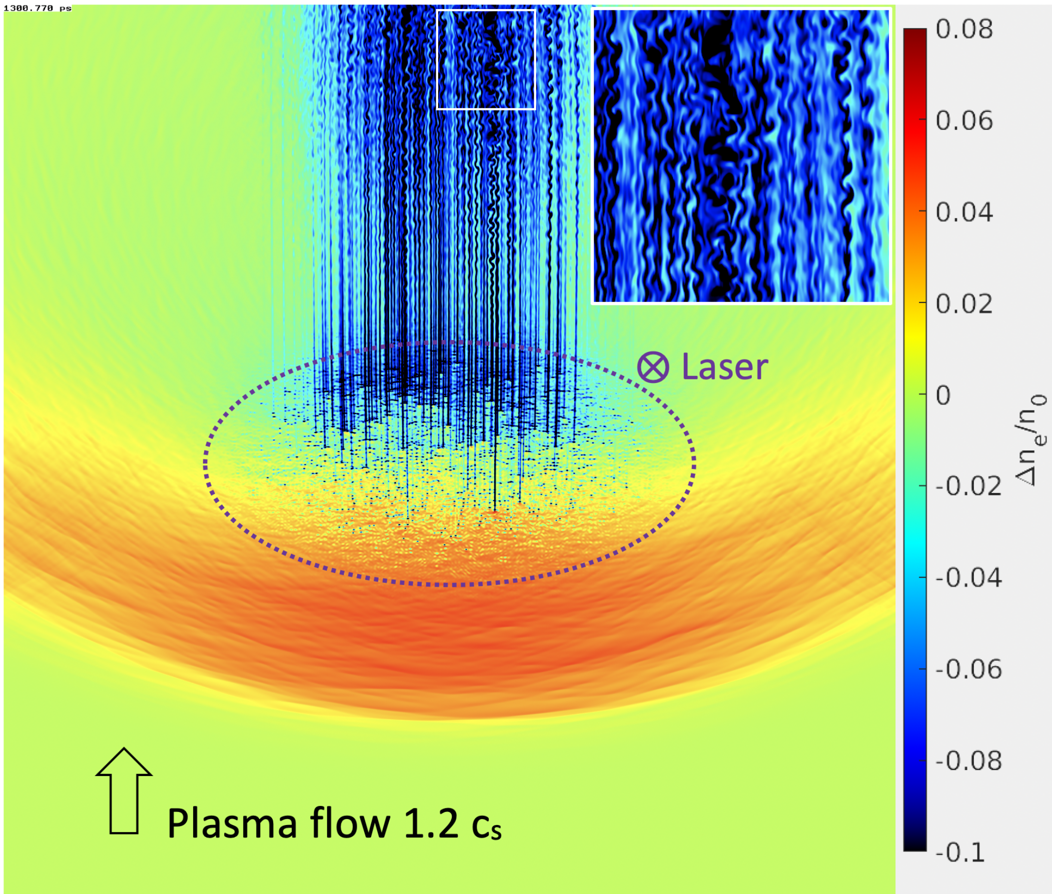

FIGURE 6.2: Density perturbations due to plasma flow across a NIF quad from pF3D simulations. In this simulation the laser is propagating into the page and the transverse plasma flow is in the upward direction. Note the inset shows the Kelvin-Helmholtz instability and a transition to turbulence in the upstream plasma flow.

6.2 Drag Force on a Flowing Plasma

When transverse fluctuations in a laser field are large compared to fluctuations along the propagation axis, the hydrodynamic model may be simplified to two dimensions, so that only the fluid momentum component perpendicular to the laser axis is effected. Using linearized isothermal hydrodynamics, it has been shown [29], an expression for the deflection rate of a beam in a flowing plasma can be describe by Eq. 6.1.

$$\frac{\partial\langle\theta\rangle}{\partial z} = \frac{128}{45}\frac{\langle n\rangle}{n_c}\frac{1}{f\lambda}\frac{\langle U\rangle}{T_e} f(M, \nu_{ia}), \tag{6.1}$$

Where $\frac{\partial\langle\theta\rangle}{\partial z}$ is the average beam deflection rate along the propagation axis. The $\langle\rangle$ indicates an average over a group of speckles where fluctuations in quantities such as the plasma density n, and the laser ponderomotive potential U, are assumed to vary slowly compared to a speckle's width, $f\lambda$. Here n_c is the laser's critical density, and the ponderomotive potential is defined by its induced density fluctuation in a stationary plasma $\frac{U}{T_e} = \frac{\delta n}{\langle n \rangle} \approx \frac{1}{4}\frac{v_{osc}^2}{v_{the}^2}$.

Again from [29], the function $f(M, \nu_{ia})$ is given by:

$$f(M, \nu_{ia}) = \frac{2}{\pi}\int_0^{\pi/2} \frac{M\nu_{ia}cos(\theta)^2}{(1 - M^2cos(\theta)^2)^2 + 4M^2\nu_{ia}^2cos(\theta)^2}d\theta, \tag{6.2}$$

Here ν_{ia} is the ion acoustic amplitude damping rate normalized to the ion acoustic frequency. The integral represents a uniform disk of transverse wavenumber Fourier amplitudes with radius $\pi/f\lambda$. The $M = 1$ singularity is integrable, so that if M varies with z and goes through a sonic point the total angular deflection is finite. In the limit of small damping $\nu_{ia} \to 0$ with $M > 1$ the function $f(M, \nu_{ia})$ is approximated by:

$$f(M) \approx \frac{1}{2M\sqrt{M^2 - 1}}, \tag{6.3}$$

The drag coefficient α describing the loss in fluid momentum as a function of time is derived in [96] using the isothermal fluid equations 6.4-6.8. Here $\vec{p} = \rho\vec{v}$ represents the fluids momentum density.

$$\frac{\partial \vec{p_\perp}}{\partial t} + \vec{\nabla}_\perp \cdot (\vec{v_\perp}\vec{p_\perp}) = -c_s^2\vec{\nabla}_\perp\rho - c_s^2\rho\nabla_\perp(\frac{U}{T_e}), \tag{6.4}$$

$$\frac{\partial \rho}{\partial t} + \vec{\nabla}_\perp \cdot \vec{p_\perp} = 0, \tag{6.5}$$

Each of these fields has a local mean and fluctuations, ex

$$\vec{p_\perp} = \langle \vec{p_\perp} \rangle + \delta\vec{p_\perp}, \tag{6.6}$$

When the fluctuations are ignored except in the last term on the RHS of Eq. 6.4, then

$$\frac{\partial \langle \vec{p_\perp} \rangle}{\partial t} + \vec{\nabla}_\perp \cdot (\langle \vec{p_\perp} \rangle \langle \vec{v_\perp} \rangle) = -\alpha\langle \vec{p_\perp} \rangle - c_s^2\langle \rho \rangle \nabla_\perp(\ln\langle \rho \rangle + \frac{\langle U \rangle}{T_e}), \tag{6.7}$$

$$\frac{\partial \langle \rho \rangle}{\partial t} + \vec{\nabla}_\perp \cdot (\langle \rho \rangle \langle \vec{v_\perp} \rangle) = 0, \tag{6.8}$$

When U/T_e is small, then the fluctuation coupling results in a term, $\alpha\langle\vec{p_\perp}\rangle$, pointing along the local momentum direction for the isotropic RPP disk model. Otherwise, α must be generalized to a tensor. The drag coefficient, α, is given by Eq. (28) of Ref. [96].

$$\alpha = 2\frac{\langle U\rangle}{T_e}\frac{\langle n_c\rangle}{n}c_s\frac{1}{M}\frac{\partial\langle\theta\rangle}{\partial z}, \tag{6.9}$$

We can now find analytic results for shock formation due to drag from an idealized laser beam whose spatial envelope is a slab, only varying in the x-direction. Assume steady state flow in the positive x-direction with incident Mach number, $M > 1$, specified at x = 0 and initial unperturbed density profile. Using the small damping limit Eq. 6.3, steady state solutions of Eqs. 6.7 and 6.8 imply

$$\frac{90}{256}\frac{d}{dx}(M+\frac{1}{M}) = -\frac{1}{M^2\sqrt{M^2-1}}, \tag{6.10}$$

Sonic flow, $M = 1$ is reached at $x = x_{sonic}$

$$x_{sonic} = \frac{90}{256}\int_1^M (u^2-1)^3/2 = \frac{90}{2048}\left[M(2M^2-5)\sqrt{M^2-1}+3\ln\left[2(\sqrt{M^2-1}+M)\right]\right], \tag{6.11}$$

Where u is the flow velocity, and x_{sonic} is the normalized distance the supersonic plasma can penetrate into the laser spot. The normalization of x_{sonic} is chosen such that the units of length are $F\lambda/(U/T_e)^2$. This normalization is convenient since the theoretical scaling can account for multiple variables with one curve as in the scaling results shown in figure 6.3. Conservation of momentum implies that if there is a drag on the flow, then the beam must deflect in the opposite direction of the drag. In the images of figure 6.4 a single NIF like beam is compared with 4 NIF like beams arranged in a "quad". The figures demonstrate that the effect of 4 beams not only gives 4x the intensity in the focal spot but also results in smaller speckles which have a larger ponderomotive force. Note that this is particularly relevant in Eqs. 6.9 and 6.11, where the drag coefficient and shock distance are dependent on ponderomotive potential and the speckle size.

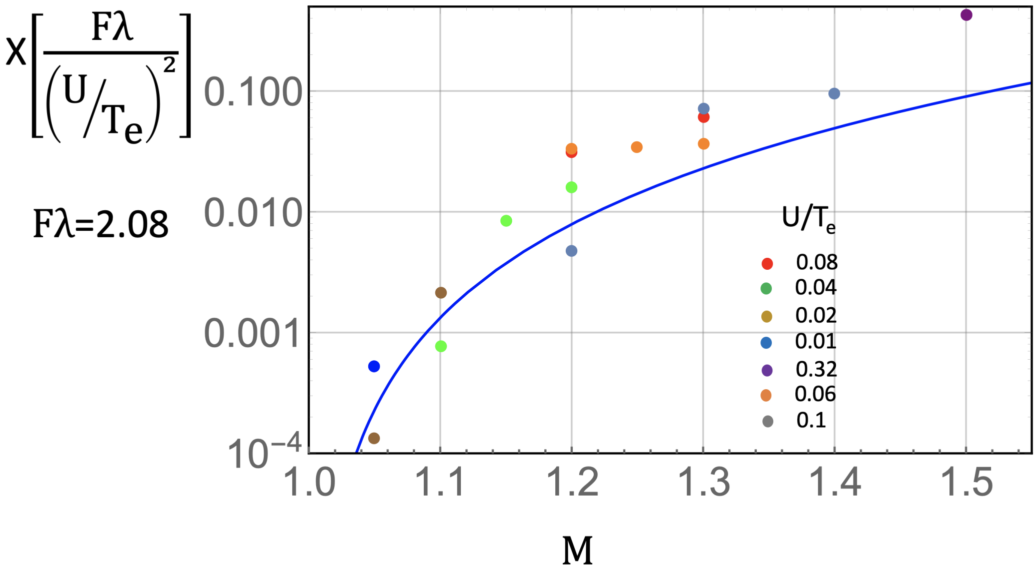

FIGURE 6.3: Comparison between linear scaling for the length necessary to slow down the flow below sonic velocity and nonlinear hydro simulations in 2D.

6.3 Non-Linear Hydrodynamic Simulations

Initial modeling of the laser and hydrodynamics response was performed with pF3D (c.f. figs. 6.1 and 6.2) on the Quartz supercomputer at LLNL. To continue this work in Alberta, CLAWPACK was setup on Compute Canada's Cedar supercomputer. The laser focus intensity was generated using Fourier optics (see sec. A.3). CLAWPACK is a non-linear second order hydrodynamics code written and described by Randall LeVeque [54], and modified for plasma physics [35],[34]. The fluid equations assume a neutral plasma and operate on an ion response time-scale (sub-picco second time steps). The fluid plasma is subject to the ponderomotive force of a lasers focal spot in 2D. Simulations were performed in this 2D x-y geometry where the laser would propagate in z. The laser intensity and plasma flow was varied to obtain the scaling of equation 6.11. The laser profile was generated using Fourier optics with wavelength $\lambda = 351\mu m$, an f-number of 6, and a second order elliptical super Gaussian focal spot size of approximately $100\mu m$ in diameter transverse to the flow and $80\mu m$ in diameter parallel to the flow. All simulations used the exact same laser profile (speckle pattern), but the intensity of the pattern was varied. The plasma density $n = 0.1n_c$, and ion acoustic damping rate $\nu_{ia} = 0.05\omega_{ia}$, were also constant throughout all the simulations.

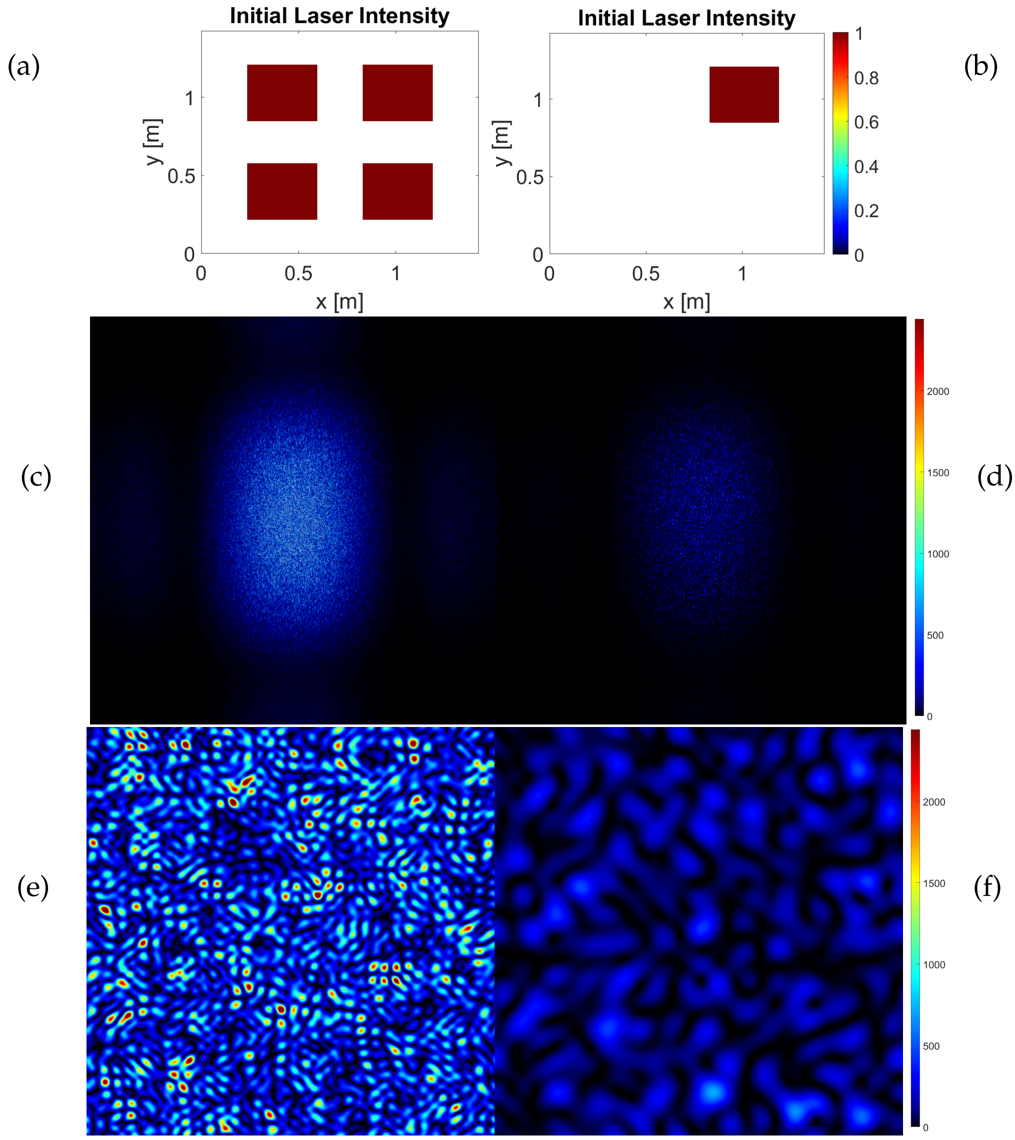

FIGURE 6.4: **Top:** Light incident to the lens. (a) Full NIF quad. (b) Single beam from NIF quad. **Center:** Focal spot intensity profile. (c) Full NIF quad. (d) Single beam from NIF quad. Note that both figures cover the same area of space and have the same colorbar. **Bottom:** Focal spot intensity profile zoomed in. (e) Full NIF quad. (f) Single beam from NIF quad. Note that both figures cover the same area of space and have the same colorbar.

Figures 6.5 and 6.6 show typical simulation results for the plasma density and flows velocity at t=4000λ/c_s. The laser speckles can be observed to slow down the flow of the plasma as it enters the speckle and accelerate it on its way out. The cumulative effect of the many speckles over a distance results in a large scale bow shock wrapping around the laser pulse.

To determine the distance into the laser spot where the flow becomes subsonic,

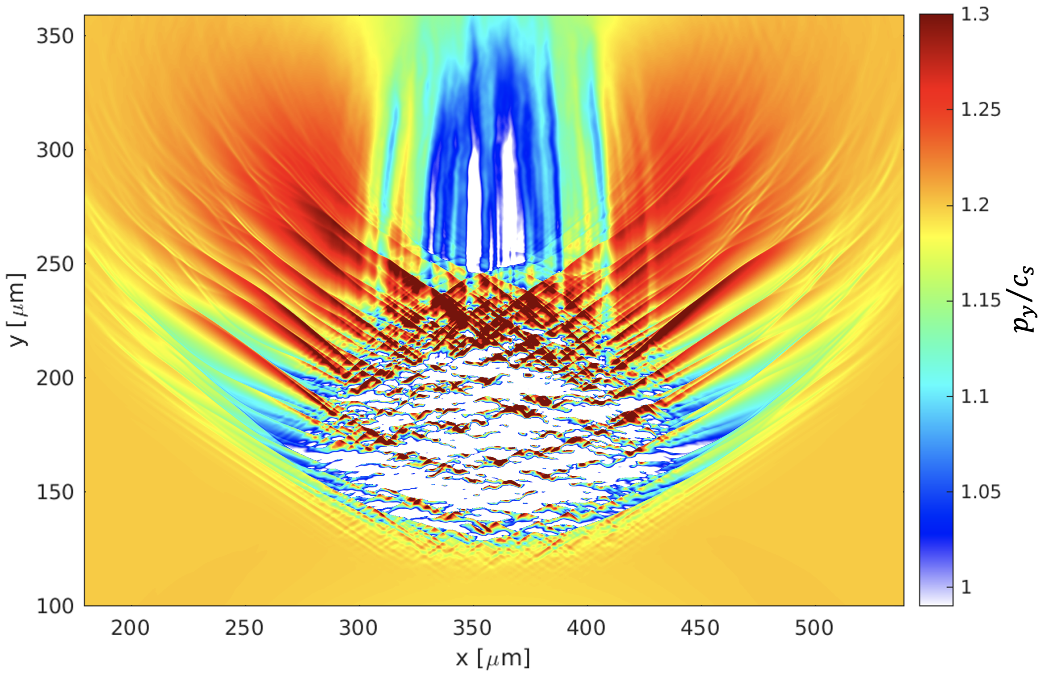

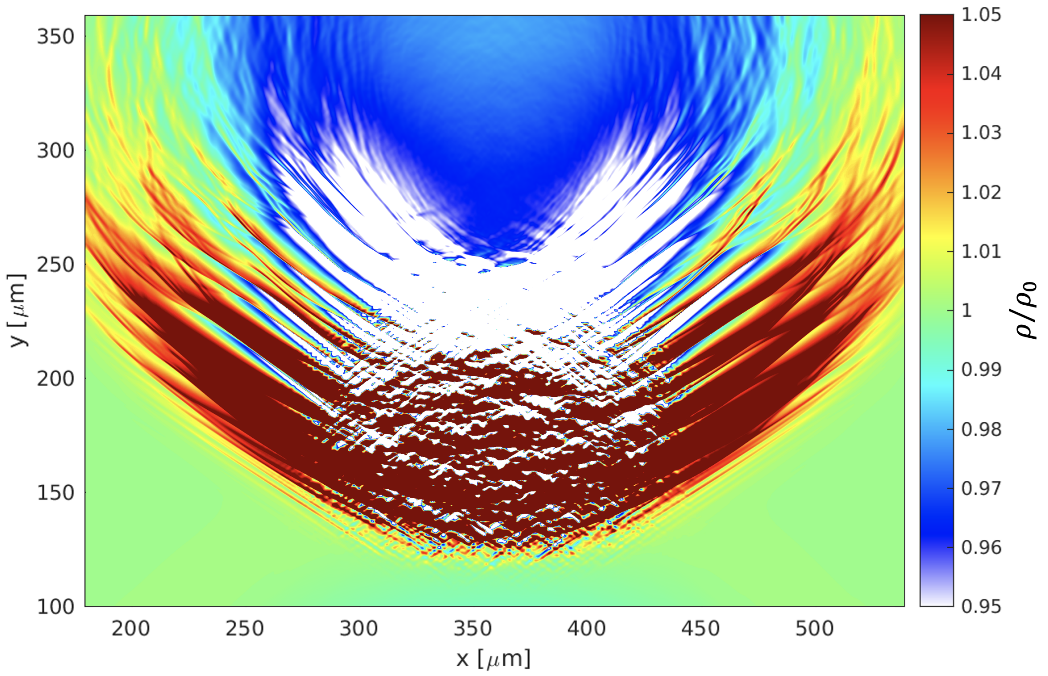

FIGURE 6.5: Example of CLAW simulation. Top: Fluid momentum. Bottom: Fluid Density. Both at t=4000λ/c_s. Parameters correspond to case no. 17.

x_{sonic}, line-outs were taken through the center of the simulation box, along the y-direction, and averaged over 64 x-gridpoints. The lowest y-value where the plasma flow was less than sonic was tracked in time. After investigating the data in time for its validity, the lowest y-value from all simulations was taken at t=3040λ/c_s. The value of x_{sonic} was determined by subtracting a constant from the lowest y-value and

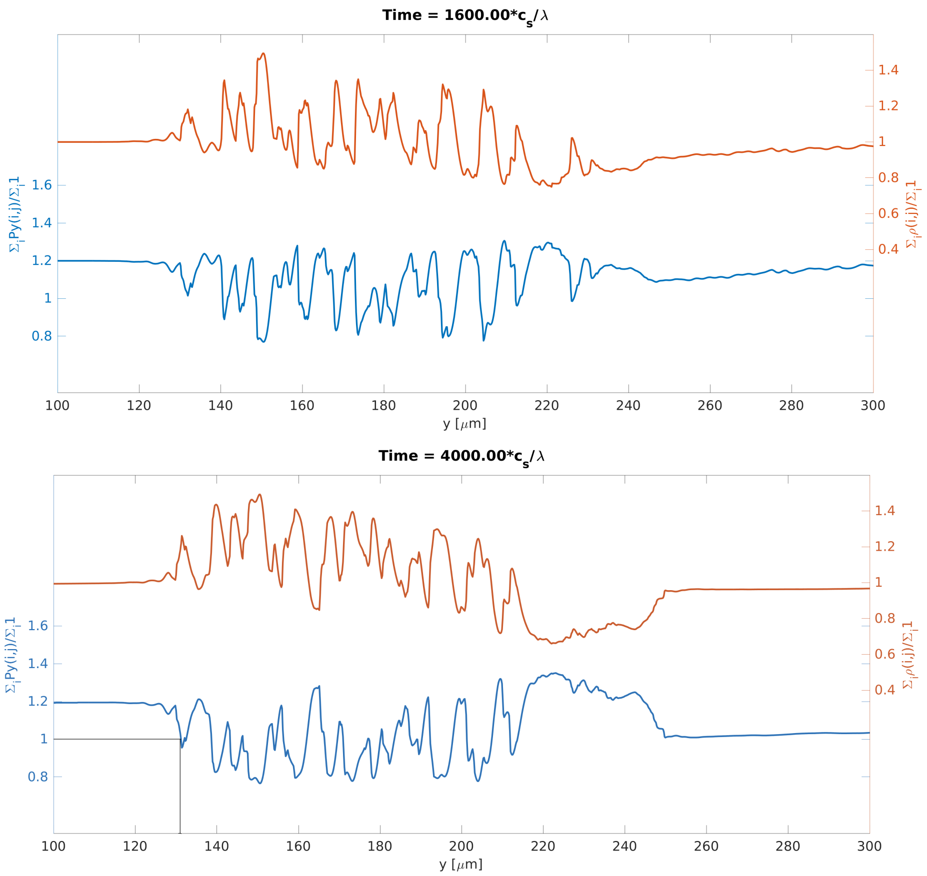

FIGURE 6.6: Example of CLAW simulation. Line-outs taken through the center of the box, along the y-direction, and averaged over 65 x-gridpoints (32 on each side). Plots show of the density (orange) and flow velocity (blue) along the y-axis. Parameters correspond to case no. 17. The simulation distance to shock y^*_{sonic}, is illustrated in the lower figure.

recorded in table 6.1 along with other relevant scaling parameters.

Table 6.1, and Figure 6.3 show the results of 23 simulations renormalized to fit one scaling curve. The scaling shows very good agreement with the simulation data when subtracting the constant value $127\mu m$ from the offset raw data. Deviations in the data are likely due to the effect of individual laser speckles, the data could be improved in the future by using a larger simulation box and focal spot size. With a larger focal spot, one can average over more speckles transverse to the flow in order to recover the quasi-1D slab model. The simulations include Landau damping of the ion acoustic waves with damping rate $\nu_{ia}/\omega_{ia} = 0.05$, while the theoretical scaling has assumed no damping. The damping reduces the amplitude of ion acoustic perturbations and therefore the process of slowing the flow. The effects of the damping

Case	v_{flow}/c_s	U/T_e	$\langle n\rangle/n_c$	$f\lambda[\mu m]$	ν_{ia}/ω_{ia}	y^*_{sonic}
1	1.1	0.08	0.1	2.08	0.05	126.4217
2	1.3	0.08	0.1	2.08	0.05	149.9502
3	1.05	0.08	0.1	2.08	0.05	122.5588
4	1.2	0.08	0.1	2.08	0.05	140.1174
5	1.1	0.32	0.1	2.08	0.05	119.5739
6	1.3	0.32	0.1	2.08	0.05	127.2997
7	1.5	0.32	0.1	2.08	0.05	138.7127
8	1.01	0.01	0.1	2.08	0.05	122.7344
9	1.05	0.01	0.1	2.08	0.05	140.6442
10	1.01	0.02	0.1	2.08	0.05	122.0321
11	1.05	0.02	0.1	2.08	0.05	130.8114
12	1.1	0.02	0.1	2.08	0.05	140.9953
13	1.05	0.04	0.1	2.08	0.05	126.0706
14	1.1	0.04	0.1	2.08	0.05	131.1625
15	1.15	0.04	0.1	2.08	0.05	140.9953
16	1.2	0.04	0.1	2.08	0.05	150.8281
17	1.2	0.10	0.1	2.08	0.05	131.3381
18	1.3	0.10	0.1	2.08	0.05	145.3850
19	1.4	0.10	0.1	2.08	0.05	150.4770
20	1.1	0.10	0.1	2.08	0.05	127.1241
21	1.2	0.06	0.1	2.08	0.05	149.2479
22	1.25	0.06	0.1	2.08	0.05	150.3014
23	1.3	0.06	0.1	2.08	0.05	151.3549

TABLE 6.1: List of all simulations cases. The columns are as follows: case number, plasma flow velocity v_{flow}/c_s, laser ponderomotive potential / electron thermal velocity U/T_e, average plasma density / critical density $\langle n\rangle/n_c$, f-number times the wavelength $f\lambda$, ion acoustic damping rate / ion acoustic frequency ν_{ia}/ω_{ia}, simulation distance to shock y^*_{sonic}.

are frequency dependent and the damping does not scale with U/Te, so the damping can't be normalized into the same scaling theory shown in Fig. 6.3. The effects of the damping are expected to cause deviations from the curve and variations in the data.

6.4 Conclusion

Non-linear hydrodynamics simulations match the theoretical scaling [29] for the distance to shock a supersonic plasma with a laser's ponderomotive potential. This chapter is part of an ongoing study of laser induced shock formation in flowing plasmas. The project was awarded a Discovery Science campaign on the NIF, with shots taking place after the completion of this thesis. I plan to publish the simulation scaling results demonstrated in this chapter, and to continue this by looking at the effects of SSD, and at 3D crossed beam geometries. SSD causes speckle motion and may result in smoothing of the drag force on timescales much larger than the SSD period. Many crossed beams at large angles (e.g. NIF hemisphere 96 beams), result in fine scale speckle patterns with many beat waves. The scaling in this chapter assumes speckles were long along their propagation axis (transverse to the flow) compared to their width, which is not necessarily accurate for speckles in NIF like geometries (see figure A.6, where the flow may pass through laser speckles that are more spherical.

Chapter 7

Conclusions and Future Work

7.1 ICF

In Chapter 5 a new high bandwidth laser based plasma diagnostic was proposed. Experiments with similar configurations to this have been performed without the bandwidth [121], however the bandwidth is critical to single shot probing. We plan to test the proposed probe in experiments as high bandwidth lasers in this configuration become available. Throughout the work on this project, we performed detailed studies of the effects of bandwidth with a variety of optical components. Modest amounts of bandwidth have historically been used for beam smoothing (SSD) on the NIF. We plane to investigate high bandwidth as a method of speeding up speckle motion for mitigating CBET, SRS, SBS, and hydrodynamic instabilities and the effects of the bandwidth itself on avoiding unwanted resonances in LPI.

Work related to ICF in Chapter 6 was awarded Discovery Science shots on the NIF. We are currently planning the experiment and running simulations of the LPI. The experiment will involve a setup with planer target being shot with both hemispheres of the NIF. The outer beams (44.5^o and 50^o) will only be shot from one side, while the inner beams (23.5^o and 30^o) will shoot from both sides. On both sides of the target the inner beams will ionize the surface of the target to create a supersonic plume of expanding plasma. On the side with both inner and outer cones of beams, the inner beams will cross near the sonic point to slow the plasma and cause a bow shock. The experiment will be imaged with a gated x-ray diagnostic from the side so that both expanding plumes can bee seen and the effects of the inner beams can be contrasted with the reference side. An early rendering of the laser geometry is shown in figure 7.1. Here 96+32=128 (of 192) paraxial NIF lasers are shown in a custom colormap, with a gold cylindrical target. Two 3D portals were used to have dynamic vision of the geometry.

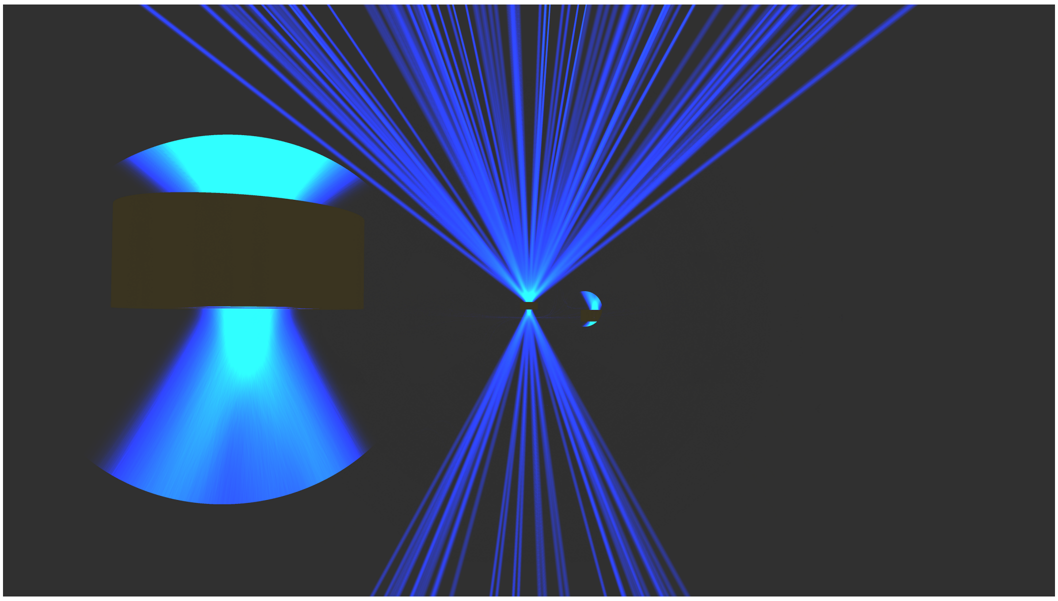

FIGURE 7.1: A 3D rendering of the NIF lasers and target geometry with portals. 10 reflections or iterations of the portals were performed.

Non-linear hydrodynamic simulations show significant slowing of the plasma with single beams and small spot sizes (cf. Chapter 6). We are currently running larger simulations with larger laser spots and plan to consider the effects of SSD. The Kelvin-Helmholtz instability was observed in simulations of the flowing plasma after passing through a laser focus. We plan to analyze and characterize the instability for conditions relevant to ICF plasmas.

7.2 LWFA and Mid-IR

In Chapters 2, 3, and 4 of this thesis, improvements to short pulse laser based particle acceleration and radiation production were investigated. In Chapter 2 theoretical and numerical modeling were used to demonstrate that a BRA can amplify or sustain a laser pulse to improve wake generation for particle acceleration in a plasma. In Chapter 3 PIC simulations revealed deeper insight into the bubble formation of LWFA in the relativistic regime. Here PIC simulations were compared with experimental results to show that backward SRS from the wake driving laser pulse can be a possible method of diagnosing bubble formation. The investigation of producing mid-IR from LWFA in Chapter 4 is part of an ongoing study. A large 3D PIC simulation is currently being analyzed for comparison with the 2D simulations and experiment. Preliminary results of this simulation are shown in figure 7.2. The 3D PIC simulation reveals additional physics including the formation of a tube like structure of high plasma density surrounding the receding mid-IR light as it passes through the back of the bubbles. With further analysis the 3D simulation should allow for more insight into the physics and provide a high resolution dataset for figures. As if figure 4.8d the color bar of the electric field can be applied in Fourier space to allow for rendering of realistic colors. We plane to extend this capability to the rendering software developed during this thesis.

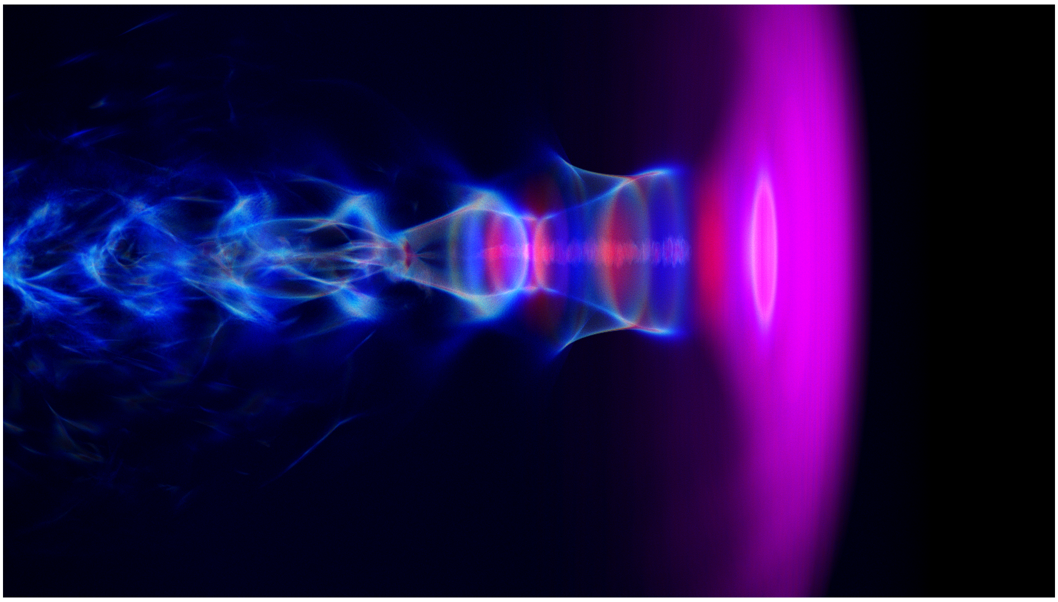

FIGURE 7.2: A 3D OSIRIS simulation of LWFA in the Blowout regime. Both the plasma density and laser electric fields are displayed. The plasma density is shown from blue ($1.4n_0$) to red ($4.5n_0$) in a jet colormap. The laser electric field is shown from $eE/m_ec\omega_0$=-0.75 to +0.75 in a red-blue colormap.

7.3 Rendering

Many figures in this thesis were generated using parallel ray tracing. The code Rayven (c.f. A.4) was developed during the course of this Ph.D. work for advanced visualization of large datasets produced by simulations. Many High Performance

Computing (HPC) codes are capable of preforming 3D simulations at high resolutions in space and time. Due to the extreme sizes of the data sets most HPC codes only dump simulation output files "snapshots" at predefined intervals of time-steps to save storage space and post-processing time. In future work Rayven can be implemented in distributed memory to avoid slow input-output, and provide live visualization of HPC simulations. In many HPC codes the simulation domain is decomposed for parallelism, Rayven has also been domain decomposed and can be incorporated into these simulations with little additional computational cost.

The algorithm used in Raven has already been extended to support Virtual Reality (VR) by using two cameras separated in space. Currently for non-trivial environments the frame-rate is well below the 90Hz required for comfortable viewing in VR. With performance optimizations and new hardware we plan to improve the frame rates and continue development for VR support. The code Rayven was also equipped with a dynamic bounding volume hierarchy to allow for rendering of more complex environments involving large numbers of objects. A game engine was developed to allow for users and artificial intelligence (AI) to have control of the camera and interact with the environments. In future work we plane to improve the game engine architecture to provide interactive physics simulations and a sandbox for AI.

Bibliography

[1] Félicie Albert and Alec G R Thomas. "Applications of laser wakefield accelerator-based light sources". In: *Plasma Physics and Controlled Fusion* 58.10 (2016), p. 103001. DOI: 10.1088/0741-3335/58/10/103001. URL: https://doi.org/10.1088%2F0741-3335%2F58%2F10%2F103001.

[2] A. A. Andreev et al. "Short light pulse amplification and compression by stimulated Brillouin scattering in plasmas in the strong coupling regime". In: *Physics of Plasmas* 13.5 (2006), p. 053110. DOI: 10.1063/1.2201896. eprint: https://doi.org/10.1063/1.2201896. URL: https://doi.org/10.1063/1.2201896.

[3] N.E. Andreev and S.Yu. Kalmykov. "Backward stimulated Raman scattering of a modulated laser pulse in plasmas". In: *Physics Letters A* 227.1 (1997), pp. 110 –116. ISSN: 0375-9601. DOI: https://doi.org/10.1016/S0375-9601(97)00016-9. URL: http://www.sciencedirect.com/science/article/pii/S0375960197000169.

[4] R. L. Berger et al. "Influence of Spatial and Temporal Laser Beam Smoothing on Stimulated Brillouin Scattering in Filamentary Laser Light". In: *Phys. Rev. Lett.* 75 (6 1995), pp. 1078–1081. DOI: 10.1103/PhysRevLett.75.1078. URL: https://link.aps.org/doi/10.1103/PhysRevLett.75.1078.

[5] R. L. Berger et al. "Multi-dimensional Vlasov simulations and modeling of trapped-electron-driven filamentation of electron plasma waves". In: *Physics of Plasmas* 22.5 (2015), p. 055703. DOI: 10.1063/1.4917482. eprint: https://aip.scitation.org/doi/pdf/10.1063/1.4917482. URL: https://aip.scitation.org/doi/abs/10.1063/1.4917482.

[6] R. L. Berger et al. "On the dominant and subdominant behavior of stimulated Raman and Brillouin scattering driven by nonuniform laser beams". In:

Physics of Plasmas 5.12 (1998), pp. 4337–4356. DOI: 10.1063/1.873171. eprint: https://doi.org/10.1063/1.873171. URL: https://doi.org/10.1063/1.873171.

[7] N Bloembergen, AH Zewail, and A Amos. "Energy Redistribution in Isolated Molecules and the Question of Mode-Selective Laser Chemistry Revisited". In: *J. Phys. Chem* 88 (1984), pp. 5459–5465. URL: https://pubs.acs.org/doi/pdf/10.1021/j150667a004.

[8] S. V. Bulanov et al. "Transverse-Wake Wave Breaking". In: *Phys. Rev. Lett.* 78 (22 1997), pp. 4205–4208. DOI: 10.1103/PhysRevLett.78.4205. URL: https://link.aps.org/doi/10.1103/PhysRevLett.78.4205.

[9] Sergei V Bulanov et al. "Relativistic mirrors in plasmas. Novel results and perspectives". In: *Physics-Uspekhi* 56.5 (2013), pp. 429–464. DOI: 10.3367/ufne.0183.201305a.0449. URL: https://doi.org/10.3367%2Fufne.0183.201305a.0449.

[10] M. Chiaramello et al. "Role of Frequency Chirp and Energy Flow Directionality in the Strong Coupling Regime of Brillouin-Based Plasma Amplification". In: *Phys. Rev. Lett.* 117 (23 2016), p. 235003. DOI: 10.1103/PhysRevLett.117.235003. URL: https://link.aps.org/doi/10.1103/PhysRevLett.117.235003.

[11] A. Colaïtis et al. "Crossed beam energy transfer: Assessment of the paraxial complex geometrical optics approach versus a time-dependent paraxial method to describe experimental results". In: *Physics of Plasmas* 23.3 (2016), p. 032118. DOI: 10.1063/1.4944496. eprint: https://doi.org/10.1063/1.4944496. URL: https://doi.org/10.1063/1.4944496.

[12] A. Colaïtis et al. "Towards modeling of nonlinear laser-plasma interactions with hydrocodes: The thick-ray approach". In: *Phys. Rev. E* 89 (3 2014), p. 033101. DOI: 10.1103/PhysRevE.89.033101. URL: https://link.aps.org/doi/10.1103/PhysRevE.89.033101.

[13] C.A. Coverdale et al. "Properties of the spectra of relativistically strong laser pulses in an underdense plasma". In: *Plasma Physics Reports* 22.8 (Aug. 1996), pp. 617–624. URL: http://dx.doi.org/10.1134/1.952331.

[14] J. Cowley et al. “Excitation and Control of Plasma Wakefields by Multiple Laser Pulses”. In: *Phys. Rev. Lett.* 119 (4 2017), p. 044802. DOI: 10.1103/PhysRevLett.119.044802. URL: https://link.aps.org/doi/10.1103/PhysRevLett.119.044802.

[15] C. B. Darrow et al. “Strongly coupled stimulated Raman backscatter from subpicosecond laser-plasma interactions”. In: *Phys. Rev. Lett.* 69 (3 1992), pp. 442–445. DOI: 10.1103/PhysRevLett.69.442. URL: https://link.aps.org/doi/10.1103/PhysRevLett.69.442.

[16] A. S. Davies et al. “Picosecond Thermodynamics in Underdense Plasmas Measured with Thomson Scattering”. In: *Phys. Rev. Lett.* 122 (15 2019), p. 155001. DOI: 10.1103/PhysRevLett.122.155001. URL: https://link.aps.org/doi/10.1103/PhysRevLett.122.155001.

[17] J. M. Dias, L. Oliveira e Silva. “Photon acceleration versus frequency-domain interferometry for laser wakefield diagnostics”. In: *Phys. Rev. ST Accel. Beams* 1 (3 1998), p. 031301. DOI: 10.1103/PhysRevSTAB.1.031301. URL: https://link.aps.org/doi/10.1103/PhysRevSTAB.1.031301.

[18] S. N. Dixit et al. “Random phase plates for beam smoothing on the Nova laser”. In: *Appl. Opt.* 32.14 (1993), pp. 2543–2554. DOI: 10.1364/AO.32.002543. URL: http://ao.osa.org/abstract.cfm?URI=ao-32-14-2543.

[19] R. Dragila and J. Krepelka. “Laser plasma density profile modification by ponderomotive force”. In: *Journal de Physique* 39 (6 1978), pp. 617–623. DOI: 10.1051/jphys:01978003906061700. URL: https://hal.archives-ouvertes.fr/jpa-00208793.

[20] B. Ersfeld and D. A. Jaroszynski. “Superradiant Linear Raman Amplification in Plasma Using a Chirped Pump Pulse”. In: *Phys. Rev. Lett.* 95 (16 2005), p. 165002. DOI: 10.1103/PhysRevLett.95.165002. URL: https://link.aps.org/doi/10.1103/PhysRevLett.95.165002.

[21] E. Esarey, C. B. Schroeder, and W. P. Leemans. “Physics of laser-driven plasma-based electron accelerators”. In: *Rev. Mod. Phys.* 81 (3 2009), pp. 1229–1285. DOI: 10.1103/RevModPhys.81.1229. URL: https://link.aps.org/doi/10.1103/RevModPhys.81.1229.

[22] E. Esarey, A. Ting, and P. Sprangle. "Frequency shifts induced in laser pulses by plasma waves". In: *Phys. Rev. A* 42 (6 1990), pp. 3526–3531. DOI: 10.1103/PhysRevA.42.3526. URL: https://link.aps.org/doi/10.1103/PhysRevA.42.3526.

[23] J. Faure et al. "A laser-plasma accelerator producing monoenergic electron beams". In: *Nature* 431 (2004), pp. 541–544. URL: https://doi.org/10.1038/nature02963.

[24] F. Fiuza et al. "Laser-Driven Shock Acceleration of Monoenergetic Ion Beams". In: *Phys. Rev. Lett.* 109 (21 2012), p. 215001. DOI: 10.1103/PhysRevLett.109.215001. URL: https://link.aps.org/doi/10.1103/PhysRevLett.109.215001.

[25] R A Fonseca et al. "One-to-one direct modeling of experiments and astrophysical scenarios: pushing the envelope on kinetic plasma simulations". In: *Plasma Physics and Controlled Fusion* 50.12 (2008), p. 124034. DOI: 10.1088/0741-3335/50/12/124034. URL: https://doi.org/10.1088%2F0741-3335%2F50%2F12%2F124034.

[26] R. A. Fonseca et al. "OSIRIS: A Three-Dimensional, Fully Relativistic Particle in Cell Code for Modeling Plasma Based Accelerators". In: *Computational Science — ICCS 2002*. Ed. by Peter M. A. Sloot et al. Berlin, Heidelberg: Springer Berlin Heidelberg, 2002, pp. 342–351. ISBN: 978-3-540-47789-1.

[27] D. H. Froula et al. "Plasma Scattering of Electromagnetic Radiation: Theory and Measurement Techniques". In: *Elsevier and Amsterdam* (2011). URL: https://doi.org/10.1016/C2009-0-20048-1.

[28] C. G. R. Geddes et al. "High-quality electron beams from a laser wakefield accelerator using plasma-channel guiding". In: *Nature* 431 (2004), pp. 538–541. URL: https://doi.org/10.1038/nature02900.

[29] Sandip Ghosal and Harvey A. Rose. "Two-dimensional plasma flow past a laser beam". In: *Physics of Plasmas* 4.7 (1997), pp. 2376–2396. DOI: 10.1063/1.872219. eprint: https://doi.org/10.1063/1.872219. URL: https://doi.org/10.1063/1.872219.

[30] R. J. Henchen et al. "Observation of Nonlocal Heat Flux Using Thomson Scattering". In: *Phys. Rev. Lett.* 121 (12 2018), p. 125001. DOI: 10.1103/PhysRevLett.121.125001. URL: https://link.aps.org/doi/10.1103/PhysRevLett.121.125001.

[31] D. E. Hinkel et al. "Stimulated Raman scatter analyses of experiments conducted at the National Ignition Facility". In: *Physics of Plasmas* 18.5 (2011), p. 056312. DOI: 10.1063/1.3577836. eprint: https://doi.org/10.1063/1.3577836. URL: https://doi.org/10.1063/1.3577836.

[32] RM Hochstrasser. "Two-dimensional spectroscopy at infrared and optical frequencies". In: *Proceedings of the National Academy of Sciences* 104.36 (2007), pp. 14190–14196. ISSN: 0027-8424. DOI: 10.1073/pnas.0704079104. URL: http://www.ncbi.nlm.nih.gov/pubmed/10051590http://www.pubmedcentral.nih.gov/articlerender.fcgi?artid=PMC26732http://www.pnas.org/cgi/doi/10.1073/pnas.0704079104.

[33] A Hoffman. "Extending opportunities". In: *Nature Photonics* 6.7 (2012), p. 407. ISSN: 17494885. DOI: 10.1038/nphoton.2012.164. URL: http://www.nature.com/articles/nphoton.2012.164.

[34] S Hüller et al. "Crossed beam energy transfer in the presence of laser speckle ponderomotive self-focusing and nonlinear sound waves". In: *Physics of Plasmas* 27.2 (2020), p. 022703. DOI: 10.1063/1.5125759. eprint: https://doi.org/10.1063/1.5125759. URL: https://doi.org/10.1063/1.5125759.

[35] S. Hüller et al. "Harmonic decomposition to describe the nonlinear evolution of stimulated Brillouin scattering". In: *Physics of Plasmas* 13.2 (2006), p. 022703. DOI: 10.1063/1.2168403. eprint: https://doi.org/10.1063/1.2168403. URL: https://doi.org/10.1063/1.2168403.

[36] Stefan Hüller et al. "Crossed beam energy transfer between optically smoothed laser beams in inhomogeneous plasmas". In: *Philosophical Transactions of the Royal Society A: Mathematical, Physical and Engineering Sciences* 378.2184 (2020), p. 20200038. DOI: 10.1098/rsta.2020.0038. eprint: https://royalsocietypublishing.org/doi/pdf/10.1098/rsta.2020.0038. URL: https://royalsocietypublishing.org/doi/abs/10.1098/rsta.2020.0038.

[37] A E Hussein et al. "Stimulated Raman backscattering from a laser wakefield accelerator". In: *New Journal of Physics* 20.7 (2018), p. 073039. DOI: 10.1088/1367-2630/aaceeb. URL: https://doi.org/10.1088%2F1367-2630%2Faaceeb.

[38] D. A. Jaroszynski et al. "Superradiance in a Short-Pulse Free-Electron-Laser Oscillator". In: *Phys. Rev. Lett.* 78 (9 1997), pp. 1699–1702. DOI: 10.1103/PhysRevLett.78.1699. URL: https://link.aps.org/doi/10.1103/PhysRevLett.78.1699.

[39] T. G. Jones et al. "Temporally resolved Raman backscattering diagnostic of high intensity laser channeling". In: *Review of Scientific Instruments* 73.6 (2002), pp. 2259–2265. DOI: 10.1063/1.1475348. eprint: https://doi.org/10.1063/1.1475348. URL: https://doi.org/10.1063/1.1475348.

[40] D Jung et al. *Next-generation mid-infrared sources*. Vol. 19. 12. IOP Publishing Ltd., 2017, p. 123001. DOI: 10.1088/2040-8986/aa939b. URL: http://stacks.iop.org/2040-8986/19/i=12/a=123001?key=crossref.fc2c9fe2c39f1a4464f9538acc71e95f.

[41] D. Kaganovich et al. "Compact, all-optical generation of coherent x-rays". In: *United States Patent Application Publication* 0014874 A1 (2016).

[42] D. Kaganovich et al. "Nonlinear frequency shift in Raman backscattering and its implications for plasma diagnostics". In: *Physics of Plasmas* 23.12 (2016), p. 123104. DOI: 10.1063/1.4971236. eprint: https://doi.org/10.1063/1.4971236. URL: https://doi.org/10.1063/1.4971236.

[43] R. K. Kirkwood et al. "A plasma amplifier to combine multiple beams at NIF". In: *Physics of Plasmas* 25.5 (2018), p. 056701. DOI: 10.1063/1.5016310. eprint: https://doi.org/10.1063/1.5016310. URL: https://doi.org/10.1063/1.5016310.

[44] R. K. Kirkwood et al. "Observation of Energy Transfer between Frequency-Mismatched Laser Beams in a Large-Scale Plasma". In: *Phys. Rev. Lett.* 76 (12 1996), pp. 2065–2068. DOI: 10.1103/PhysRevLett.76.2065. URL: https://link.aps.org/doi/10.1103/PhysRevLett.76.2065.

[45] S. Kneip et al. "Bright spatially coherent synchrotron X-rays from a table-top source". In: *Nature Physics* 6.980?983 (2010). URL: https://doi.org/10.1038/nphys1789.

[46] S. Kneip et al. "Bright spatially coherent synchrotron X-rays from table-top source". In: *Nature Physics* 6 (2010), pp. 980–983. URL: https://doi.org/10.1038/nphys1789.

[47] M. Kono and M. Škorić. *Nonlinear Physics of Plasmas*. Springer Series on Atomic, Optical, and Plasma Physics. Springer Berlin Heidelberg, 2010. ISBN: 9783642146947. URL: https://books.google.ca/books?id=fHDM99M49xIC.

[48] K. Krushelnick et al. "Second Harmonic Generation of Stimulated Raman Scattered Light in Underdense Plasmas". In: *Phys. Rev. Lett.* 75 (20 1995), pp. 3681–3684. DOI: 10.1103/PhysRevLett.75.3681. URL: https://link.aps.org/doi/10.1103/PhysRevLett.75.3681.

[49] A. Bruce Langdon. "Nonlinear Inverse Bremsstrahlung and Heated-Electron Distributions". In: *Phys. Rev. Lett.* 44 (9 1980), pp. 575–579. DOI: 10.1103/PhysRevLett.44.575. URL: https://link.aps.org/doi/10.1103/PhysRevLett.44.575.

[50] W. P. Leemans et al. "Observation of Terahertz Emission from a Laser-Plasma Accelerated Electron Bunch Crossing a Plasma-Vacuum Boundary". In: *Phys. Rev. Lett.* 91 (7 2003), p. 074802. DOI: 10.1103/PhysRevLett.91.074802. URL: https://link.aps.org/doi/10.1103/PhysRevLett.91.074802.

[51] W.P. Leemans et al. "GeV electron beams from a centimetre-scale accelerator". In: *Nature Physics* 2 (2006), pp. 696–699. URL: https://doi.org/10.1038/nphys418.

[52] R. H. Lehmberg, A. J. Schmitt, and S. E. Bodner. "Theory of induced spatial incoherence". In: *Journal of Applied Physics* 62.7 (1987), pp. 2680–2701. DOI: 10.1063/1.339419. eprint: https://doi.org/10.1063/1.339419. URL: https://doi.org/10.1063/1.339419.

[53] R.H. Lehmberg and S.P. Obenschain. "Use of induced spatial incoherence for uniform illumination of laser fusion targets". In: *Optics Communications* 46.1

(1983), pp. 27 –31. ISSN: 0030-4018. DOI: https://doi.org/10.1016/0030-4018(83)90024-X. URL: http://www.sciencedirect.com/science/article/pii/003040188390024X.

[54] Randall J. LeVeque. *Numerical Methods for Conservation Laws. Second Edition*. Birkhauser Basel, 1992.

[55] C. K. Li et al. "Observations of Electromagnetic Fields and Plasma Flow in Hohlraums with Proton Radiography". In: *Phys. Rev. Lett.* 102 (20 2009), p. 205001. DOI: 10.1103/PhysRevLett.102.205001. URL: https://link.aps.org/doi/10.1103/PhysRevLett.102.205001.

[56] J. Lin et al. "Adaptive control of laser-wakefield accelerators driven by mid-IR laser pulses". In: *Opt. Express* 27.8 (2019), pp. 10912–10923. DOI: 10.1364/OE.27.010912. URL: http://www.opticsexpress.org/abstract.cfm?URI=oe-27-8-10912.

[57] W. Lu et al. "A nonlinear theory for multidimensional relativistic plasma wave wakefields". In: *Physics of Plasmas* 13.5 (2006), p. 056709. DOI: 10.1063/1.2203364. eprint: https://doi.org/10.1063/1.2203364. URL: https://doi.org/10.1063/1.2203364.

[58] J. D. Ludwig et al. "Enhancement and control of laser wakefields via a backward Raman amplifier". In: *Physics of Plasmas* 25.5 (2018), p. 053108. DOI: 10.1063/1.5023387. eprint: https://doi.org/10.1063/1.5023387. URL: https://doi.org/10.1063/1.5023387.

[59] J. D. Ludwig et al. "Single shot high bandwidth laser plasma probe". In: *Physics of Plasmas* 26.11 (2019), p. 113108. DOI: 10.1063/1.5124401. eprint: https://doi.org/10.1063/1.5124401. URL: https://doi.org/10.1063/1.5124401.

[60] Pavel M Lushnikov and Harvey A Rose. "How much laser power can propagate through fusion plasma?" In: *Plasma Physics and Controlled Fusion* 48.10 (2006), pp. 1501–1513. DOI: 10.1088/0741-3335/48/10/004. URL: https://doi.org/10.1088%2F0741-3335%2F48%2F10%2F004.

[61] V. Malka et al. “Stimulated Raman backscattering instability in short pulse laser interaction with helium gas”. In: *Physics of Plasmas* 3.5 (1996), pp. 1682–1688. DOI: 10.1063/1.871688. eprint: https://doi.org/10.1063/1.871688. URL: https://doi.org/10.1063/1.871688.

[62] V. M. Malkin, G. Shvets, and N. J. Fisch. “Detuned Raman Amplification of Short Laser Pulses in Plasma”. In: *Phys. Rev. Lett.* 84 (6 2000), pp. 1208–1211. DOI: 10.1103/PhysRevLett.84.1208. URL: https://link.aps.org/doi/10.1103/PhysRevLett.84.1208.

[63] V. M. Malkin, G. Shvets, and N. J. Fisch. “Fast Compression of Laser Beams to Highly Overcritical Powers”. In: *Phys. Rev. Lett.* 82 (22 1999), pp. 4448–4451. DOI: 10.1103/PhysRevLett.82.4448. URL: https://link.aps.org/doi/10.1103/PhysRevLett.82.4448.

[64] V.M. Malkin and N.J. Fisch. “Key plasma parameters for resonant backward Raman amplification in plasma”. In: *Eur. Phys. J. Special Topics* 223 (2014), 1157?1167. URL: https://doi.org/10.1140/epjst/e2014-02168-0.

[65] S. P. D. Mangles et al. “Monoenergetic beams of relativistic electrons from intense laser-plasma interactions”. In: *Nature* 431 (2004), pp. 535–538. URL: https://doi.org/10.1038/nature02939.

[66] P. E. Masson-Laborde et al. “Evolution of the stimulated Raman scattering instability in two-dimensional particle-in-cell simulations”. In: *Physics of Plasmas* 17.9 (2010), p. 092704. DOI: 10.1063/1.3474619. eprint: https://doi.org/10.1063/1.3474619. URL: https://doi.org/10.1063/1.3474619.

[67] P. E. Masson-Laborde et al. “Giga-electronvolt electrons due to a transition from laser wakefield acceleration to plasma wakefield acceleration”. In: *Physics of Plasmas* 21.12 (2014), p. 123113. ISSN: 1089-7674. DOI: 10.1063/1.4903851. URL: http://dx.doi.org/10.1063/1.4903851.

[68] P.E. Masson-Laborde et al. “Giga-electronvolt electrons due to a transition from laser wakefield acceleration to plasma wakefield acceleration”. In: *Physics of Plasmas* 21.12 (2014), p. 123113. DOI: 10.1063/1.4903851. eprint: https://doi.org/10.1063/1.4903851. URL: https://doi.org/10.1063/1.4903851.

[69] T. Matsuoka et al. "Stimulated Raman Side Scattering in Laser Wakefield Acceleration". In: *Phys. Rev. Lett.* 105 (3 2010), p. 034801. DOI: 10.1103/PhysRevLett.105.034801. URL: https://link.aps.org/doi/10.1103/PhysRevLett.105.034801.

[70] C. McGuffey et al. "Ionization Induced Trapping in a Laser Wakefield Accelerator". In: *Phys. Rev. Lett.* 104 (2 2010), p. 025004. DOI: 10.1103/PhysRevLett.104.025004. URL: https://link.aps.org/doi/10.1103/PhysRevLett.104.025004.

[71] C. J. McKinstrie et al. "Two-dimensional analysis of the power transfer between crossed laser beams". In: *Physics of Plasmas* 3.7 (1996), pp. 2686–2692. DOI: 10.1063/1.871721. eprint: https://doi.org/10.1063/1.871721. URL: https://doi.org/10.1063/1.871721.

[72] C. J. McKinstrie et al. "Two-dimensional stimulated Brillouin scattering". In: *Phys. Rev. E* 50 (3 1994), pp. 2182–2185. DOI: 10.1103/PhysRevE.50.2182. URL: https://link.aps.org/doi/10.1103/PhysRevE.50.2182.

[73] P. Michel et al. "Dynamic Control of the Polarization of Intense Laser Beams via Optical Wave Mixing in Plasmas". In: *Phys. Rev. Lett.* 113 (20 2014), p. 205001. DOI: 10.1103/PhysRevLett.113.205001. URL: https://link.aps.org/doi/10.1103/PhysRevLett.113.205001.

[74] P. Michel et al. "Saturation of multi-laser beams laser-plasma instabilities from stochastic ion heating". In: *Physics of Plasmas* 20.5 (2013), p. 056308. DOI: 10.1063/1.4802828. eprint: https://doi.org/10.1063/1.4802828. URL: https://doi.org/10.1063/1.4802828.

[75] P. Michel et al. "Tuning the Implosion Symmetry of ICF Targets via Controlled Crossed-Beam Energy Transfer". In: *Phys. Rev. Lett.* 102 (2 2009), p. 025004. DOI: 10.1103/PhysRevLett.102.025004. URL: https://link.aps.org/doi/10.1103/PhysRevLett.102.025004.

[76] S. Miyamoto et al. "Simulations of Anomalous Stimulated Raman Backscattering in a Bounded Plasma". In: *Journal of the Physical Society of Japan* 67.4 (1998), pp. 1281–1287. DOI: 10.1143/JPSJ.67.1281. eprint: https://doi.

org/10.1143/JPSJ.67.1281. URL: https://doi.org/10.1143/JPSJ.67.1281.

[77] C. I. Moore et al. "Electron Trapping in Self-Modulated Laser Wakefields by Raman Backscatter". In: *Phys. Rev. Lett.* 79 (20 1997), pp. 3909–3912. DOI: 10.1103/PhysRevLett.79.3909. URL: https://link.aps.org/doi/10.1103/PhysRevLett.79.3909.

[78] Aghapi G. Mordovanakis et al. "Temperature scaling of hot electrons produced by a tightly focused relativistic-intensity laser at 0.5 kHz repetition rate". In: *Applied Physics Letters* 96.7 (2010), p. 071109. DOI: 10.1063/1.3306730. eprint: https://doi.org/10.1063/1.3306730. URL: https://doi.org/10.1063/1.3306730.

[79] C. D. Murphy et al. "Evidence of photon acceleration by laser wake fields". In: *Physics of Plasmas* 13.3 (2006), p. 033108. DOI: 10.1063/1.2178650. eprint: https://doi.org/10.1063/1.2178650. URL: https://doi.org/10.1063/1.2178650.

[80] J. F. Myatt et al. "A wave-based model for cross-beam energy transfer in direct-drive inertial confinement fusion". In: *Physics of Plasmas* 24.5 (2017), p. 056308. DOI: 10.1063/1.4982059. eprint: https://doi.org/10.1063/1.4982059. URL: https://doi.org/10.1063/1.4982059.

[81] N. Naseri, W. Rozmus, and D. Pesme. "Self-channelling of intense laser pulses in underdense plasma and stability analysis". In: *Physics of Plasmas* 23.11 (2016), p. 113101. DOI: 10.1063/1.4966560. eprint: https://doi.org/10.1063/1.4966560. URL: https://doi.org/10.1063/1.4966560.

[82] N. Naseri et al. "Channeling of Relativistic Laser Pulses, Surface Waves, and Electron Acceleration". In: *Phys. Rev. Lett.* 108 (10 2012), p. 105001. DOI: 10.1103/PhysRevLett.108.105001. URL: https://link.aps.org/doi/10.1103/PhysRevLett.108.105001.

[83] Z Nie et al. "Relativistic single-cycle tunable infrared pulses generated from a tailored plasma density structure". In: *Nature Photonics* 12.8 (2018), p. 489. URL: https://doi.org/10.1038/s41566-018-0190-8.

[84] R. Nuter and V. Tikhonchuk. “Prepulse suppression and optimization of backward Raman amplification with a chirped pump laser beam”. In: *Phys. Rev. E* 87 (4 2013), p. 043109. DOI: 10.1103/PhysRevE.87.043109. URL: https://link.aps.org/doi/10.1103/PhysRevE.87.043109.

[85] CH Pai et al. “Generation of intense ultrashort midinfrared pulses by laser-plasma interaction in the bubble regime”. In: *Physical Review A* 82.6 (2010), p. 063804. ISSN: 1050-2947. DOI: 10.1103/PhysRevA.82.063804. URL: https://link.aps.org/doi/10.1103/PhysRevA.82.063804.

[86] J P Palastro et al. “A nonlinear plasma retroreflector for single pulse Compton backscattering”. In: *New Journal of Physics* 17.2 (2015), p. 023072. DOI: 10.1088/1367-2630/17/2/023072. URL: https://doi.org/10.1088%2F1367-2630%2F17%2F2%2F023072.

[87] Y. Ping et al. “Development of a nanosecond-laser-pumped Raman amplifier for short laser pulses in plasma”. In: *Physics of Plasmas* 16.12 (2009), p. 123113. DOI: 10.1063/1.3276739. eprint: https://doi.org/10.1063/1.3276739. URL: https://doi.org/10.1063/1.3276739.

[88] Yuan Ping et al. “Amplification of Ultrashort Laser Pulses by a Resonant Raman Scheme in a Gas-Jet Plasma”. In: *Phys. Rev. Lett.* 92 (17 2004), p. 175007. DOI: 10.1103/PhysRevLett.92.175007. URL: https://link.aps.org/doi/10.1103/PhysRevLett.92.175007.

[89] Tenio Popmintchev et al. “Phase matching of high harmonic generation in the soft and hard X-ray regions of the spectrum”. In: *Proceedings of the National Academy of Sciences* 106.26 (2009), pp. 10516–10521. ISSN: 0027-8424. DOI: 10.1073/pnas.0903748106. eprint: https://www.pnas.org/content/106/26/10516.full.pdf. URL: https://www.pnas.org/content/106/26/10516.

[90] K. I. Popov et al. “Ion Response to Relativistic Electron Bunches in the Blowout Regime of Laser-Plasma Accelerators”. In: *Phys. Rev. Lett.* 105 (19 2010), p. 195002. DOI: 10.1103/PhysRevLett.105.195002. URL: https://link.aps.org/doi/10.1103/PhysRevLett.105.195002.

[91] K. I. Popov et al. "Ion Response to Relativistic Electron Bunches in the Blowout Regime of Laser-Plasma Accelerators". In: *Phys. Rev. Lett.* 105 (19 2010), p. 195002. DOI: 10.1103/PhysRevLett.105.195002. URL: https://link.aps.org/doi/10.1103/PhysRevLett.105.195002.

[92] A. Pukhov and J. Meyer-ter-Vehn. "Laser wake field acceleration: the highly non-linear broken-wave regime". In: *Applied Physics B* 74.4-5 (2002), pp. 355–361. DOI: 10.1007/s003400200795. URL: https://doi.org/10.1007/s003400200795.

[93] C. Riconda et al. "Spectral characteristics of ultra-short laser pulses in plasma amplifiers". In: *Physics of Plasmas* 20.8 (2013), p. 083115. DOI: 10.1063/1.4818893. eprint: https://doi.org/10.1063/1.4818893. URL: https://doi.org/10.1063/1.4818893.

[94] Hans G. Rinderknecht et al. "Highly Resolved Measurements of a Developing Strong Collisional Plasma Shock". In: *Phys. Rev. Lett.* 120 (9 2018), p. 095001. DOI: 10.1103/PhysRevLett.120.095001. URL: https://link.aps.org/doi/10.1103/PhysRevLett.120.095001.

[95] D. V. Romanov et al. "Self-Organization of a Plasma due to 3D Evolution of the Weibel Instability". In: *Phys. Rev. Lett.* 93 (21 2004), p. 215004. DOI: 10.1103/PhysRevLett.93.215004. URL: https://link.aps.org/doi/10.1103/PhysRevLett.93.215004.

[96] Harvey A. Rose. "Laser beam deflection by flow and nonlinear self-focusing". In: *Physics of Plasmas* 3.5 (1996), pp. 1709–1727. DOI: 10.1063/1.871690. eprint: https://doi.org/10.1063/1.871690. URL: https://doi.org/10.1063/1.871690.

[97] Harvey A. Rose and L. Yin. "Langmuir wave filamentation instability". In: *Physics of Plasmas* 15.4 (2008), p. 042311. DOI: 10.1063/1.2901197. eprint: https://aip.scitation.org/doi/pdf/10.1063/1.2901197. URL: https://aip.scitation.org/doi/abs/10.1063/1.2901197.

[98] J. S. Ross et al. "Collisionless Coupling of Ion and Electron Temperatures in Counterstreaming Plasma Flows". In: *Phys. Rev. Lett.* 110 (14 2013), p. 145005.

DOI: 10.1103/PhysRevLett.110.145005. URL: https://link.aps.org/doi/10.1103/PhysRevLett.110.145005.

[99] Antoine Rousse et al. "Production of a keV X-Ray Beam from Synchrotron Radiation in Relativistic Laser-Plasma Interaction". In: *Phys. Rev. Lett.* 93 (13 2004), p. 135005. DOI: 10.1103/PhysRevLett.93.135005. URL: https://link.aps.org/doi/10.1103/PhysRevLett.93.135005.

[100] Antoine Rousse et al. "Production of a keV X-Ray Beam from Synchrotron Radiation in Relativistic Laser-Plasma Interaction". In: *Phys. Rev. Lett.* 93 (13 2004), p. 135005. DOI: 10.1103/PhysRevLett.93.135005. URL: https://link.aps.org/doi/10.1103/PhysRevLett.93.135005.

[101] James D. Sadler et al. "Optimization of plasma amplifiers". In: *Phys. Rev. E* 95 (5 2017), p. 053211. DOI: 10.1103/PhysRevE.95.053211. URL: https://link.aps.org/doi/10.1103/PhysRevE.95.053211.

[102] B. A. Shadwick, C. B. Schroeder, and E. Esarey. "Nonlinear laser energy depletion in laser-plasma accelerators". In: *Physics of Plasmas* 16.5 (2009), p. 056704. DOI: 10.1063/1.3124185. eprint: https://doi.org/10.1063/1.3124185. URL: https://doi.org/10.1063/1.3124185.

[103] B. A. Shadwick, C. B. Schroeder, and E. Esarey. "Nonlinear laser energy depletion in laser-plasma accelerators". In: *Physics of Plasmas* 16.5 (2009), p. 056704. DOI: 10.1063/1.3124185. eprint: https://doi.org/10.1063/1.3124185. URL: https://doi.org/10.1063/1.3124185.

[104] B. H. Shaw et al. "Reflectance characterization of tape-based plasma mirrors". In: *Physics of Plasmas* 23.6 (2016), p. 063118. DOI: 10.1063/1.4954242. eprint: https://doi.org/10.1063/1.4954242. URL: https://doi.org/10.1063/1.4954242.

[105] G. Shvets et al. "Superradiant Amplification of an Ultrashort Laser Pulse in a Plasma by a Counterpropagating Pump". In: *Phys. Rev. Lett.* 81 (22 1998), pp. 4879–4882. DOI: 10.1103/PhysRevLett.81.4879. URL: https://link.aps.org/doi/10.1103/PhysRevLett.81.4879.

[106] S. Skupsky et al. "Improved laser-beam uniformity using the angular dispersion of frequency-modulated light". In: *Journal of Applied Physics* 66.8 (1989), pp. 3456–3462. DOI: 10.1063/1.344101. eprint: https://doi.org/10.1063/1.344101. URL: https://doi.org/10.1063/1.344101.

[107] P. Sprangle, E. Esarey, and A. Ting. "Nonlinear interaction of intense laser pulses in plasmas". In: *Phys. Rev. A* 41 (8 1990), pp. 4463–4469. DOI: 10.1103/PhysRevA.41.4463. URL: https://link.aps.org/doi/10.1103/PhysRevA.41.4463.

[108] P. Sprangle, E. Esarey, and A. Ting. "Nonlinear theory of intense laser-plasma interactions". In: *Phys. Rev. Lett.* 64 (17 1990), pp. 2011–2014. DOI: 10.1103/PhysRevLett.64.2011. URL: https://link.aps.org/doi/10.1103/PhysRevLett.64.2011.

[109] P. Sprangle et al. "Laser wakefield acceleration and relativistic optical guiding". In: *Applied Physics Letters* 53.22 (1988), pp. 2146–2148. DOI: 10.1063/1.100300. eprint: https://doi.org/10.1063/1.100300. URL: https://doi.org/10.1063/1.100300.

[110] P. Sprangle et al. "Propagation and guiding of intense laser pulses in plasmas". In: *Phys. Rev. Lett.* 69 (15 1992), pp. 2200–2203. DOI: 10.1103/PhysRevLett.69.2200. URL: https://link.aps.org/doi/10.1103/PhysRevLett.69.2200.

[111] S. Steinke et al. "Multistage coupling of independent laser-plasma accelerators". In: *Nature* 530 (2016), 190?193. URL: https://doi.org/10.1038/nature16525.

[112] C. H. Still et al. "Filamentation and forward Brillouin scatter of entire smoothed and aberrated laser beams". In: *Physics of Plasmas* 7.5 (2000), pp. 2023–2032. DOI: 10.1063/1.874055. eprint: https://doi.org/10.1063/1.874055. URL: https://doi.org/10.1063/1.874055.

[113] M. J. V. Streeter et al. "Observation of Laser Power Amplification in a Self-Injecting Laser Wakefield Accelerator". In: *Phys. Rev. Lett.* 120 (25 2018), p. 254801. DOI: 10.1103/PhysRevLett.120.254801. URL: https://link.aps.org/doi/10.1103/PhysRevLett.120.254801.

[114] T. Tajima and J. M. Dawson. "Laser Electron Accelerator". In: *Phys. Rev. Lett.* 43 (4 1979), pp. 267–270. DOI: 10.1103/PhysRevLett.43.267. URL: https://link.aps.org/doi/10.1103/PhysRevLett.43.267.

[115] T Tajima and JM Dawson. "Laser Electron Accelerator". In: *Physical Review Letters* 43.4 (1979), pp. 267–270. ISSN: 0031-9007. DOI: 10.1103/PhysRevLett.43.267. URL: https://link.aps.org/doi/10.1103/PhysRevLett.43.267.

[116] A. Ting et al. "Backscattered supercontinuum emission from high-intensity laser–plasma interactions". In: *Opt. Lett.* 21.15 (1996), pp. 1096–1098. DOI: 10.1364/OL.21.001096. URL: http://ol.osa.org/abstract.cfm?URI=ol-21-15-1096.

[117] R M G M Trines et al. "Photon acceleration and modulational instability during wakefield excitation using long laser pulses". In: *Plasma Physics and Controlled Fusion* 51.2 (2009), p. 024008. DOI: 10.1088/0741-3335/51/2/024008. URL: https://doi.org/10.1088%2F0741-3335%2F51%2F2%2F024008.

[118] FS Tsung et al. "Generation of ultra-intense single-cycle laser pulses by using photon deceleration." In: *Proceedings of the National Academy of Sciences of the United States of America* 99.1 (2002), pp. 29–32. ISSN: 0027-8424. DOI: 10.1073/pnas.262543899. URL: http://www.ncbi.nlm.nih.gov/pubmed/11752414http://www.pubmedcentral.nih.gov/articlerender.fcgi?artid=PMC117508.

[119] D. Turnbull et al. "Possible origins of a time-resolved frequency shift in Raman plasma amplifiers". In: *Physics of Plasmas* 19.7 (2012), p. 073103. DOI: 10.1063/1.4736856. eprint: https://doi.org/10.1063/1.4736856. URL: https://doi.org/10.1063/1.4736856.

[120] D. Turnbull et al. "Raman Amplification with a Flying Focus". In: *Phys. Rev. Lett.* 120 (2 2018), p. 024801. DOI: 10.1103/PhysRevLett.120.024801. URL: https://link.aps.org/doi/10.1103/PhysRevLett.120.024801.

[121] D. Turnbull et al. "Refractive Index Seen by a Probe Beam Interacting with a Laser-Plasma System". In: *Phys. Rev. Lett.* 118 (1 2017), p. 015001. DOI: 10.1103/PhysRevLett.118.015001. URL: https://link.aps.org/doi/10.1103/PhysRevLett.118.015001.

[122] G. Vieux et al. “An ultra-high gain and efficient amplifier based on Raman amplification in plasma”. In: *Scientific reports* 1.7 (2017), p. 2399. URL: https://doi.org/10.1038/s41598-017-01783-4.

[123] G Vieux et al. “Chirped pulse Raman amplification in plasma”. In: *New Journal of Physics* 13.6 (2011), p. 063042. DOI: 10.1088/1367-2630/13/6/063042. URL: https://doi.org/10.1088%2F1367-2630%2F13%2F6%2F063042.

[124] M. M. Škorić, M. S. Jovanović, and M.R. Rajković. “Anomalous spectral signatures of high-intensity stimulated Raman backscattering”. In: *AIP Conference Proceedings* 369.1 (1996), pp. 363–368. DOI: 10.1063/1.50455. eprint: https://aip.scitation.org/doi/pdf/10.1063/1.50455. URL: https://aip.scitation.org/doi/abs/10.1063/1.50455.

[125] M.M. Škorić, L. Nikolić, and S. Ishiguro. “Self-organization and control in stimulated Raman backscattering”. In: *Journal of Plasma Physics* 79.6 (2013), 1003?1006. DOI: 10.1017/S0022377813001189.

[126] François Walraet, Guy Bonnaud, and Gilles Riazuelo. “Velocities of speckles in a smoothed laser beam propagating in a plasma”. In: *Physics of Plasmas* 8.11 (2001), pp. 4717–4720. DOI: 10.1063/1.1405128. eprint: https://doi.org/10.1063/1.1405128. URL: https://doi.org/10.1063/1.1405128.

[127] B. R. Walton et al. “Measurements of forward scattered laser radiation from intense sub-ps laser interactions with underdense plasmas”. In: *Physics of Plasmas* 13.11 (2006), p. 113103. DOI: 10.1063/1.2363170. eprint: https://doi.org/10.1063/1.2363170. URL: https://doi.org/10.1063/1.2363170.

[128] T.-L. Wang et al. “Feasibility study for using an extended three-wave model to simulate plasma-based backward Raman amplification in one spatial dimension”. In: *Physics of Plasmas* 16.12 (2009), p. 123110. DOI: 10.1063/1.3280012. eprint: https://doi.org/10.1063/1.3280012. URL: https://doi.org/10.1063/1.3280012.

[129] T.-L. Wang et al. “Particle-in-cell simulations of kinetic effects in plasma-based backward Raman amplification in underdense plasmas”. In: *Physics of Plasmas* 17.2 (2010), p. 023109. DOI: 10.1063/1.3298738. eprint: https://doi.org/10.1063/1.3298738. URL: https://doi.org/10.1063/1.3298738.

[130] X. Wang et al. "Quasi-monoenergetic laser-plasma acceleration of electrons to 2 GeV". In: *Nature Communications* 4.1988 (2013). URL: https://doi.org/10.1038/ncomms2988.

[131] S. C. Wilks et al. "Photon accelerator". In: *Phys. Rev. Lett.* 62 (22 1989), pp. 2600–2603. DOI: 10.1103/PhysRevLett.62.2600. URL: https://link.aps.org/doi/10.1103/PhysRevLett.62.2600.

[132] S. C. Wilks et al. "Stimulated Raman backscatter in ultraintense, short pulse laser-plasma interactions". In: *Physics of Plasmas* 2.1 (1995), pp. 274–279. DOI: 10.1063/1.871097. eprint: https://doi.org/10.1063/1.871097. URL: https://doi.org/10.1063/1.871097.

[133] D. Woodbury et al. "Laser wakefield acceleration with mid-IR laser pulses". In: *Opt. Lett.* 43.5 (2018), pp. 1131–1134. DOI: 10.1364/OL.43.001131. URL: http://ol.osa.org/abstract.cfm?URI=ol-43-5-1131.

[134] X. Yang et al. "Chirped pulse Raman amplification in warm plasma: towards controlling saturation". In: *Nature Scientific Reports* 5.13333 (2015). URL: https://doi.org/10.1038/srep13333.

[135] Xi Zhang, Vladimir N. Khudik, and Gennady Shvets. "Synergistic Laser-Wakefield and Direct-Laser Acceleration in the Plasma-Bubble Regime". In: *Phys. Rev. Lett.* 114 (18 2015), p. 184801. DOI: 10.1103/PhysRevLett.114.184801. URL: https://link.aps.org/doi/10.1103/PhysRevLett.114.184801.

[136] W Zhu, JP Palastro, and TM Antonsen. "Pulsed mid-infrared radiation from spectral broadening in laser wakefield simulations". In: *Physics of Plasmas* 20.7 (2013), p. 073103. ISSN: 1070664X. DOI: 10.1063/1.4813245. URL: http://aip.scitation.org/doi/10.1063/1.4813245.

Appendix A

Numerical Methods

A.1 Introduction

This Appendix gives an overview of some numerical techniques developed in the course of this PhD research. The techniques were used to gain further insight into codes and the methods of solving certain types of problems. First a numerical approach to hydrodynamics for the purpose of plasma simulation is presented in sec. A.2. Numerical approaches to optics for laser simulation are shown in sec. A.3. Finally numerical approaches to ray tracing are compared for visualizing datasets and more complex scenes in sec. A.4.

A.2 Plasma Simulation via Hydrodynamics

Hydrodynamic simulations have the advantage of being a fast method of simulating plasmas when compared with kinetic simulations such as PIC or Vlasov simulations. A disadvantage of the hydrodynamic approach is that it misses kinetic effects which can become important for high intensity lasers, energetic plasmas, and fast particles. In this thesis PIC is used when studying short pulse lasers and particle accelerators, while hydrodynamic methods are used when considering large scale, non-relativistic laser-plasma interactions.

The Navier-Stokes equations (see Ch. 5 Eq. 5.36) are the core of hydrodynamic modeling. In the chapters of this thesis, well established hydrodynamics codes were used, however a straightforward numerical example is given here. The Navier-Stokes equations may be broken down into the explicit second order finite differences in 2D as follows.

Conservation of mass:

$$\rho_{i,j}^{n+1} = \rho_{i,j}^{n-1} - \Delta t\big(\tfrac{\rho_{i+1,j}^{n}-\rho_{i-1,j}^{n}}{\Delta x}v_{x,i,j}^{n} + \tfrac{v_{x,i+1,j}^{n}-v_{x,i-1,j}^{n}}{\Delta x}\rho_{i,j}^{n}$$

$$+ \frac{\rho_{i,j+1}^{n} - \rho_{i,j-1}^{n}}{\Delta y}v_{y,i,j}^{n} + \frac{v_{y,i,j+1}^{n} - v_{y,i,j-1}^{n}}{\Delta y}\rho_{i,j}^{n}\big) \tag{A.1}$$

Conservation of momentum: for the x-component:

$$v_{x,i,j}^{n+1} = v_{x,i,j}^{n-1} + \big[-(\rho_{i,j}^{n+1} - \rho_{i,j}^{n-1})v_{x,i,j}^{n} - \Delta t\big(\tfrac{\rho_{i+1,j}^{n}-\rho_{i-1,j}^{n}}{\Delta x}v_{x,i,j}^{n}v_{x,i,j}^{n} + 2v_{x,i,j}^{n}\tfrac{v_{x,i+1,j}^{n}-v_{x,i-1,j}^{n}}{\Delta x}\rho_{i,j}^{n} +$$

$$\tfrac{\rho_{i,j+1}^{n}-\rho_{i,j-1}^{n}}{\Delta y}v_{x,i,j}^{n}v_{y,i,j}^{n} + \rho_{i,j}^{n}\big(\tfrac{v_{x,i,j+1}^{n}-v_{x,i,j-1}^{n}}{\Delta y}v_{y,i,j}^{n} + \tfrac{v_{y,i,j+1}^{n}-v_{y,i,j-1}^{n}}{\Delta y}v_{x,i,j}^{n}\big) +$$

$$\frac{P_{i+1,j}^{n} - P_{i-1,j}^{n}}{\Delta x} - 2F_{x,i,j}\big)\big]\big(\frac{1}{1+\rho_{i,j}^{n}}\big) \tag{A.2}$$

The same method my be repeated to obtain equation for the y-component. Here the force $\vec{F}_{i,j}^{n} = [F_{x,i,j}^{n}, F_{y,i,j}^{n}]$ is a body force, and may include the ponderomotive force $\vec{F}_p \propto -\vec{\nabla} I$ of a laser. The equation of state is $P = \rho k_b T$, which determines the sound speed $c_s^2 = \frac{\partial P}{\partial \rho}$, this second order finite difference does not allow for supersonic velocities. Adding the 3rd dimension via this method is trivial, but requires a factor of N_Z more resources (memory, compute time) to solve, where N_Z is the number of grid points in the third spatial dimension. This algorithm is well suited for optimization, $1/\Delta x$ should be precomputed or the equations normalized so that it is unnecessary. A stencil may also be used in shared memory groups with guard cells to give access to faster memory. This algorithm is also embarrassingly parallel. An RTX 2080 can achieve about 500fps @ 8192x8192 resolution solving for all the variables above while taking the gradient of a paraxial laser field, when a Fourier transform of the velocity is taken to include damping, the frame-rate is reduced to 200fps. The numerical stencil includes the Von Neumann neighborhood in space-time, so causality is restricted by the CFL condition, $v_x\Delta t/\Delta x + v_y \Delta t/\Delta y < 1$ in 2D. An example of this algorithm with a laser focus ponderomotive force is shown in figure A.1.

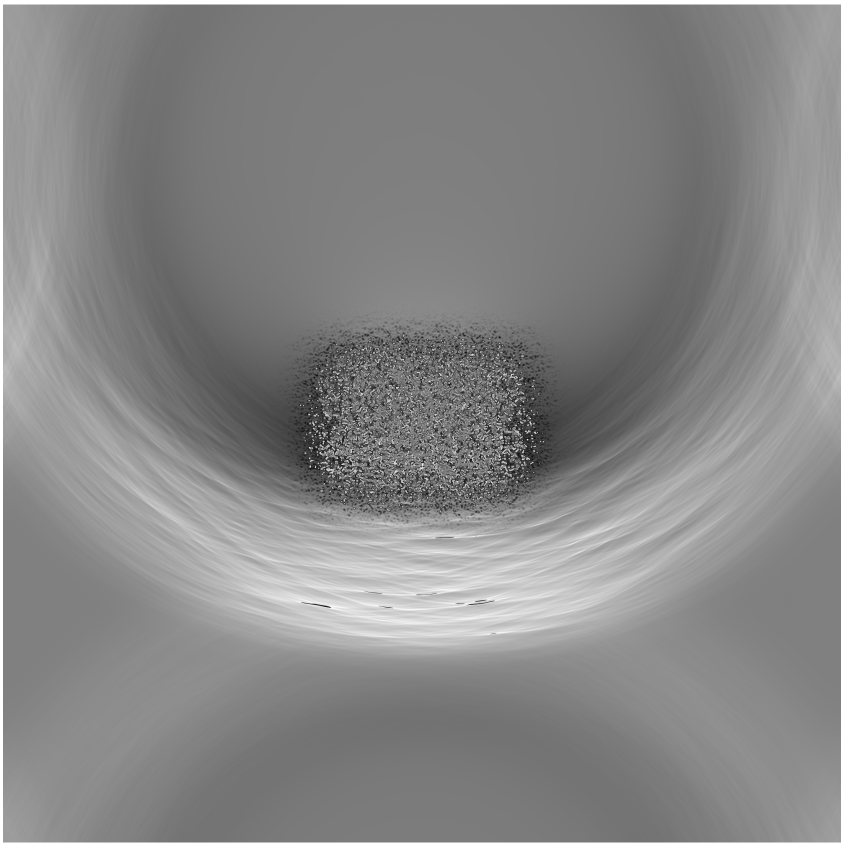

FIGURE A.1: Saturated grayscale image of fluid density in response to the ponderomotive force of a paraxial laser. There is a sub-sonic flow in the upward direction, and periodic boundary conditions.

A.3 Fourier Optics and the Paraxial Approximation

Fourier Optics

Fourier optics is a powerful technique for making realistic laser focal spots given an electric field on a lens. Starting with the amplitude and phase on the lens, a 2D Fourier transform gives the amplitude and phase at the focal spot. Effectively any focal spot intensity pattern can be obtained by setting the light incident to the lens to be its Fourier inverse. Equation A.3 shows this relation mathematically assuming the laser is traveling along the z-direction and is focused to z=0. The primed quantities represent the focal coordinates, f is the focal length, and λ is the laser wavelength.

$$E_{focus(x',y',0)} = \int_{-\infty}^{\infty}\int_{-\infty}^{\infty} E_{lens(x,y,-f)} e^{-2\pi i \frac{xx'+yy'}{\lambda f}} dxdy \tag{A.3}$$

Here $E_{(x,y,z)}$ is the complex electric field envelope in time with arbitrary polarization in the x-y plane. Because the field is a complex number containing both the amplitude and phase, effects of spatially or temporally dependent phases can be taken into account. Random Phase Plates (RPP) or Continuous Phase Plates (CPP) are common optical elements used to control the focal spot intensity pattern of a laser. The smaller the phase elements the bigger the focal spot, and the smaller the aperture is the larger the focal speckles are. A RPP can be easily implemented numerically as spatially dependent phase shifts to the electric field on the lens: $E_{(x,y)} \rightarrow E_{(x,y)}e^{i\phi_{(x,y)}}$, where $\phi_{(x,y)}$ is the spatially dependent phase shift. Numerically $\phi_{(x,y)}$ becomes $\phi_{(x[i],y[j])}$ and will have finite grid spacing, so constant size elements are necessarily an integer multiple of the grid spacing. While this can result in some limitations, it is convenient that two grid points per square RPP element results in a spatially resolved focal spot, and one grid point per square RPP element fills the focal grid regardless of the normalization. Figure A.2 show the effect of interfering phase elements to produce a speckled laser focus.

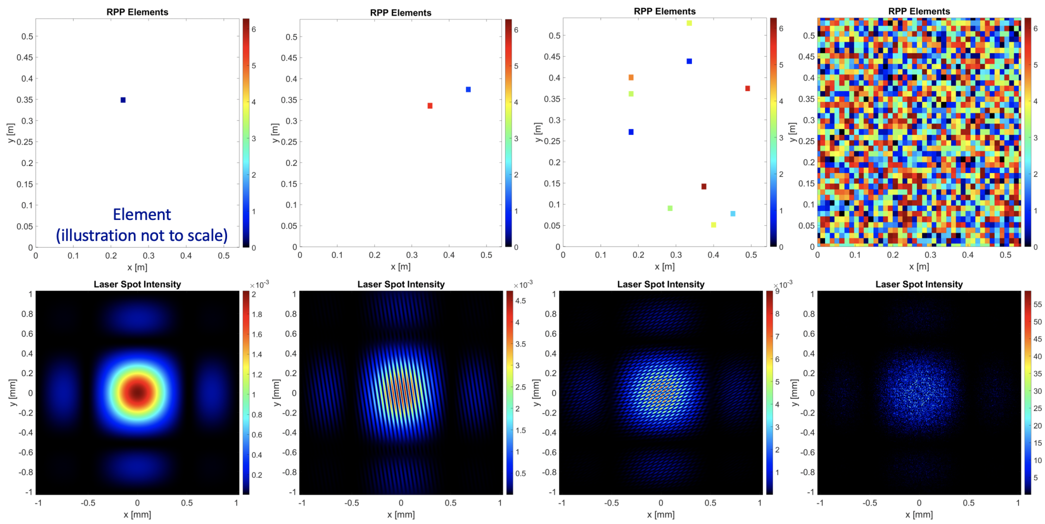

FIGURE A.2: Effects of Random Phase Plate elements. Each phase element of an RPP focuses to its diffraction limited spot, but the difference in phases causes interference so that a speckle pattern in the laser focus emerges.

Note that square phase elements produce a $sinc^2$ focal spot intensity profile as the Fourier transform of a boxcar is a $sinc$ function. To create arbitrary focal spot profiles one may simply use the inverse Fourier transform. Often beams are chosen to have a Gaussian or Super Gaussian focal spot. One may create such a profile with speckles by starting with a large focal spot and using a filter in the Fourier domain.

Laser Light Propagation in the Paraxial Approximation

The paraxial approximation is an approximation to Maxwell's equations which assumes that the light is traveling primarily along an axis, $k_{\parallel} \gg k_{\perp}$, where the light has a central wavenumber of $\vec{k}$. For lasers the paraxial approximation is generally very good, but can become inaccurate for small f-numbers ($f < 2$). An advantage of the paraxial approximation is that it is much faster than solving the full Maxwell equations, and the paraxial approximation includes fine scale structure (speckles and beat waves) which is typically neglected in other methods such as Ray Tracing. Assuming that a laser is traveling along the z-axis and $\sin\theta \approx \theta$ for angles away from the z-axis. The complex envelope of the laser field at a distance z from the focal point can be approximated by:

$$\mathcal{F}[E_{(x,y,z)}] = \mathcal{F}[E_{(x,y,0)}]e^{i\frac{k_{\perp}^2}{2k_{\parallel}}z} \tag{A.4}$$

Where $\mathcal{F}$ denotes the 2D Fourier transform. Here the laser field $E_{(x,y,z)}$ is the complex amplitude enveloped over its frequency/wavenumber, with arbitrary polarization in the x-y plane. An expression for the full electric field may be obtained simply by multiplying by $e^{i(\vec{k}\cdot\vec{(}x)-\omega t)}$.

The effects of additional optical components such as a grating or echelon are easily added to the model through the use of spatially and/or temporally varying phases. An example of paraxial propagation is shown in figure A.3. In this example the lasers start as two separate beams on one lens, a Fourier transform gives the focal spot. When starting from the lens the effect of paraxial propogation A.4, may simply be applied as $E_{(x,y,0)}e^{i\frac{k_{\perp}^2}{2k_{\parallel}}z}$ on the lens before Fourier transforming to avoid transforming back and forth again. Note that by having both beams on one lens, the full complex field is already on the same grid so that proper beat waves can be observed where the beams overlap.

Smoothing by Spectral Dispersion

To focus a laser to its diffraction limited spot the laser field incident to the optics must have a uniform phase front. Laser speckles or "hotspots" are caused by (usually unwanted) phase alterations at the optics. In inertial confinement fusion, high intensity

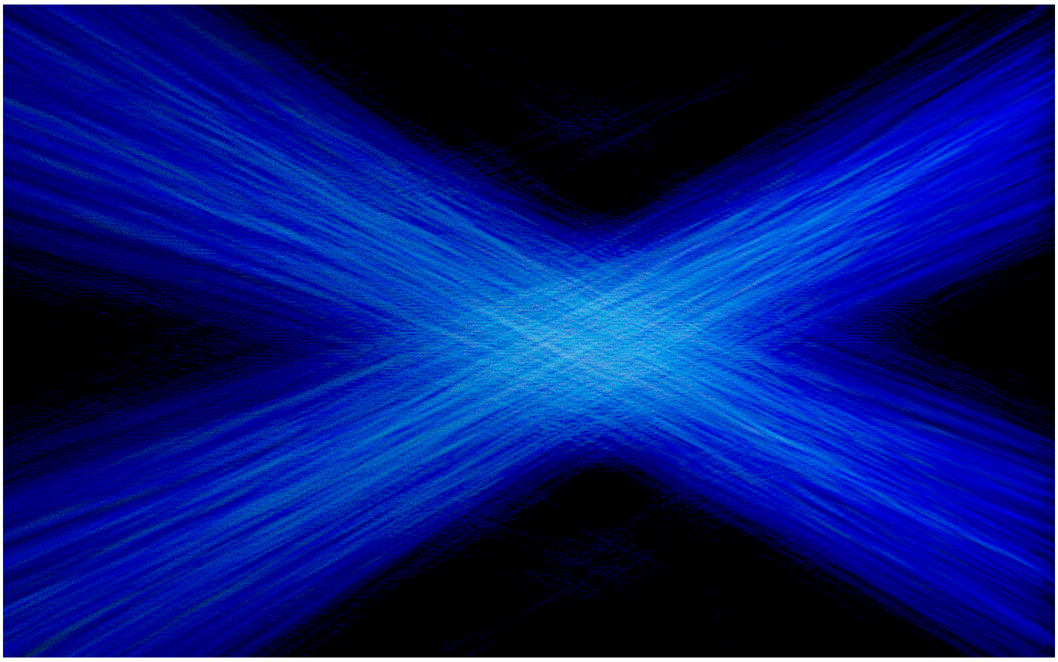

FIGURE A.3: An example of using Fourier optics and the paraxial approximation to create two 3D crossing laser beams with RPPs. The absolute value of the electric field is shown from blue (low) to red (high). Note that a beat ($\vec{k}_{beat} = \vec{k}_1 - \vec{k}_2$) wave can be seen in the laser field due to the crossing beams.

laser speckles may result in hydrodynamic instabilities that degrade implosion symmetry, or may seed laser plasma instabilities such as Raman or Brillouin scattering. Smoothing by Spectral Dispersion or SSD, is a method of using bandwidth in combination with a grating to produce speckle movement. This method was originally proposed [106] for temporally smoothing laser focal spots. As speckle movement becomes fast on the timescale of instabilities the effect of the hot spots in laser intensity become insignificant. The bandwidth itself used in SSD also helps to mitigate resonance with instabilities. A schematic of the SSD configuration is shown below in Figure A.4.

Assuming there is some bandwidth in the laser light with central wavelength λ_0, the angle of diffraction from the grating is easily calculated from the grating's angular dispersion $d\theta/d\lambda$:

$$\theta_{(\lambda)} = \frac{d\theta}{d\lambda}(\lambda_{(y)} - \lambda_0) \tag{A.5}$$

The desired number of color cycles gives a constraint on the grating's angular dispersion:

$$\frac{d\theta}{d\lambda} = \frac{N_c}{w_0}\frac{\omega_0}{\omega_m} \tag{A.6}$$

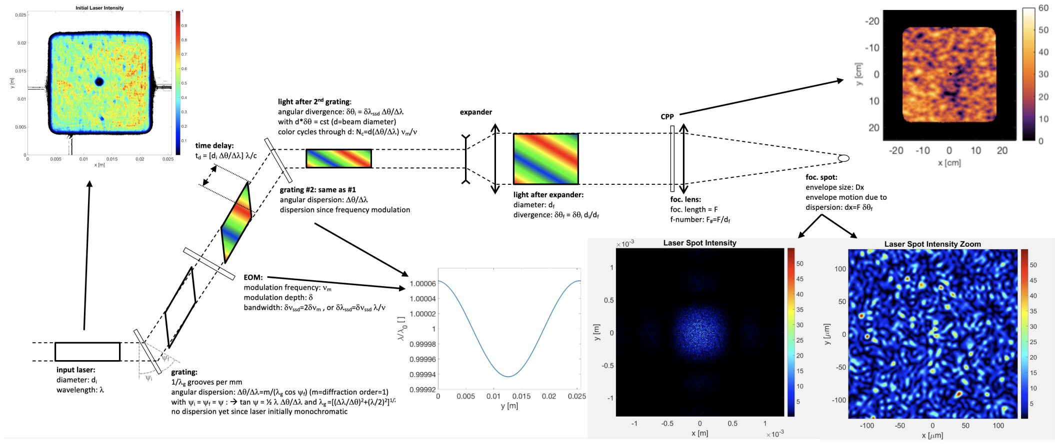

FIGURE A.4: A schematic for the implementation of SSD. The laser starts in a fiber and is passed through an EOM to gain bandwidth. The laser then undergoes expansion and amplification, afterwords it is tilted by a grating to introduce a shear delay in the pulse. The shear delay results in transverse color cycles across the pulse, so that all the bandwidth is incident to the lens at the same time.

Where N_c is the number of color cycles (typically 1), w_0 is the width of the beam incident on the grating, ω_0 is the central angular frequency of the laser, and ω_m is the modulation frequency. Numerical implementation simply requires a wavelength dependent phase shift in the electric field at the lens:

$$E_{(y_n)} \rightarrow E_{(y_n)} e^{ik \sin\theta_{(\lambda_n)} y_n} \tag{A.7}$$

Results of this method are consistent with speckle velocity theory [126]. At the laser focus the speckles have sinusoidal motion along the direction of SSD (y-direction) in time as shown in figure 5.2, in the x-y plane of the focus the spot appears to roll into the z-direction. Adding more bandwidth results in spreading of the focal spot along the direction of SSD as shown in figure A.5.

Non-Paraxial Geometry

While the paraxial approximation may be a powerful tool, it is limited to small deviations in beam propagation along the paraxial axis. Modern laser facilities and experiments often involve the use of more than one laser traveling in more than one direction. Assuming individual lasers do not deviate from their axis too much, one method of overcoming the paraxial limitation for multiple lasers is to assign each laser its own paraxial axis. The lasers are each paraxially propagated along

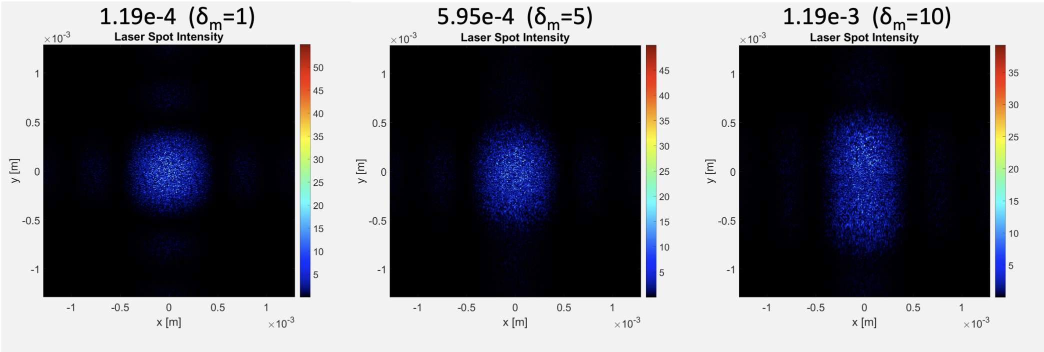

FIGURE A.5: SSD laser focus intensity vs bandwidth for an EOM with $\omega_m = 17GHz$ and varying modulation depth δ_m.

their own axis with the total field being interpolated to the master grid where the plasma's dynamics are solved by hydrodynamics/PIC/etc. An example of using the paraxial approximation in Non-Paraxial Geometry is shown in figures A.6 and A.14. In figure A.6, the full complex field of the lasers is interpolated to include phenomena such as the beat waves, which result in fine speckles. In figure A.14, only the intensity of the lasers is interpolated so that there is no beat waves.

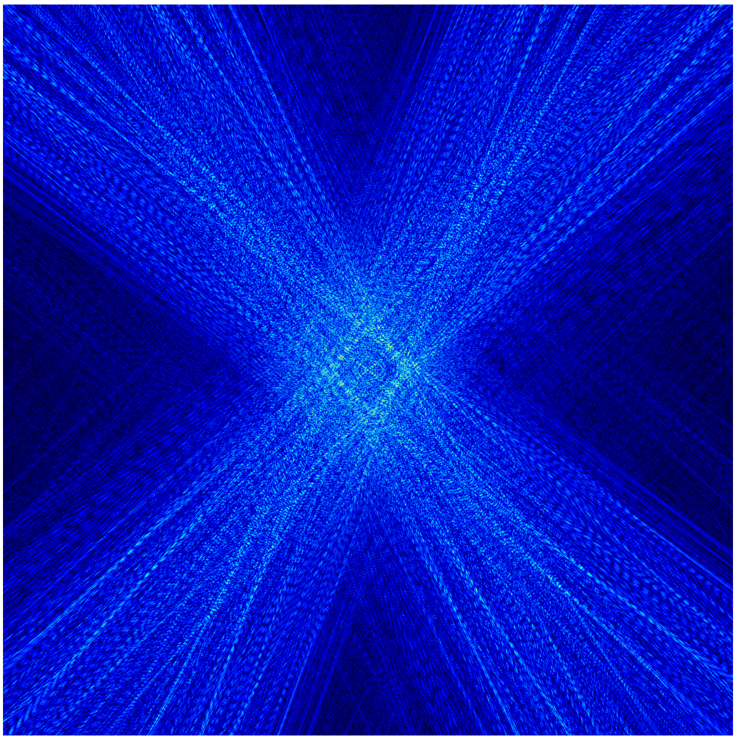

FIGURE A.6: An example of Non-Paraxial Geometry. The absolute value of the electric field is plotted from blue (low) to red (high). Here each of the lasers is propagated along its own paraxial axis (with SSD and RPP) in 2D and interpolated to the master grid where the plasma was simulated using a hydrodynamic model. The laser crossing angles corresponded to the inner and outer NIF beams.

A.4 Ray Tracing

Ray Tracing is a very quick method for simulating light by treating light as geometric rays. Ray Tracing is an effective method for creating high quality rendering and has hardware implementations in many modern graphics cards. A disadvantage of Ray Tracing compared to Maxwell's equations or the paraxial approximation is that it misses fine scale structure (speckles) and misses wave phenomena (beat waves, tunneling) unless directly modeled.

While ray tracing can be a powerful laser plasma simulation method [12], this section focus on ray tracing as a rendering technique. The implementation of ray tracing for rendering or laser plasma simulation is very similar apart from one subtle difference. During laser plasma interactions, individual rays of light may interact with each other (ex: CBET), while in rendering this is almost never the case. When rays do not interact ray tracing is embarrassingly parallel, but interaction of rays requires more sophisticated programing for efficient parallelism. Ray tracing as a rendering technique is ideal for execution on GPUs (Graphics Processing Units), and modern GPUs are designed specifically for ray tracing.

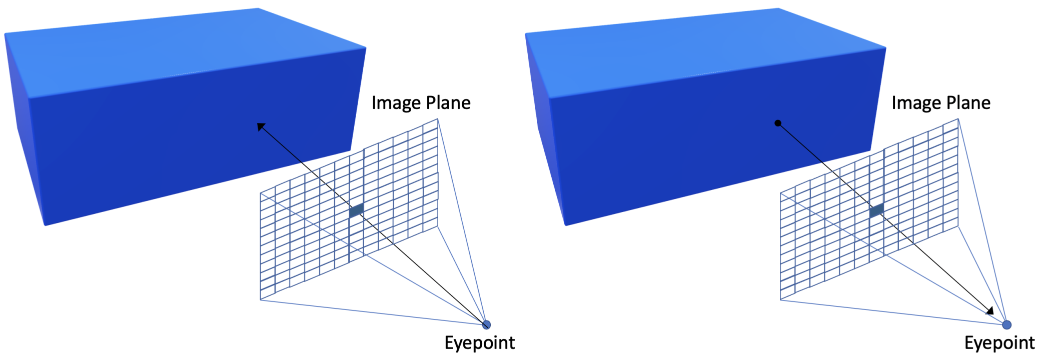

FIGURE A.7: An example of Reverse (left) and Forward (right) ray tracing. In reverse ray tracing the rays originate from the eye-point and are pointed through the center of each pixel. In forward ray tracing the rays originate from the object and are pointed to the eye-point.

The two major methods of initializing rays in a rendering environment are "Forward" and "Reverse" ray tracing. Forward ray tracing involves casting rays directly from their source (ex: light bulb), this method has the advantage of simplicity especially for global illumination, but may be wasteful since time may be spent calculating ray trajectories that never reach the camera. Reverse ray tracing involves casting rays backward from the camera, this method guarantees that all simulated rays are recorded by the camera, but requires the programmer to work backwards. In general it is better to use forward ray tracing when there are only one or few objects, when the number of objects becomes large it is much more practical to use reverse ray tracing.

Figures 4.1 and A.3 were generated using forward ray tracing. These figures are a good example of where this approach can be more effective. Because there is exactly one object in the environment and (almost) the entire object can be seen by the camera, it is more efficient to originate the rays from the object than from the camera. Figures A.13, and A.14 were generated using reverse ray tracing. Due to the complexity of the environment and the large number of objects, forward raytracing would be impractical.

Camera and Rays

The camera is the most fundamental object for a ray tracing program, in its simplest form, its structure contains the coordinates of the camera and the direction it is facing. The camera has an eye point and an image plane A.7, rays pass through both the eye point and pixels in the image plane to produce an image. An example of the IMAGEPLANE, CAMERA, and RAY classes can be seen in Figures A.8, A.9, and A.10 respectively.

```
class IMAGEPLANE
{
public:
    float x[2] = { -16 / 9,16 / 9 }; // bounding box
    float y[2] = { -1,1 };
    float z[2] = { 1,1 };
    unsigned long nx, ny;            // pixel counts
    float dx, dy;                    // pixel widths
    float *image;                    // image array
    float *X, *Y, *Z;                // pixel locations
};
```

FIGURE A.8: An example of the IMAGEPLANE class.

```
class CAMERA
{
public:
    bool record = false;    // save images
    float o[3] = { 0,0,0 }; // location
    float d[3] = { 0,0,1 }; // pointing direction
    long NX;                // gridpoints along horizontal direction
    long NY;                // gridpoints along vertical direction
    IMAGEPLANE imageplane;  // IMAGEPLANE
};
```

FIGURE A.9: An example of the CAMERA class.

```
class RAY {
public:
    float ox, oy, oz; // location
    float dx, dy, dz; // pointing direction
    float Ir, Ig, Ib; // rgb intensity
    int n;            // ray number
    bool stop;        // is the ray in action
    float a0;         // amplitude
};
```

FIGURE A.10: An example of the RAY class. A rays structure contains the coordinates of the ray ($\vec{o}$), the direction it is pointing ($\vec{d}$), its RGB light intensity ($\vec{i}$) and other optional features. The binary "stop" feature is a cheep and effective way to avoid tracing rays which have terminated.

In reverse ray tracing, rays originate from the eye point and point to each of the pixels on the image plane.

$$ray[i].\vec{o} = camera.\vec{o} \tag{A.8}$$

$$ray[i].\vec{d} = camera.imageplane.\vec{O}[i] - ray.\vec{o} \tag{A.9}$$

Here, i represents the ray or pixel number in linear memory ($i = nx * camera.imageplane.ny + ny$ with $nx = 1$ to $camera.imageplane.nx$, $ny = 1$ to $camera.imageplane.ny$ in steps of 1) which can be vectorized to take advantage of parallel processing methods such as a CUDA kernel, openMP parallelization, or SIMD operations. $camera.imageplane.\vec{O}[i]$ represents the X,Y,Z matrices containing the locations of the image plane grid points.

In forward ray tracing, rays originate from the light sources and can be traced directly to the pixels on the image plane as below:

$$ray[i].\vec{o} = volume.\vec{o}[i] \tag{A.10}$$

$$ray[i].\vec{d} = camera.\vec{o} - ray.\vec{o} \tag{A.11}$$

Here $volume.\vec{o}[i]$ is size $NV \equiv volume.NX \times volume.NY \times volume.NZ$ and represents the the grid points of the volume contains data. In this method NV rays are also generated and pointed at the camera's eye point. The rays are then collected on the image plane via a multi-dimensional histogram. Note if the volume data has uniform spacing there can be significant aliasing effects which can be easily remedied by randomizing the data points locations within the grid spacing.

Primitive Objects

Primitive objects include any objects that can be used to construct more complicated objects, but in general are simple to test ray-object intersections. For example a plane is easy to test for intersections and 6 planes may be used to build a cube. Common primitive objects include: triangles, planes, spheres, cones, etc. In this section I will demonstrate how a hit test may be preformed for a plane. Such planes may be placed in a Bounding Volume (sec. A.4) to construct large objects with fewer hit tests.

To define a plane one needs to specify a point and vector within the plane or provide equivalent information. For convenience one typically defines classes for primitive objects, a plane's class may look like the following:

```
class PLANE {
public:
    float x0, xf, y0, yf, z0, zf;     // bounding box
    float Ir, Ig, Ib;                 // rgb intensity (no texture)
    float I = 1.0f;                   // intensity modifier [0-1]
    int n = 0;                        // world position
    float *texture;                   // pointer to texture
    int nx = 1;                       // texture dimensions
    int ny = 1;
    float n_x = 0;                    // normal directions
    float n_y = 0;
    float n_z = -1;
    float Rr = 0;                     // reflectivity/manipulations of rgb light
    float Rg = 0;
    float Rb = 0;
};
```

FIGURE A.11: An example of the PLANE class.

Note that here I have used a bounding box and the plane normal vector to constrain the location plane, this choice was made so that I can easily ensure that rays only intersect with a square plane rather than an infinite plane. The plane may be easily shaded using the RGB triplets that define the whole plane's color, or via a texture. Note that the texture is a single float pointer ($\sim$64bits) rather than a container for an image ($\sim$1Mbyte) so that this plane may simply point to a single texture location which can be reused for many planes to save memory (see Fig. A.13).

Primitive objects are particularly fitted for GPU rendering. Since these objects typically only require a few bytes of memory they are quickly transferred from the host memory to the device memory after discrimination and exclusion.

World and Camera Buffer

The most time consuming part of a ray tracer (∼95%) is testing and sorting ray-object intersections. Because of this it is desirable to minimize the number of objects that are tested. An obvious discrimination is that objects outside the camera's field of view will not need to be tested, this is referred to as the "viewing frustum".

To separate and store objects that will be tested from those that won't be tested, we create two "World"s. The main "World" is typically allocated in the abundant host memory as a void pointer to a void pointer (void**), while the "Camera World" is allocated in device memory. The "World" contains pointers to all the objects that exist, while the "Camera World" only contains pointers to objects that the camera will try to render. Upon each time-step or frame, the host determines which objects in the "World" might be seen by the camera and fills in the pointers of the "Camera World". In this way, many objects from a complex scene can be excluded from hit tests to save time.

Bounding Volume Hierarchy

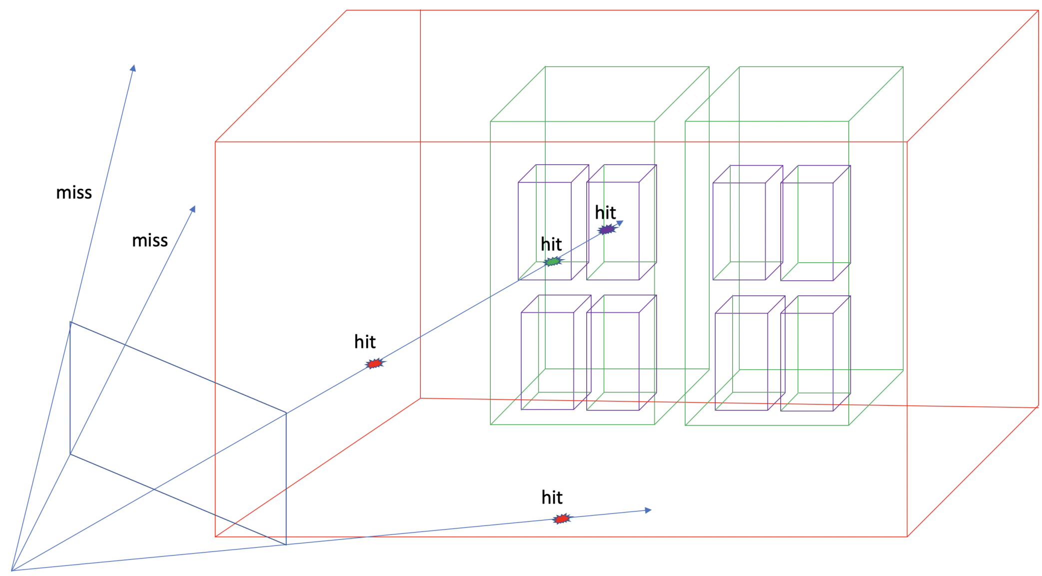

FIGURE A.12: An example of the Bounding Volume Hierarchy. In this environment the left two rays only need to preform one hit test since they miss the outer most volume. The upper right ray performs 7 hit tests, 1 for the red volume, 2 for the green volumes, and 4 for the purple objects inside the left green volume.

Another method of reducing the number of ray-object intersection tests is to use the Bounding Volume Hierarchy (BVH). The BVH is incredibly powerful when the number of objects is large, as the number of objects approaches infinity the BVH reduces the complexity from $\mathcal{O}(n)$ to $\mathcal{O}(\log n)$.

To setup the BVH one simply groups objects by proximity and finds the minimum volume that contains them. Objects within the volume are only tested for intersections if the ray first intersects the volume.

As an example, we can consider an environment with 10x10x10=1000 objects spaced equally along the 3 axis as a 3D grid. Naively one would say each ray has to check for intersections with 1000 objects. By splitting the objects into 2 volumes along each dimension, creating a total of 8 bounding volumes that contain all 1000 objects or 125 each. Each ray now may only need to check 133 objects, the 8 bounding volumes, and the 125 objects within the volume it hits. This simple grouping has resulted in a speedup of almost 8x, however much greater speedups may be achieved with strategic choices of volumes, and volumes within volumes. An example of using the BVH is shown in figure A.13, the primitive planes that makeup the landscape are also dynamically subdivided into 32x32 bounding volumes with 32x32 planes in each.

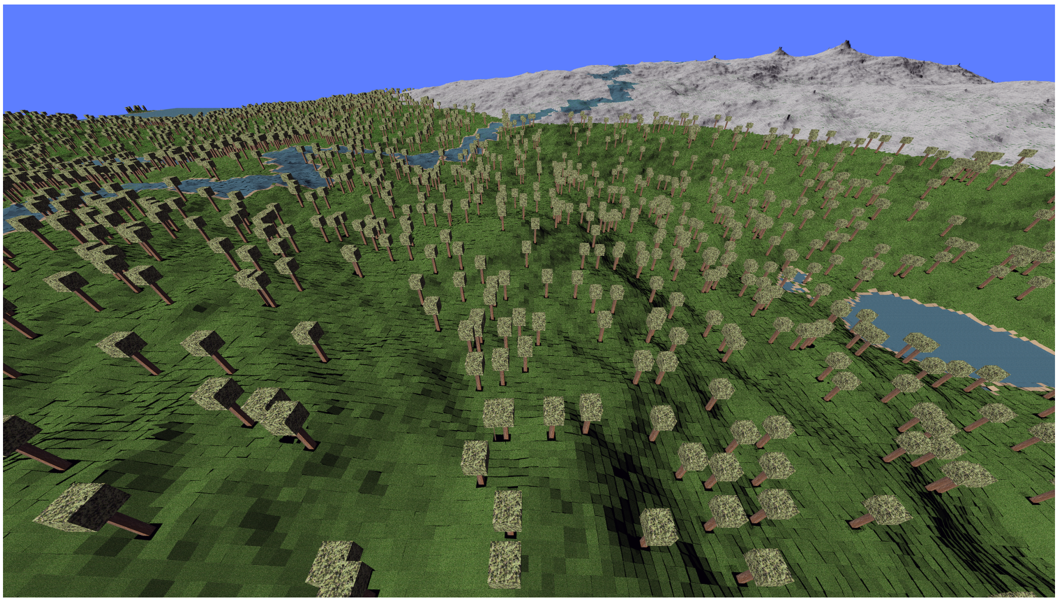

FIGURE A.13: An example of the Bounding Volume Hierarchy. In this environment the primitive planes that make up each of the trees are contained within their own bounding volumes. The primitive planes that makeup the landscape are also dynamically subdivided into 32x32 bounding volumes with 32x32 planes in each. Note that this very large number of objects (>1Million) would take an unreasonable amount of time to render without the use of the BVH, but takes $\sim$1s to render in 4K on a RTX 2080 with the BVH.

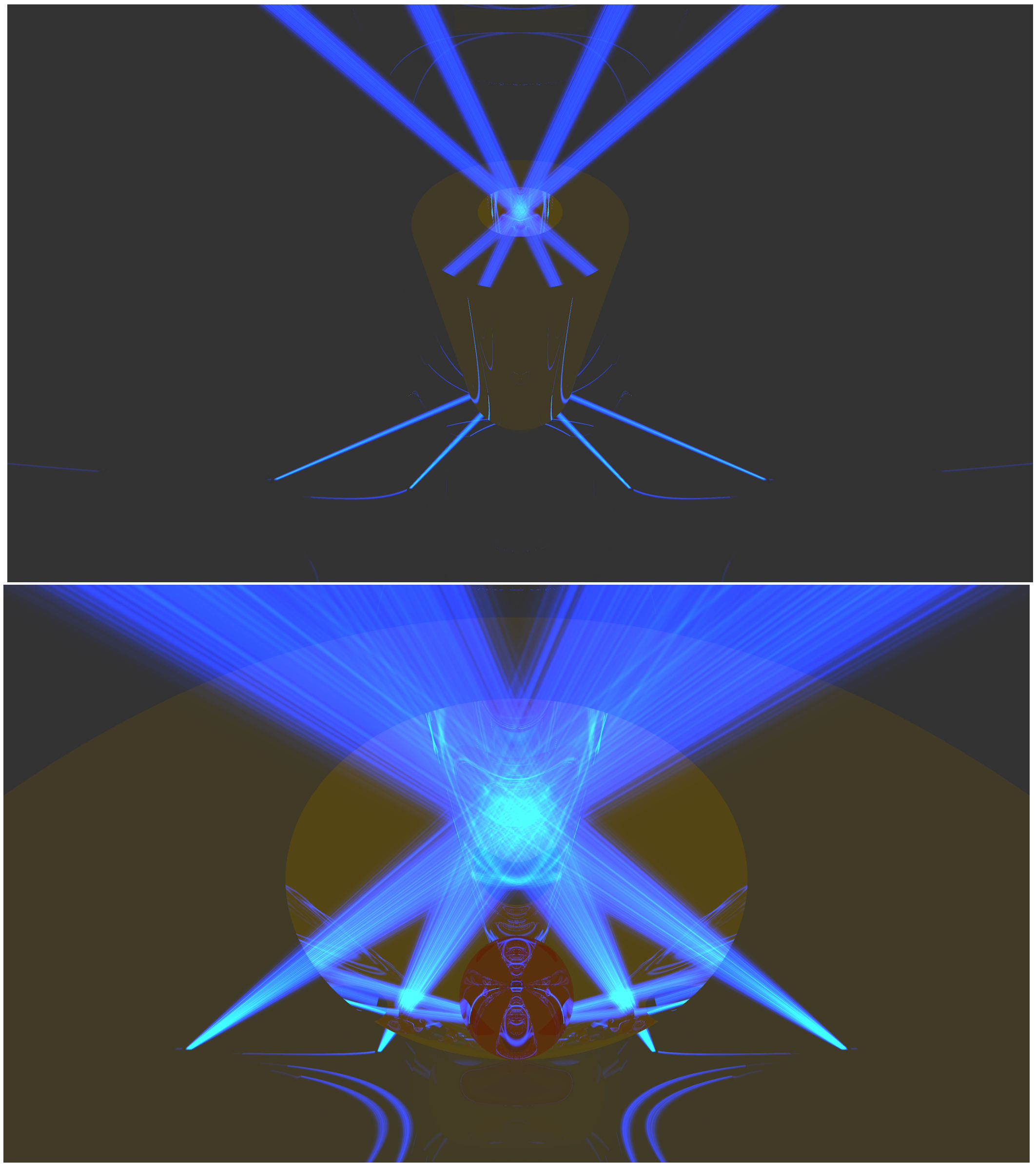

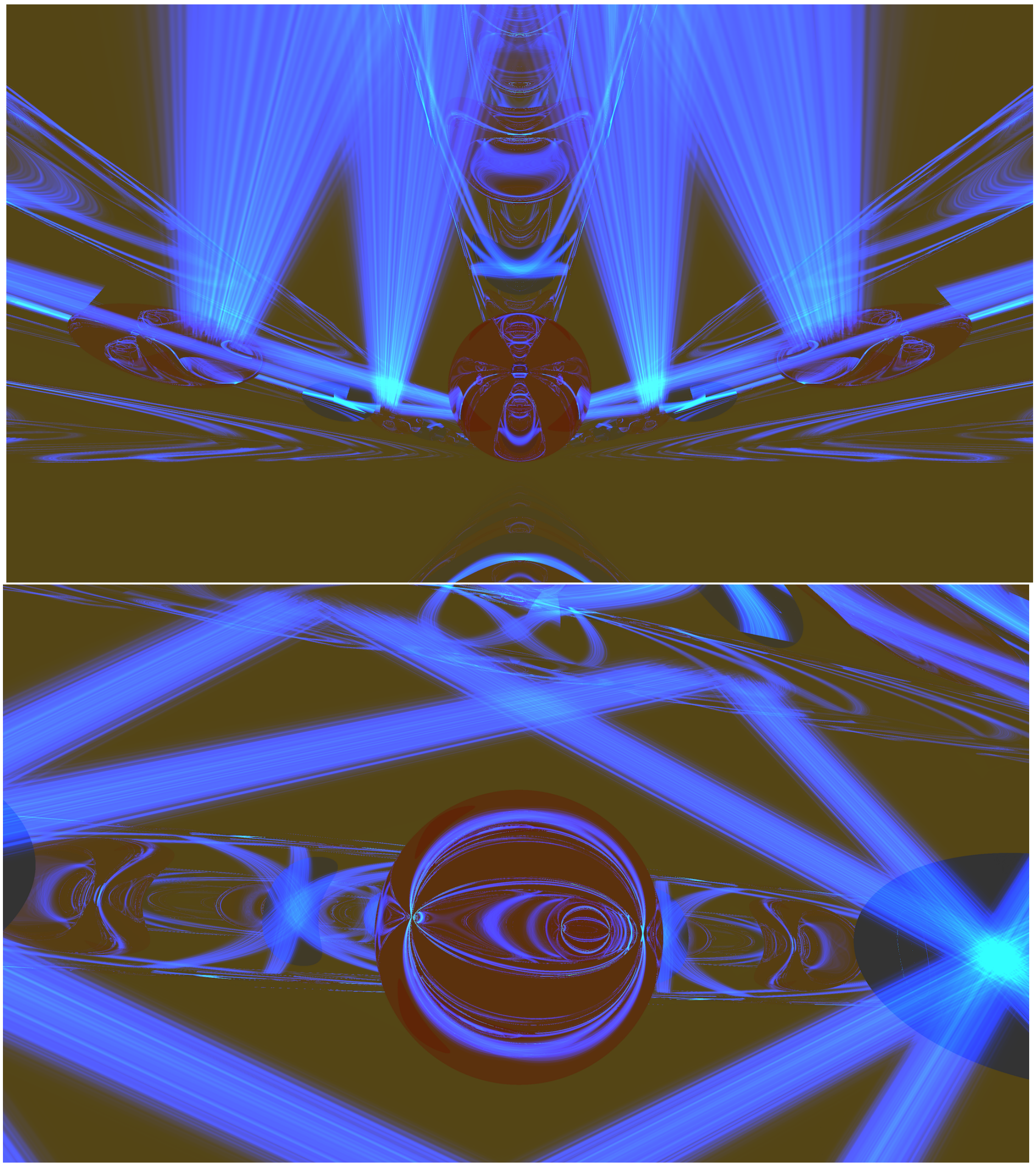

FIGURE A.14: A gold NIF Hohlraum, with a red fuel capsule, in a gray target chamber. Ray traced with 8 full 3D NIF-like paraxial lasers and 10 reflections.